MANUFACTURING, CHARACTERIZATION AND MODELING OF HELICAL ELECTROSPUN FIBERS FOR CARDIAC TISSUE ENGINEERING

AHMED ALATTAR

A THESIS SUBMITTED TO
THE FACULTY OF GRADUATE STUDIES
IN PARTIAL FULFILLMENT OF THE REQUIREMENTS
FOR THE DEGREE OF
MASTER OF APPLIED SCIENCE

GRADUATE PROGRAMME IN MECHANICAL ENGINEERING
YORK UNIVERSITY
TORONTO, ONTARIO

OCTOBER 2021

Abstract

Cardiovascular disease is a predicament that affects the entire world. Complications arise due to inadequate blood supplied to the heart muscle, which leads to scar tissue formation and ventricular dilation. One of the proven methods to promote cellular regeneration is the implantation of seeded scaffolds using stem cell therapy. Electrospinning has been selected to manufacture scaffolds due to the providing a suitable structure to promote cultivation of cells. Each application requires a set of criteria to be met in a seeded scaffold. In cardiac applications, the mechanical properties and matrix structure need to align with the native tissue.

In this thesis, the optimal process parameters to attain electrospun helical fibers are determined. Secondly, the material behaviors of helical scaffolds are examined under different loading schemes. Lastly, numerical modeling for the experimental data is evaluated.

Acknowledgement

I would like to first extend my gratitude to Dr. Aleksander Czekanski for providing me the opportunity to pursue my graduate studies at York University in its Innovative Design and Engineering Analysis Laboratory (IDEA-LAB). He introduced me to the novel bioengineering field. His support and guidance provided throughout the research was tremendous and assisted me to meet my research goals.

My thanks also extend to Natural Sciences and Engineering Research Council of Canada (NSERC) particularly Collaborative Research and Training Experience (CREATE) program for funding this research. I also express my gratitude to the technicians in the mechanical engineering department at York University's Lassonde School of Engineering, as they provided technical support with the apparatuses used in my studies.

One a personal note, my deepest thanks to my parents and fiancée for supporting me through the toughest times. Their unconditional love and support was crucial in the past two years and it was the main reason I could fulfill my ambition. Finally, I am thankful to the IDEA-LAB members and friends for the encouragement and support. A special thanks to Dr. Elli Gkouti for assisting and guiding me through the research.

Table of Contents

Notations

Ψ Strain energy density function

I_i Invariant of Cauchy-green deformation tensor

J Deformation tensor

λ_i Principal stretches

μ_0 Shear modulus

λ_{m} locking stretch

ε Strain

$\dot{\varepsilon}$ Rate of strain

J_{el} Elastic volume ratio

K_0 Bulk modulus

$G\infty$ long term shear modulus

τ_i Relaxation time

List of figures

List of tables

1. Introduction

1.1 Cardiac failure impact

Cardiovascular disease is a predicament, affecting approximately 26 million people globally each year [1]. In North America, variations of heart disease are the leading cause of death [2]. In the United States, one out of every four deaths are caused by heart disease, 655,000 people per year [3]. As of 2016, 85.6 million adults Americans had at least one type of cardiovascular disease. During the same period, it was estimated that more than 6.2 million were living with some form of heart failure. Statistical analysis predicts that this will increase to up to 8 million by 2030 [1].

Heart failure costs healthcare an estimated US$108 billion globally per year, which accounts for 1-2% of global healthcare budgets. The spending is spread unevenly worldwide, with 28% of spending occurring in the United States, 7% in Europe, and the remaining 65% spread among the rest of the world [4]. This high cost is because heart failure is the leading cause of hospitalization in both North America and Europe, accounting for 1 million admissions. Patients with preliminary diagnosis of heart failure account for 1-2% of patient's admissions. Meanwhile early post-discharge mortality and readmission rates have remained constant [5].

Life as a heart failure patient is difficult; patients suffer decreasing quality of life. Some therapies can provide varying degrees of improved quality of life, but many patients still experience recurring hospitalizations [4]. Many studies have examined the effect of exercise on heart failure patients and have concluded that anaerobic exercise has to be tailored to the patients, which in turn complicates the recovery process [6]. Moreover, older patients generally face difficulties in exercise due to reduced mobility [4].

1.2 What is cardiovascular disease and heart failure?

Heart failure is a complex syndrome that does not have a clear diagnostic path. Many symptoms or causes combined can lead to heart failure [7]. Heart failure may be defined as a pathophysiological state at which adequate amount of blood to supply the body is not delivered to the heart [8]. The main cause of blood delivery restriction is due a partial blockage of the artery as seen in figure 1.1. Due to blood delivery restriction to a certain group of cells cardiomyocyte and endothelial cell death occur rapidly. Furthermore, cell death triggers an inflammatory response and subsequently cytokine secretion. The following phase is spread of cell death and a mild natural cardiac regeneration effort is commenced. The last phase, which leads to heart failure, is the scar tissue formation leading to excessive stiffening of cardiac tissue and left ventricular dilation [9]. The phases of heart failure are summarized in figure 1.2.

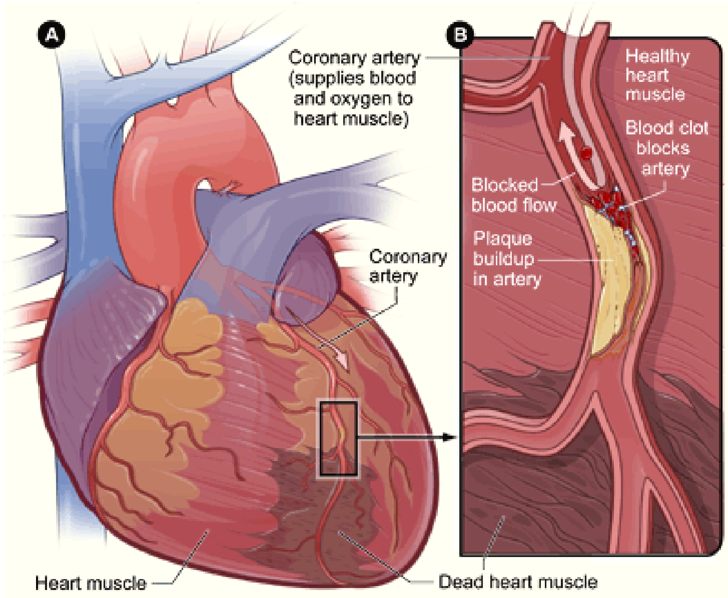

Figure 1.1 (a) Deceased cardiac tissue due to a heart attack, (b) blocked artery restricting blood flow and thus oxygen deliveredit captiony to the tissue [3].

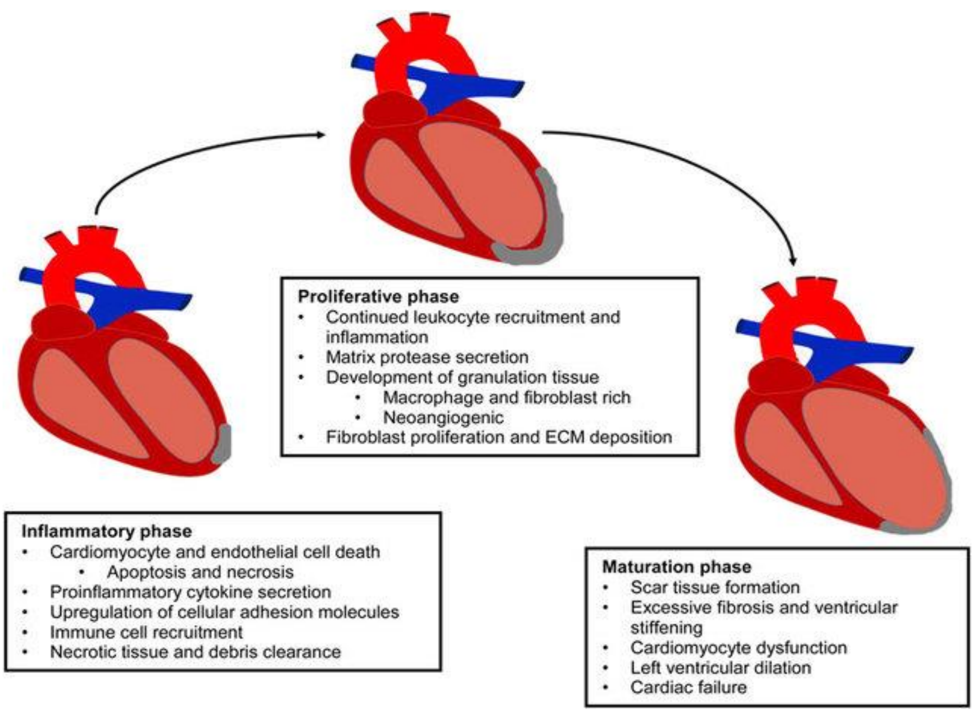

Figure 1.2 Three phases of myocardial infraction;the three phases may be summarized as: inflammatory phases, proliferative phases, and maturation phases [9].

Cardiac muscle is different from other skeletal muscles in the human body. While conventional skeletal muscle undergoes a degree of regeneration, the cardiac muscle regeneration rate is significantly lower [10], [11]. Due to lower cellular regeneration of the cardiac muscle, it was observed that the rate is insufficient to achieve complete recovery [8]. Along with one of the methods mentioned earlier, the scientific community agreed that another approach is necessary. From this, a novel branch of research named Tissue Engineering (TE) was derived. Electrospinning is one of the most popular techniques utilized in TE, and this method has been selected to meet the research objectives here.

1.3 Research objectives

This thesis aims to develop a better understanding of the behavior of electrospun helical fibers for cardiac tissue engineering. The objectives are met through multiple studies, each designed to fulfill one of them. The specific research objectives are:

i. Optimize electrospun helical fiber production.

A parameter sensitivity study is conducted to examine the effect of the varying process parameters. The objective of the study is to optimize the helical fiber production. Fibers are characterized using an optical microscope and an image analysis software to determine the fiber morphologies and diameters.

ii. Characterize the behavior of helical fibred scaffolds.

Scaffolds are prepared based on the optimal parameters obtained from the sensitivity study. Samples were processed for testing using a Rheometer with tensile fixtures. A comparison between electrospun samples and solid polymeric samples are conducted to determine the properties more akin to the native cardiac tissue. Three different loading schemes was used to determine the stress relaxation, recovery and softening. Sample recovery after conditioning was also explored after 24-hour recovery period. Finally, coupons are tested to failure to examine the material response,

iii. Develop a numerical model to predict the scaffold response under different loading conditions.

The hyperelastic behavior of the material attained from mechanical characterization was evaluated against existing theoretical hyperelastic models. Stable models for each case tested is analyzed with respect to the experimental data to determine the accurate models. Furthermore, experimental viscoelastic response is utilized to establish a theoretical model using Pony series functions.

1.4 Thesis outline

Chapter 2 expands on the literature review, including tissue engineer (TE) field, the methods utilized in TE. This chapter also covers the criteria to achieve a successful scaffold. The electrospinning technique has been selected as a suitable method to address the research questions raised, which are highlighted in intensive literature review in the following subsection. Understanding the mechanical properties of the native heart tissue is crucial to a scaffold with similar mechanical properties to the heart; this is also covered in the literature review. The methodology for the studies conducted are outlined in **Chapter 3**. Results of studies conducted focusing on the manufacturing of the helical fibered scaffold are stated and discussed in **Chapter 4**. The chapter is divided into studies, a sensitivity study and a temperature-controlled study. **Chapter 5** highlights the behaviour characterization of the helical electorspun scaffolds. **Chapter 6** discusses the numerical modeling of the scaffolds. The accuracy of the of the model compared with test results are stated in the chapter. Conclusions and future remarks are provided in **Chapter 7**.

.

2. Literature review

2.1 Introduction to tissue engineering

Tissue engineering is a developing field that involves both principles of engineering and life sciences. The main objective of utilizing this discipline is to develop an engineered method to aid with recovery, maintenance and improvement of native tissue [12]. This discipline emerged out of the lack of donor organs and the various complications related to a transplanting procedure [13]. Researchers have explored various methods to achieve the objectives outlined. Cardiac tissue engineering research can be divided clearly into paths. A group of researchers aims to increase the level of cardiac muscle repair through stem cell therapy [14]. Meanwhile, another research path is examining the effects of utilizing various materials to promote cardiac tissue repair [15]. A more prevalent method is to develop a scaffold for cell seeding. Scaffolding cells has been widely successful in promoting regeneration of different types of human tissues via seed cells on scaffold, the most common of them being human bone tissues [16]. The same path has been adapted for cardiac muscle regeneration. A recent study was successful in stimulating and producing cardiac patches made from biomaterials [17].

2.2 What is a scaffold?

A scaffold is an engineered patch that allows the seeding of a stem cell derived cardiomyocytes. The materials of the scaffold can vary widely depending on the production method of the scaffold. Although, most of the materials used in Tissue Engineering have the same basic criteria, they vary from polymers to hydrogels [18]. The basic objective of a scaffold is to mimic the cell environment or extracellular matrix (ECM). With the goal defined clearly, the engineering process needs to consider various aspects and design elements to achieve a functional scaffold, which can be visualized in figure 2.1 [17]. Design elements can be met by using different manufacturing techniques and solutions.

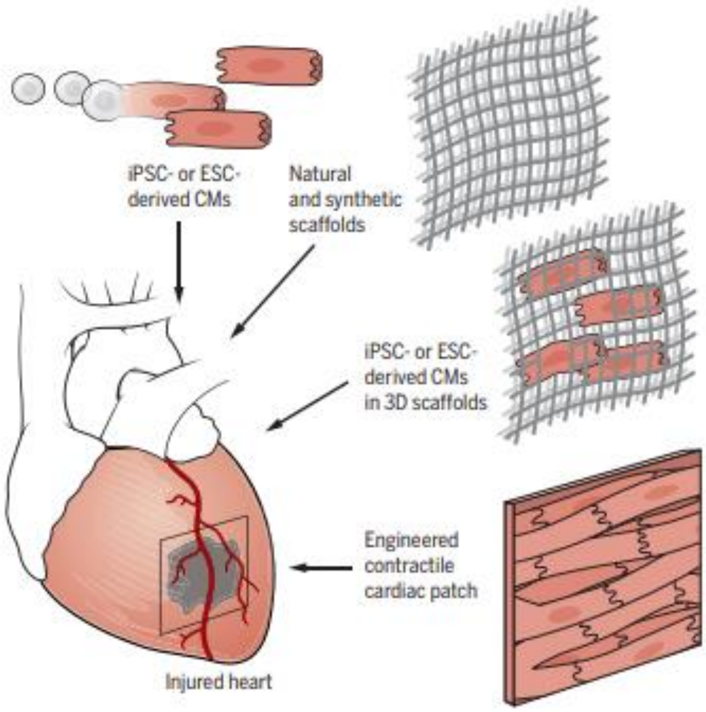

Figure 2.1 Seeding scaffold with stem cells obtained from cardiomyocytes for the scaffold to be utilized in in-vivo implantation [19].

2.3 Successful scaffold criterion

A cardiac scaffold has set off criteria in order to be successful in terms of witnessing sufficient cellular growth for implantation. While achieving cellular growth is crucial, other criteria are also essential for a successful scaffold. The materials utilized in the fabrication technique must be biocompatible, and depending on the application, the material must be biodegradable as well. There are some significant advantages of utilizing tissue engineering for cellular based transplantation approach. One of the major advantages, is providing a 3D environment that mimics the natural Extra Cellular Matrix (ECM) of the cardiac tissue. The environment of the scaffold should provide some key aspects for the cardiac cells, which can be seen in figure 2.2 [20].

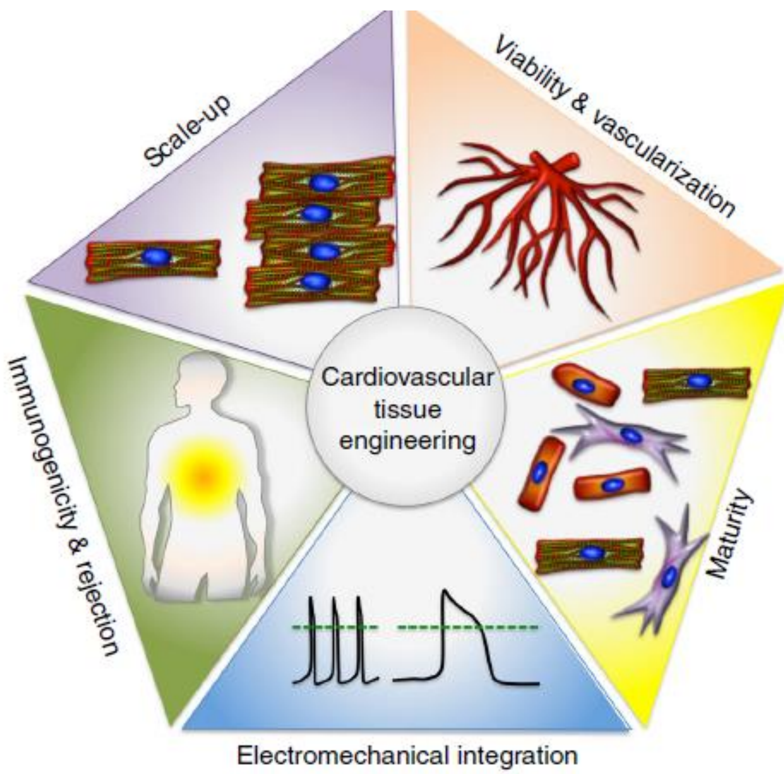

Figure 2.2 Bottlenecks encoutred in cardiac tissue engineering [20].

Achieving an ECM environment in a scaffold is the main challenge facing the scientific community now. A fibrous structure has been identified to be crucial for cell organization, survival, and function of the cardiac cells. Developing a successful scaffold environment should allow the seeded cardiac cells to mature and grow by supplying nutrients to all layers of cells and scaffolds; this is known as vascularization. Achieving a fully vascularized scaffold between the various layers of scaffold is still a challenge. Most of the contribution can be classified under two methods.

The first method utilizes a patterned sample mold to shape the scaffold accordingly [21]. The other methods follow a post processing procedure, in which the scaffold was modified post-production to incorporate channels and vents to allow the flow of nutrients [22]. Another aspect to consider is to manufacture a scaffold with an environment that allows for electromechanical integration or conductivity between the cells. The cells develop electromechanical integration within the scaffold, which in turn leads to integration between the scaffold and the cardiac muscle. It was suggested that aligned structures promote higher levels of cardiomyocytes development and maturity[23].

2.4 Electrospinning in tissue engineering

Electrospinning, with all its numerous modifications and setup variations, has been used in the field of tissue engineering for a long time. While its applications are not limited to solely organ regeneration, it also has been utilized in tissue repair, with scaffolds for skin repair application being the most common application. The versatility of this process is the reason why it can be widely molded to a variety of applications, with minor modifications to the technique and parameters. Moreover, electrospun scaffolding has the advantage of being easily manipulated with several post-processing procedures. Modifications done to the scaffolds may include nanoimprinting lithography and laser ablation. These modifications are done to the scaffold to increase the cell and nutrient infiltration in the scaffold [24].

This technique has several advantages beyond the wide adoption seen in the TE field. One advantage unique to electrospinning is that the fibrous scaffold provides a similar structure to the natural ECM found in most native tissues, ranging from bone to cardiac muscle [24]. A study highlighted the functions of a native ECM to cells and compared them to engineered scaffolds, with the several core functions of ECM being fulfilled by the scaffolds. The functions can be divided into several crucial roles of architecture, biological and mechanical properties [17].

2.5 Electrospinning in cardiac TE applications

The literature has explored various methods to manufacture electropsun cardiac scaffold to achieve a cardiac patch with a higher success rate. Selection of the polymer is the first step when it comes to designing an engineered scaffold. Electrospinning materials may be classified as natural or synthetic materials. The advantage of utilizing natural materials is the environment provided by the scaffold resembles the natural environment for the cells and thus increases the probability of them to cultivate and develop. However, most natural materials are expensive and not readily available. Another disadvantage of natural materials is that they tend to be physically and chemically unstable. Synthetic materials are more stable, cheaper, and readily available. The properties of synthetic materials can be tailored according. Various properties may be manipulated include mechanical properties, toxicity, biocompatibility, and degradability.

A major disadvantage in synthetic materials is the lack of natural essential cues present in natural materials, which hinders their performance regarding cell seeding and tissue organization [25]. A review paper has compiled an intensive summary about both types of materials and stated their respective advantages, disadvantages and common applications [26].

Another aspect for scaffolds to obtain similar structure is fibre diameter alignment with native tissue structure. It was observed via Scanning Electron Microscopy (SEM) that the heart muscle structure can be classified into three distinct fibre types, each with a unique function. The outer fibre is Parietal pericardium (Epimysial fibres), which surrounds the entire heart muscle with the function of preventing excessive stretching. Following that is the Epicardium (Perimysial fibres), the main function of this type of fibre is to connect adjacent muscle bundles and is responsible for the anisotropic contraction of the heart.

Lastly, there is the Endocardium (Endomysial fibres), which are small fibrils that surround the cardiomyocytes. Each type of fibre has a unique diameter size. The average fibre diameters with highest percentage of natural presence are 0.15 µm for Endomysial fibres, 1.5µm for Perimysial fibres and 2.5 µm for Epimysial fibres.

The authors conducted a study examining a scaffold based on each diameter of the native tissue structure and concluded that Epimysial fibres promoted CMs spreading and proliferation, while scaffold based on Endomysial fibres provided mechanical structure in line with the native cardiac tissue. Thus, it was suggested that a hybrid scaffold with fibre diameters between Epimysial and Endomysial fibre sizes is the optimal size to facilitate cell growth and vascularization [27].

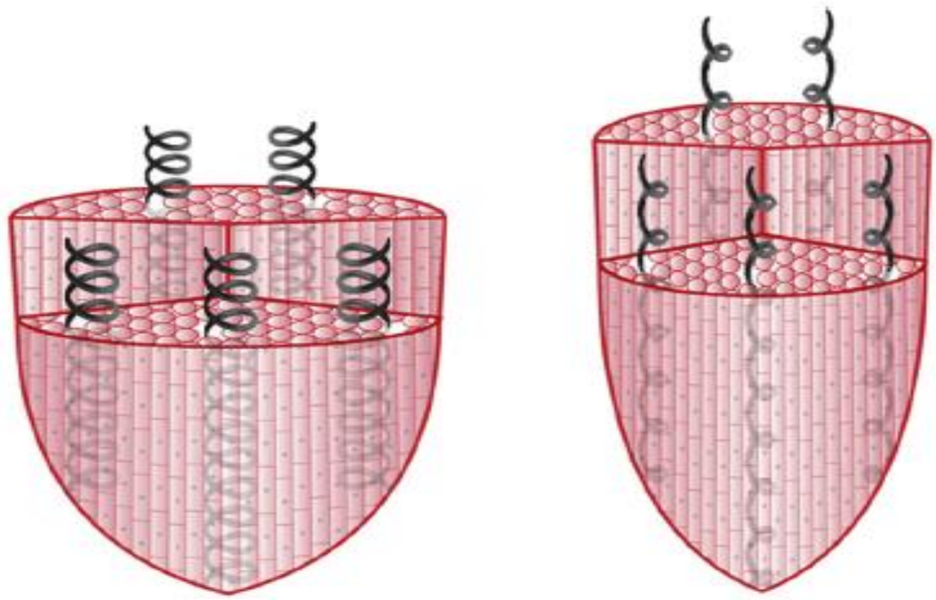

(a) (b)

Figure 2.3 Schematic representing the role of Epicardium during the cardiac muscle (a) diastole and (b) systole [28].

A crucial point that is often overlooked when manufacturing electrospun engineered scaffold is the mechanical properties of the scaffold. Scaffold with similar properties to the native tissue will lead to higher probability of success. The properties of the scaffold can be controlled by manipulating the fiber structures of the scaffold and selecting suitable materials. While a hybrid solution, combining both natural and synthetic material will provide relatively comparable properties and suitable environment for the cells to cultivate [29]. The most common method of altering the fiber structure to achieve better cellular alignment is substituting the flat collector to a rotating drum collector. Utilizing a rotating collector will lead to aligned fibers [30]. A highly aligned fiber structure will result in an aligned cellular structure and thus leading to anisotropic beating of the cultivated cardiomyocytes. However, natural aligned synthetic fibered scaffold result in larger stiffness value range from 50MPa to 4,000MPa when compared to the native tissue with a stiffness range of 200kPa to 500kPa [31]. This leads to a conclusion that random oriented fibers offer a more suitable stress range for cardiac scaffolds.

Native cardiac tissue expands up to 20% of its sedentary size during the systole segment of pumping blood, with a rate up to 200 beats per minutes. Due to the anisotropic nature of the muscle, the force is generated and engineered scaffolds needs to withstand the generated force [25]. A recent study concluded that straight fiber does not provide adequate stretching to meet the natural cardiac tissue criteria and thus explored helical fiber production and adaptability for cardiac TE application, implementation of helical fibers in scaffolds can be seen in figure 2.4 [28]. Furthermore, the literature has explored various modifications to the electrospinning process to manufacture helical fibers for different applications. The modifications focused mainly on alternating the collector to generate a buckling force [32]. Due to the buckling phenomena being unpredictable and the electrospinning process being a random process in nature, obtaining a scaffold of entirely helical fibers is a challenge.

Nevertheless, some parameters may be altered to increase the buckling probability in the process. A study explored the effects of some parameters on the buckling of fibers. The author concluded that two types of buckling patterns may be observed, two dimensional and three dimensional and both patterns are influenced by the distance that the fibers travel before deposition [33]. Another study demonstrated that the effect of increasing the polymer concentration in electrospinning solution led to an increased helical fiber production in a scaffold [28].

Figure 2.4 Illustration of cardiac cells during diastole and systol; (a) utilizing a helical fiber promotes increased stretching, (b) CMs on straight fibers does not have an ability to stretch adequately [28].

2.6 Electrospinning setup and process

The setup of a conventional electrospinning process is elementary yet versatile in obtaining varying results. There are three crucial components to the setup, a high voltage power supply, a needle, and a collector. The high voltage power supply is connected to the needle using a high voltage graded cable to endure the voltage and current supplied. A successful electrospinning process requires a blunt needle, with the desired gauge size. Any conductive material may be selected as the collector. However, the shape and size of the collector will vary the structure of resulting electrospun fibers. While tip to collector distance (TDC) is the distance from the end of the blunt needle, or the spinneret to the collector, it has a major effect on the fiber morphology. The electrospinning setup schematic can be seen in the figure 2.5. The following subsection expands on the electrospinning process parameters.

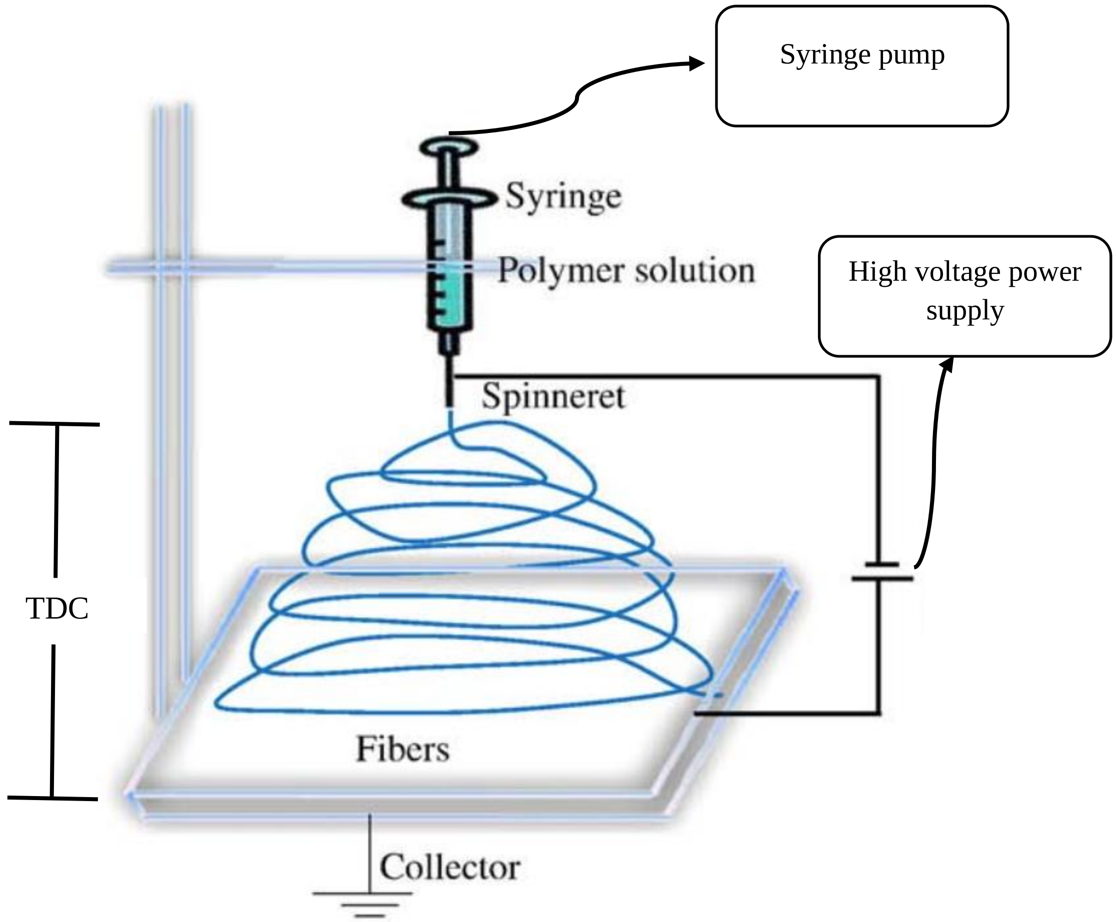

Figure 2.5 Schematic of vertical electrospinnig setup [34] .

Electrospinning theory is rudimentary as the setup. High voltage sourced from a power supply creates forces that act on the solution resulting in the electrospun fibers. DC voltages utilized may vary between 1 to 30Kv depending on the solution and desired fibers structure. The high voltage supply induces evenly distributed charges on the surface of the needle. Thus, charges on the needle result in two forces, electrostatic repulsion force between the surface charges of the solution and an electric force exerted by the external electric fields [35]. The formation of the Taylor cone and forces acting on the droplet can be visualized in figure 2.7 (a) and (b).

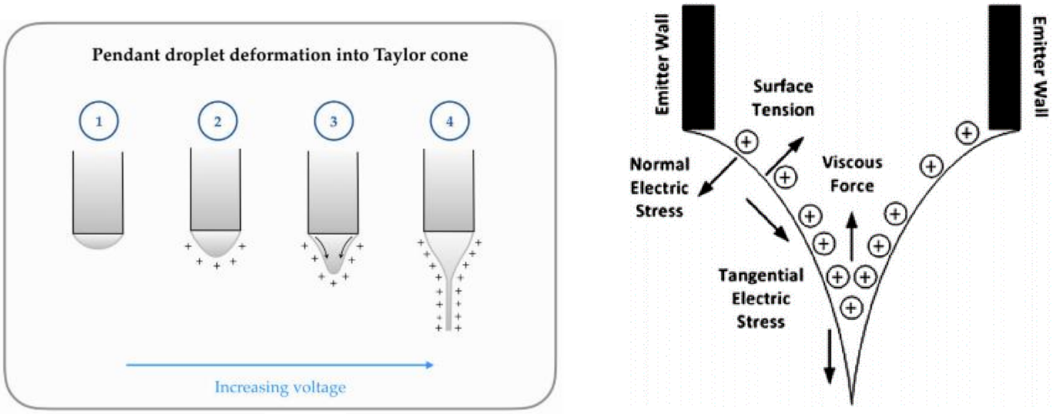

(a) (b)

Figure 2.6 (a) Taylor cone formation due to forces generated on a solution drop at the needle tip, (b) summation of forces required for Taylor's cone formation [36], [37].

As the electric forces increase and reach a certain value that surmounts the surface tension forces of the solution a cone shape is produced, known as the Taylor cone. A Taylor Cone is produced from positively charged solution; a jet is produced from the cone’s peak. The forces from the electric field, generated by the high voltage connect to the needle, increase, the jet continues to stretch further at high velocity. The word spinning in electrospinning is derived from the next stage in the process. As the jet is stretched with high velocity it is forced into a whipping and spinning motion, which result in long thin fibers [38].

Conventional electrospinning process will generate random mat of fibers. However some modifications to the process may be introduced to generate different results [30]. Forces generated on the solution will control the fiber diameter. To vary the fiber diameter, either the solution characteristics or the amount of voltage utilized in the process has to be altered [26].

Classification of the stable jet induced via an Electrospinning process is divided into four sections. The first section is known as the base section, which is identified when the solution jet is emitted from the needle. The next section is the jet section. The key aspect of this section is obtaining a continuous jet, which is subsequently divided into many fibres in the following section. Thirdly, the continuous jet is affected by various forces, causing the jet to be unstable. The instability of the jet will cause it to start a whipping motion, which in turn results in a spinning motion of the continuous fiber. Hence, the name of this section is identified as the instability section and the name of the electrospinning process. Finally, the unstable jet reaches the collector in a section known as the collection section [38] .

The base section of the electrospinning process has two key identification criteria. A jet is drawn from the liquid solution and is emitted from the needle tip. Due to the forces acting on the surface of the solution emitted from the needle tip, a conical shape is formed. The cross-section area of the conical shape may differ according to the properties of the solution used and the size of the spinneret. A jet is discharged from the Taylor cone when the electric force exceeds the surface tension force of the solution due to the electric field [28].

During the jet section the fiber is emitted from the end of the Taylor cone created during the initiation of the base section. The electrical forces maintain a constant discharge of the solution to achieve a continuous jet. The initial decrease of diameter occurs during this stage of the process. A decrease in diameter of a jet is inversely proportional and driven mainly by the flow rate of the solution. Mass per time is also considered as a main factor of determining the diameter of a continuous jet. As the flow rate decreases, the diameter of the jet increases maintaining a constant mass per time during the entire process [40].

Instability forces cause whipping or spinning motion in the continuous fiber, which in turn leads the fiber to be stretched and its shape to altered resulting in nano-diameter sized fibers. In several cases the forces acting on the jet may lead to the jet being split into multiple jets, which is known as splaying [41].

Due to the forces acting on the continuous jet, any excess charges require a substantial duration to be redistributed along the length of the jet. The bottom end of the jet generated extremely high velocity due to the Coulomb forces repelling each other during the stretching and solidification of the jet. A whipping or spinning motion, which drives the fiber into loops, is generated due to the immense velocity of the jets. As the jet moves closer to the collector, the loops generated by the jet grow larger in diameter and stretched the jet even further decreasing the fiber diameter [40].

The final section of the process is the collection region. The key identification of the collection region is the jet being motionless and deposited on the collector. Depending on the solution used for the electrospinning process the solvent evaporates and the polymer fiber is present on the collector [39]. However, if the process utilized an abrasive or a harmful solvent for life cells, the scaffold should be rinsed with water to eliminate any traces of chemicals and ensure cell survivability.

2.7 Electrospinning parameters

The electrospinning process is rudimentary, however there are numerous parameters to be optimized to ensure the satisfactory results are met according to the application at hand. Different parameter will have different effects on the fibers produced. Moreover, further examining and understanding the parameters aid in exploring the process in more depth and will prevent future errors from occurring throughout the procedure.

The process parameters are mainly categorized into three groups: solution parameters, process parameters and ambient parameters. Controlling each parameter with respect to the process leads into the desired fiber morphology and scaffold structure.

2.7.1 Solution parameters:

- *Solution concentration*

Solution concentration directly affects the outcome of fiber diameter. A low polymer concentration in the solution leads to nano-sized particles being sprayed. The electrospinning process fails and an electrospraying process will occur naturally instead [42]. Increase of polymer concentration in the solution leads to an increase of beads and beaded fibers can be witnessed as the outcome of the electrospinning process [43]. A further increase in the polymer concentration will result in fiber formation with suitable diameter to be utilized in some applications. However, increasing the polymer concentration above a certain threshold, causes a ribbon shaped microfiber to form [44]. Beyond that point, very high polymer concentration will result in needle blockage.

- *Molecular weight*

Molecular weight is directly correlated to the viscosity of the solution with a direct proportional relationship. To ensure the production of a continuous stream of fibers to form instead of monomeric fibers or droplets, a suitable range of molecular weight is required. However, molecular weight varies depending on the type of polymer and solvent used. During the jet section the polymer leaves the spinneret tip and is electrically stretched. The only factor that maintains the continuity of the fibers during the stretch is the connectivity of molecular chains of the polymer [45].

- *Viscosity*

Viscosity is linearly proportional to both the molecular weight and the polymer concentration of the solution [46]. A key feature to determine whether the viscosity of the solution needs to be increased is the growth of bead diameter and the expansion of distance between beads on a fiber. An identification of the viscosity increasing as is the main parameter affecting the fiber morphology is the bead shape. The bead shape will change gradually from spherical to spindle shaped as the viscosity increase [43].

- *Surface tension*

Surface tension is the driver of the beads in a fiber and the beaded fiber morphology. This is due mainly to the Columbic force needed to overcome the surface tension of the solution [47]. The main effect of surface tension is to decreased area per unit mass of the fluid. Decreasing the viscosity of the solution it may lead to greater bead formation. On the other hand, as the viscosity increase the polymer molecules tend to disperse over the stretched fiber which reduces the chances of bead formation [26].

2.7.2 Process parameters:

- *Voltage*

A critical voltage is the specified value at which the electric field force is greater than the surface tension force and thus a jet of fibers is emitted. The critical voltage differs from one material to another based on the surface tension force generated on the solution. However, Taylor proposed an equation in which the critical voltage of the electrospinning process can be calculated [27]. The increase of voltage correlates to the decrease of entanglement of fibers, resulting in a uniform distribution of fibers in a random mesh. Increasing of the voltage will results in increased polymer discharge, and thus increasing the fiber diameter. On the other hand, it will also result in higher electrostatic repulsive force which results in narrowing down the fibers. A study stated that both effects neglect each other and thus increasing the voltage will not result in major effects on the fiber diameter [48]. Higher voltage also translates into an upward trend in the number of bead formation.

- *Flowrate*

Solution flowrate, or feed rate, is one of the main contributing factors affecting the fiber diameter during the electrospinning process. Generally, a relatively low flowrate is desirable to allow more time for the solvent to evaporate from the fibers, allowing smooth and uniform fiber to from. An increase in the flowrate will result in greater probability of beaded diameter due to lack of drying time for the fiber before it reaches the collector [44]. Decreasing the flowrate will also result in an increase of the average fiber diameter [49].

- *Tip to collector distance:*

Tip to collector distance (TCD) is the major contributing factor in the fiber diameter. Moving the nozzle closer to the collector will decrease the time allowed for the solvent to evaporate before being deposited on the collector. A larger TCD will ensure thinner diameter fibers, due to the whipping motion stretching the fibers further. Decreasing the TCD will result in fiber deformation, due insufficient distance for the fibers to stretch [50]. On the other hand, one result observed no change in the fiber morphology with different distances. However, this is theoretically due to the material used stretched and solidified at a higher rate when compared to other conventional material.

- *Ambient parameters:*

Ambient parameter may also affect the fiber morphology. Humidity and temperature will affect the fiber morphology and may result in deformed fibers. Temperature and viscosity have an inverse relationship on the fiber morphology. An increase in the temperature results in a decrease in fiber diameter, however, an increased deposition rate on the collector has been observed [51]. A very low humid environment leads to the solvent to evaporate on higher rate than accounted for, which might result in a clogged needle tip. On the other hand, an increased humidity aids with the discharge of the fiber jet, resulting in thicker electrospun mats [26].

2.8 Native tissue mechanical characterization techniques

2.8.1 Native tissue mechanical properties

Fully characterizing native cardiac tissue poes various challenges to the scientific community tissue delicate structure and post-mortem effect. Non-invasive methods have been commonly used since the early 20th century, which utilizes the Doppler method in a process known as echocardiography (ECG). This is used to obtain the strain and strain rate of the heart to assess the systolic and diastolic functions. The technology has provided accurate and reproducible test readings [52]. This technique is ideal to detect ischemia of variations in the systolic strain rate and strain not for attaining other mechanical properties. The limitation of ECG for strain rate detection is that it is in a single direction. The strain rate in transvers direction cannot be captured using ultrasound, thus the shear strain rates may not be attained [53].

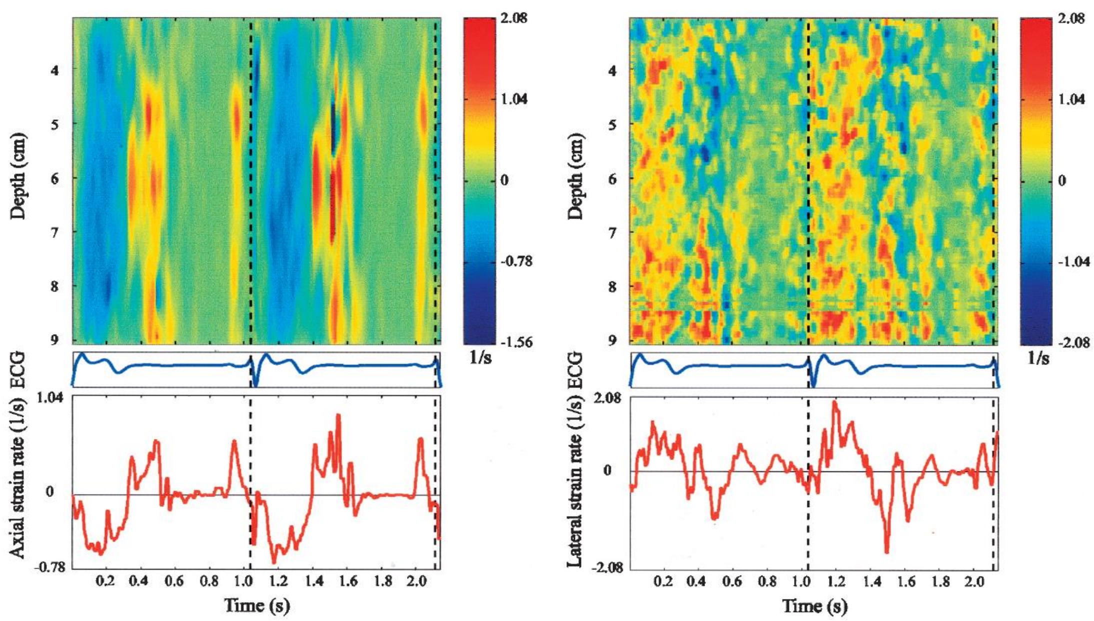

(a) (b)

Figure 2.7 Two-dimensional strain rate of a 29-year-old using an ultrasonic scanner. M-mode image and axial profile of (a) axial and (b) lateral strain rate [54].

To overcome the limitations imposed by the ultrasonic technology, the only viable solution is to utilize invasive method to identify the properties and the behaviours of the native cardiac tissue. The main challenge faced in this technique is the post-mortem effect (rigor mortis) which results in changes that are experienced throughout all the muscular system. This effect commences in the range of two to four hours after death and is considered fully developed after 12 hours. Within this time frame, the tissue endures chemical changes due to the lack of vital nutrients and thus alter the mechanical properties [55]. However, testing the native tissue before the rigor mortis effect is a viable method to attain all the mechanical properties of the tissue. A study was conducted with 5 different hearts from varying age groups and death causes. Biaxial extension protocol was conducted with two different sample types, cross fiber direction (CFD) and mean fiber direction (MFD). Samples were subjected to 1.05 to 1.15 stretch levels, in increments of 0.025 at different loading ratios. It was concluded that the native tissue experiences viscoelastic behavior and that the stress and strain increases with the increase of cross head velocity. Stress relaxation was also observed in the samples within 5 minutes and up to 30 minutes of applying a constant load [56].

2.8.2 Scaffold characterization mechanical properties

On of the criterion of a successful scaffold is achieving similar properties as the native tissue, with mechanical property of the engineered scaffold being one of the overlooked properties. Engineering a scaffold matching the properties of the cardiac tissue, a property range must be outlined and based on the native tissue properties. While native cardiac tissue may expand by up to 20% of its sedentary size during the systole period when the heart contracts, with a rate of up to 200 beats/min, most straight-fiber scaffolds will not experience the same strain [25]. Moreover, natural aligned synthetic-fiber scaffolds have larger stiffness values, ranging from 50MPa to 4000MPa, when compared with those of the native tissue, which has stiffness values of 200Kpa to 500kPa [31]. Through the beating cycle of the heart, the tissue experiences tension while drawing blood into the tissue (systole) and compression while pumping blood out (diastole). Native cardiac tissue undergoes a complex loading scheme, which can be observed using an in vivo ultrasonic technique in order to gauge the strain rate [54]. Loading occurs at high speed and frequency thus causing a bottleneck in testing properties of scaffolds. The final observation that the native tissue is assumed to have an elastic behaviour, that is noted due to the strain rate approaches zero during the unloading segment of the testing [56].

2.9 Numerical modeling of native tissue

Analytical models are utilized to simulate and predict material properties under complex loading condition that poses a challenge to physically examine in a controlled manner. Various modeling methods have been used in literature to accurately predict mechanical properties and behaviors. Attaining the mechanical properties of the spring-like fibered electrospun scaffold will facilitate the development of an analytical model. A previous effort successfully derived a model for a straight-fibered electrospun scaffold manufactured using poly (3-caprolactone) (PCL). The study investigated two different models, Fung’s model of quasilinear viscoelasticity (QLV) and Arruda and Boyce’s eight-chain model to ensure accuracy [57]. While, QLV has been applied to multiple soft tissue and biological materials, including native heart tissue, synthetic polymers tend to have a nonlinear and viscoelastic (rate-dependant) behavior [42]. On the other hand, the eight-chain model is developed based on statistical mechanics and conventionally used in rubber-based applications. Nonetheless, it was applied to simulate human skin [58]. The authors concluded that straight-fiber PCL scaffolds experience viscoelastic behavior, and the loading response of the material is affected by the preconditioning of the sample, which is represented by the stress softening effect. Furthermore, stress relaxation is decreased owing to the preconditioning of the sample, which aligns more with the QLV theory model over the multiple loading situations [57].

2.10 Stress relaxation and stress softening of soft materials

Soft materials generally refer to wide array of materials that include elastomers, biomaterials, and native human tissue and all of them experience viscoelastic behavior along with Mullins effect to an extent. Stress relaxation occur when the material is subjected to cyclic loading, the peak stress point that may be reached decreases with every cycle until it reaches a stable point. This phenomenon can be attributed to the interactions between the matrix and the molecules where more force, speed or repeating of cycles are required to break the molecular chains [59].

The Mullins effect occurs when a material is initially stretched to a certain point and for any subsequent cycle it would require less stress to reach the maximum stretch point [60]. Stress softening or the Mullins effect can be attributed to the damage continuum mechanics [58]. In the literature the material is considered hyperplastic and the strain energy density function is converted to include the damage parameter [59]. Preconditioning the sample via several cyclic loading iterations before the experiment will remove the stress softening effect and result in the true material properties. Most soft materials include native human tissue experience rate dependent viscous behavior and thus the modeling of such material is complex. A study developed a model which couples viscoelastic and Mullins-effect model to characterize soft materials. The model is presented in series which is based on damageable spring characterizing the Mullins effect and Kelvin unit model to capture the viscoelastic portion of the material behavior [60].

2.11 Electrospun scaffolds mechanical characterization

Attaining the mechanical properties of scaffolds are the first step of understanding the material behaviours. Conventional material testing does not provide an accurate comparison to the native cardiac tissue loading due to the complexity of the loading scheme. Utilizing analytical modeling will aid in simulating the complex loading and thus providing the expected material properties. To develop an accurate numerical model of a scaffold certain properties has to be investigated and used as building blocks of the model [57].

Characterizing electrospun scaffolds in depth is scarce topic in the literature. This can be attributed to the delicacy of the material and the need for particular apparatuses. A study conducted has explored the stress relaxation and stress softening behaviours of random oriented electrospun Polycaprolactone (PCL) scaffolds. Furthermore, the author explored two existing analytical models and determined that Fung's QLV theory captures the behaviours during loading and relaxation phases. It was concluded the scaffold experience rate dependant response akin to the native cardiac tissue. Additionally, both stress relaxation and stress softening are evident during testing of the material [57].

3. Methodology

Summary: *Electrospinning parameters has been adopted from the literature to manufacture helical fibers using electrospinning. First discussed is the manufacturing portion of the research, where the helical fiber electrospun scaffolds are manufactured and analyzed. Two different studies are conducted, an optical microscope is utilized for characterization for both scaffolds. Subsequently, a mechanical characterization study is performed to determine the material behavior. Finally, the test results from the mechanical testing is implemented in curve fitting based on present numerical models.*

3.1 Parameter sensitivity study

The materials selected had a strict criterion of being biocompatible and bioabsorbable. Based on this criterion the polymer selected was Poly(3-caprolactone) (PCL) with an average molecular weight of 80,00 (Sigma-Aldrich) and the solute. Dichloromethane (DCM) and Dimethylformamide (DMF) as the solvents were prepared. The ratio was set to constant 1:1, DCM:DMF with varying PCL concentration of 15%, 17% and 19%. For optimal homogenous mixture, the solution was mixed for 12 hours on a magnetic stirrer, while being air sealed to prevent the evaporation of the volatile chemical, DCM. The solution was deposited in a 5ml syringe with a 20-gauge needle, connected using a Luer lock mechanism and emitted using a syringe pump (New Era- 300) at three different flowrates, 0.5ml/hr, 0.75ml/hr and 1ml/hr. The positive terminal was attached to the needle while the negative terminal was connected to the aluminum sheet that serves as the collector. The electrospinnig setup used in our studies can be seen in figure 3.1 and figure 3.2. A constant 17.5kV was held throughout all the experiments. The tip to collector distance (TCD) was varied between 10cm, 15cm and 20cm. A collector angles 0°, 10° and 20° were examined.

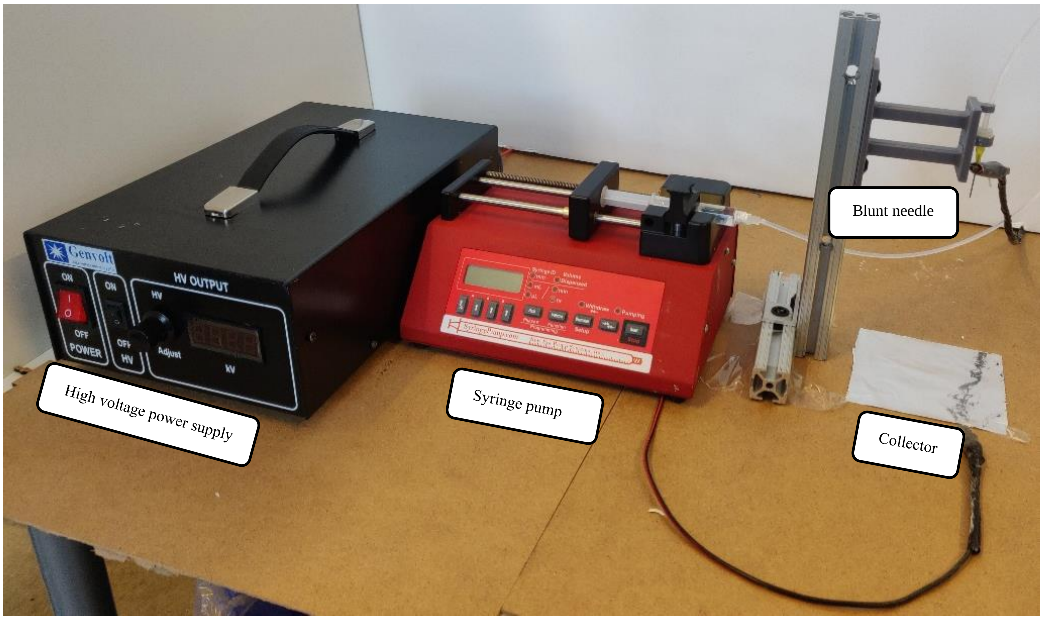

Figure 3.1 Conventional vertical electrospinning set up with an aluminum foil as collector.

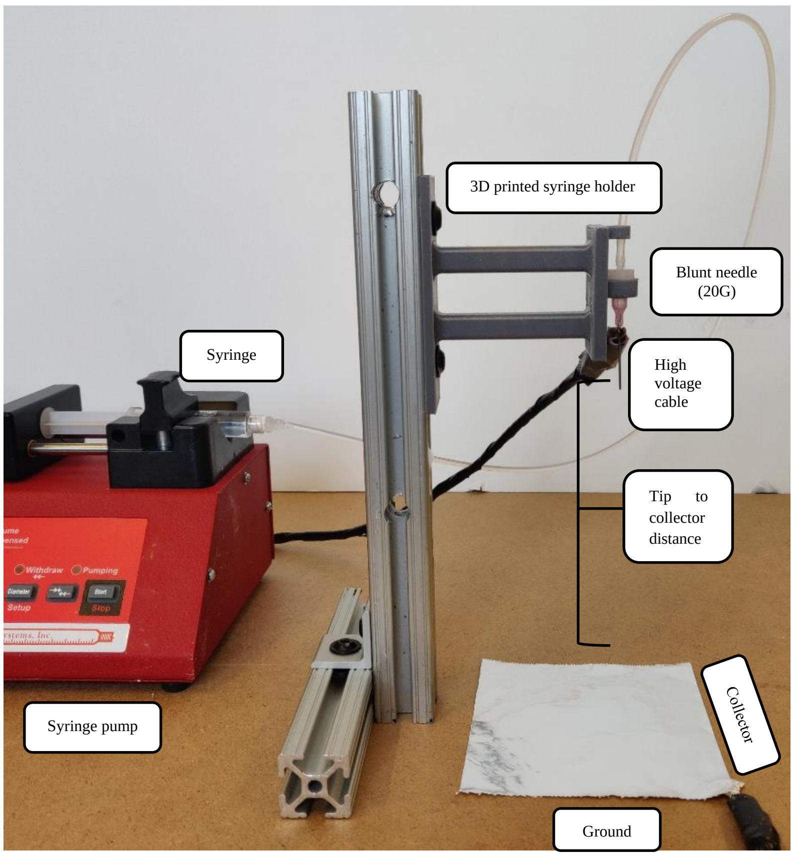

Figure 3.2 Vertical electrospining setup showing the syringe holder, blunt needle, and collector.

3.2 Temperature controlled study

A temperature-controlled sensitivity study was conducted to examine the effect of the temperature on the fiber structure and percentage of fiber structure produced. Temperature of 10°C, 20°C and 30°C was examine in a controlled temperature environment. The temperature control device (Temptronic, Thermostream) utilized was feeding into an open circulation insulated chamber. A constant TDC of 15cm was set for all experiments. All experiments were conducted using 20-gauge stainless steel needle and DC voltage supply of 17kV. Refer to table 3.1 for all varying experiment parameters. The process parameters were determined from our parameter sensitivity study conducted, that is mentioned in subsection 3.1. Similarly, the same methodology was applied to examine the scaffolds. In this study, the aim was to investigate the effect of temperature on the scaffold structure.

Table 3.1 Experiment paramters for temperature-controlled study.

<table>
<tr><th colspan="2">Experiment parameters</th></tr>
<tr><th>Temperature (°C)</th><th>Flowrate (ml/hr)</th></tr>
<tr><td rowspan="4">10</td><td>1</td></tr>
<tr><td>0.75</td></tr>
<tr><td>0.5</td></tr>
<tr><td>0.1</td></tr>
<tr><td rowspan="4">20</td><td>1</td></tr>
<tr><td>0.75</td></tr>
<tr><td>0.5</td></tr>
<tr><td>0.1</td></tr>
<tr><td rowspan="4">30</td><td>1</td></tr>
<tr><td>0.75</td></tr>
<tr><td>0.5</td></tr>
<tr><td>0.1</td></tr>
</table>

3.3 Fiber characterization

Scaffold characterization and specifically fiber characterization has been performed using an optical microscope (Zeiss, Axio Imager M2) to study the fiber structure. Furthermore, the fiber dimension has been obtained using an Image-Processing software (ScopeImage 9.0). An average number of fibers characterized for every scaffold is 50 fibers. The fiber structure was divided into three categories: (i) helix fibers, where the fibers have experienced complete buckling, (ii) partially buckled fibers, where fibers have experienced some degree of buckling, and (iii) straight fibers, where the fibers are straight with no evidence of buckling, which can be seen in figures 3.3. 3.4 and 3.5, respectively. Objectives of this study was to determine the optimal parameters for electrospun helical fibers, thus further studies can be facilitated.

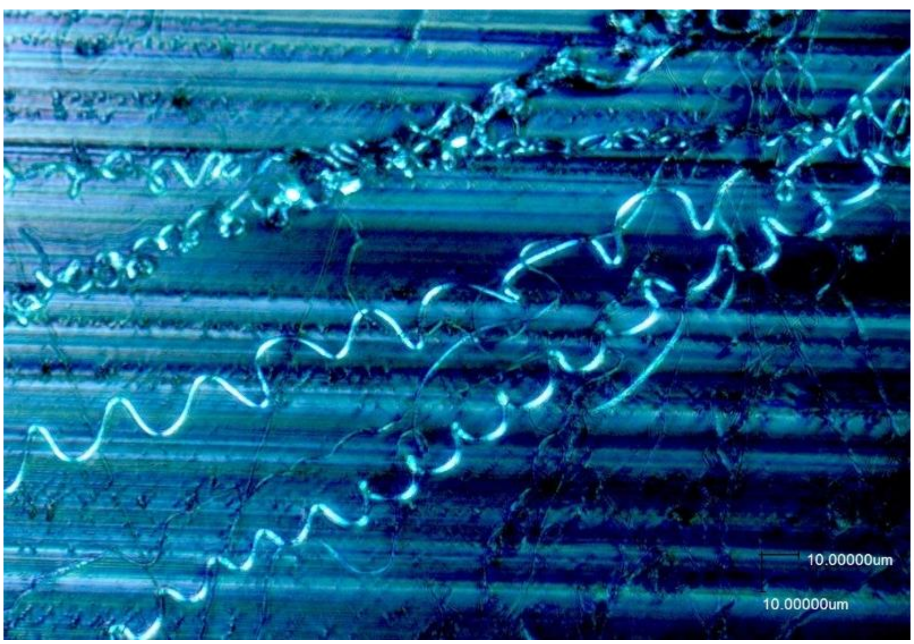

Figure 3.3 Helix fiber obtained from the following parameters: PCL concentration:15%, TCD:15cm, Flowrate:1ml/hr and collector angle 0°.

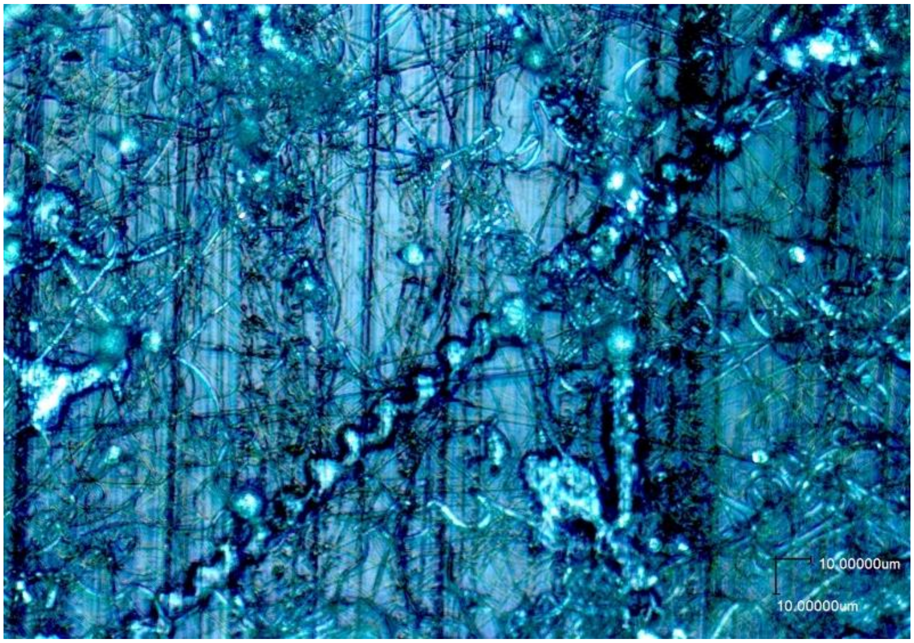

Figure 3.4 Helix fiber obtained from the following parameters: PCL concentration:15%, TCD:15cm, Flowrate:0.75ml/hr and collector angle 0°.

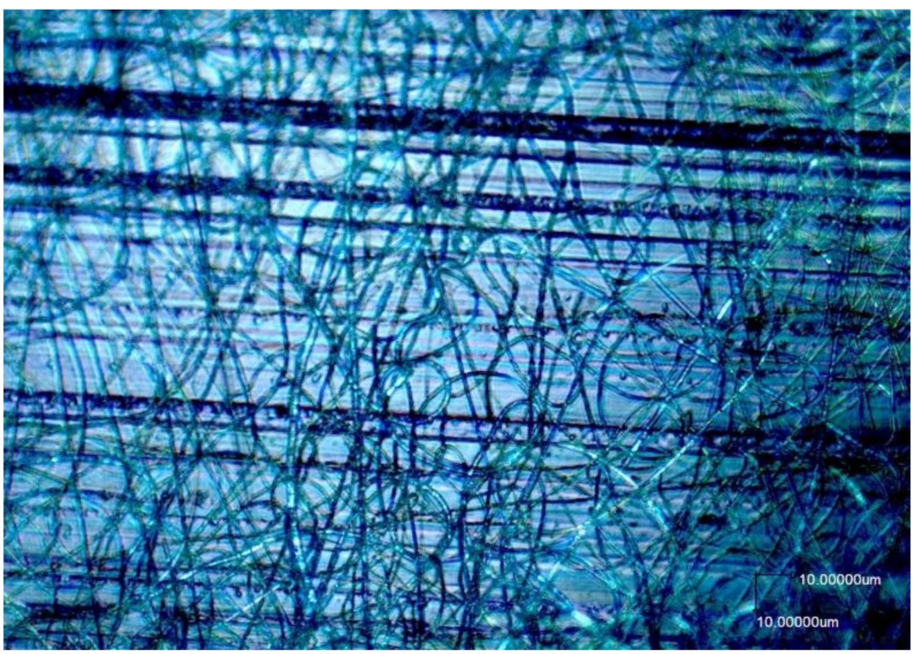

Figure 3.5 Straight fibers obtained from the following parameters: PCL concentration:19%, TCD:15cm, Flowrate: 0.5ml/hr, and collector angle: 0°.

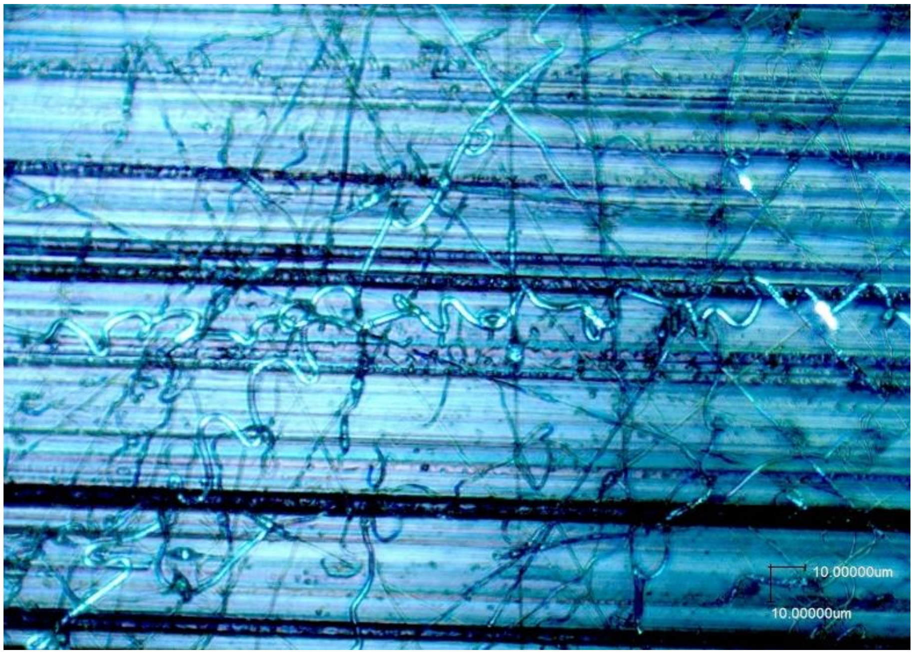

Figure 3.6 Partially buckled fibers obtained from the following parameters: PCL concentration:15%, TCD:15cm, Flowrate:1ml/hr, and collector angle: 0°.

3.4 Mechanical characterization

After the scaffolds were left to dry, tensile sample preparation was commenced. Samples were cut using a surgical scalpel. Additionally, the sample dimensions were governed using a 3D printed mold. The size of the tensile coupons was 27.9mm × 10.48mm. The thickness of the samples varied among the tensile coupons because of the randomness of the electrospinning process and the randomized results. Solid samples were obtained by drying out the polymer solution on a flat area, with the same properties as those used in the electrospinning process, resulting in sheets of polymer with altered characteristics due to the chemical reactions. Solid coupons were tested to identify any differences in mechanical properties achieved through electrospinning. The differences were determined using a processing method akin to the method used for the electrospun samples. Thickness was measured using an optical microscope along the entire sample and was attained using image analysis software (ImageJ). The measured thickness of the latter samples ranged from 0.045mm to 0.11mm, while solid sample thickness ranged from 0.32mm to 0.38mm. The variability in scaffold thickness was due to the randomness of fiber deposition and spread on the collector. An average thickness value was determined for every scaffold, while the electrospun sample thickness could increase by increasing the electrospinning duration, which can lead to detrimental effects. Increasing the duration significantly decreases the porosity of the sample, hindering the cell infiltration and seeding process.

Tensile testing was performed using a rheometer apparatus (TA Discovery model HR-30) with tensile testing fixtures and load cell of 50N, seen in figure 3.7. The data were then analyzed using script running on a commercial software (MATLAB 2020, MathWorks), and average thickness was taken into consideration. We observed that the native cardiac tissue does not undergo conventional compression during diastole. The tissue experiences complex loading conditions during tension and contraction. Uniaxial testing results facilitate the development of an FEM with a high degree of accuracy of the material subjected to complex loading [21]. For uniaxial tensile testing, a configuration of two tests with loading speeds of 0.01mm/s and 0.1mm/s were tested. Loading speed is the speed at which the cross-head is moving and subsequently applying strain on a sample and thus causing deformation. Higher speeds provided unreliable results owing to instrument limitations.

Figure 3.7 TA instruments Discovery Hybrid Rheometer (HR30) with tensile fixture installed.

The first test was performed to outline the resulting stress softening effect due to the applied strain. Samples were subjected to 20 consecutive cycles with a peak of 10% maximum strain and a valley of 2.5% strain. Subsequently, a post-cyclic loading of 300 s of constant strain was applied to the coupon. The reason for unloading until a negligible percentage of strain (2.5%) was reached was to avoid any folding of the tested sample [22]. Additional testing was conducted to confirm stress softening and stress relaxation behavior at higher strain rates.

The following loading conditions were used to highlight stress relaxation and stress recovery in the chosen test material. Multi-step loading was conducted in 5% increments until a final strain of 20% was reached; testing was then repeated in descending order, from 20% to 5%, in a similar manner. A constant strain was applied for 500s post-strain for both increasing and decreasing increments. The time during which a sample was subjected to constant strain was increased from the previously outlined test, from 300s to 500s to highlight the stress relaxation between each loading step. During this experiment, the stress response to constant strain was recorded. This stress response can be either increased or decreased depending on the unloading or loading stage, respectively, namely when the strain is held constant after loading relaxation occurs and stress decreases until an approximate constant value is reached. However, when constant strain follows an unloading step, the tested sample attempts to recover by gradually increasing its stress. Figure 3.8 represents the stress and strain experienced in electrospun scaffolds, representing a preconditioning loading scenario in conventional soft materials [59].

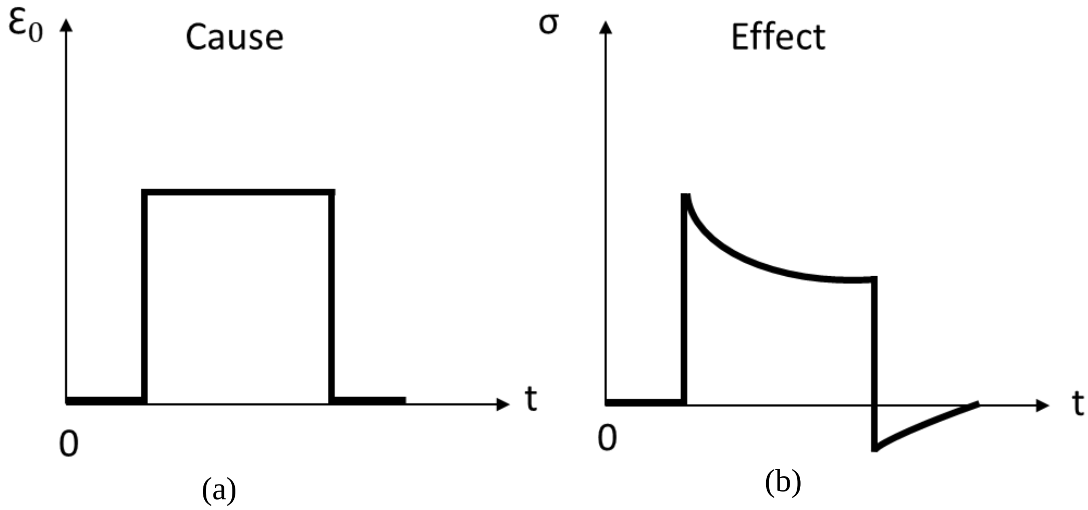

Figure 3.8 Loading cause and effect diagram, x axis represents time (s) (a) constant strain applied over time, where strain, represented by y-axis is the loading applied on the sample; (b) stress relaxation occurs due to the constant strain applied on the sample, where stress, represented by y-axis, being the effect of the applied strain.

Furthermore, a test combining both test procedures was conducted. The objective of this testing approach was to eliminate the stress softening in a material in order to highlight the unbiased stress relaxation and stress recovery phenomena in electrospun samples. Test coupons were subjected to a maximum strain of 20%. During the test, samples were subjected to 20 cycles of loading of 20% to 2.5%, followed by a multi-step testing process. Buckling of the sample would occur at higher strains, higher that 10% of original length, neglecting the need for low residual strain during testing.

3.5 Numerical modeling

Based on the results from mechanical characterization of the scaffold, it was determined that further tensile testing was required to attain data for modeling. Test data for preconditioned and postconditioned samples. Both samples experienced the same loading scheme of 20% strain and subsequently 2000s of constant strain at speeds of 0.01mm/s and 0.1mm/s. Results attained were analyzed to obtain the hyperelastic and viscoelastic models. A curving fitting method was utilized using a commercial software (ABAQUS 2020, Dassault Systèmes). Based on the literature, there is clear consensus if electrospun scaffolds are isotropic or anisotropic [57], [61]. In this study it was assumed as isotropic, however further examination is required. Multiple numerical models were explored to determine the stable models for the hyperelastic segment, where the test results were implemented as uniaxial data. During the characterization portion, it was observed that the material experiences an extended duration of viscoelastic behavior at 20% strain, thus the duration was extended to 2000s. The viscoelastic properties were modeled using Prony series. Based on the modeling results, it was noted that the properties of the material change drastically after conditioning of 20 cycles at the desired strain. During conditioning of the sample some degree of plastic deformation occurs and thus affects the specimen's length in the subsequent loading. Another observation was that the degree of the viscoelastic behavior was affected by the conditioning of the sample. **Chapter 6** expands on the results attained and highlights the conclusions.

4. Manufacturing of scaffolds

Summary: *Two different parameter studies are conducted to examine the manufacturing of helical electrospun fibers. The studies aimed to examine the percentage of helical fiber production and the fiber morphology in every test conducted. The first study conducted was a sensitivity study where the process parameters were varied to observe the effect on the helical fiber production and fiber morphology. Based on the parameters obtain from the first study, a later temperature- controlled study was conducted. Fiber production percentages and fiber morphology were analyzed to determine the effect of temperature.*

4.1 Parameter sensitivity study

4.1.1 15% PCL Concentration Solution

Utilizing 15% PCL concentration solution, the highest percentage of helix fibers produced in a scaffold were observed at 59.7% occurrence and was achieved using the following parameters: flowrate 1 ml/hr., TCD of 15cm and a flat collector. The average helical fiber diameter is higher than both the partially buckled and straight fibers. The average diameters of the fibers are 3.24µm, 1.97µm and 1.32µm for helical fiber, partially buckled and straight fibers, respectively. Furthermore, partially buckled fiber would also be considered as a positive catalyst due to a minor contribution of stretch in a scaffold. Fiber production percentages for the 15% PCL concentration solution are presented in figure 4.1, and average fiber diameters are presented in figure 4.2.

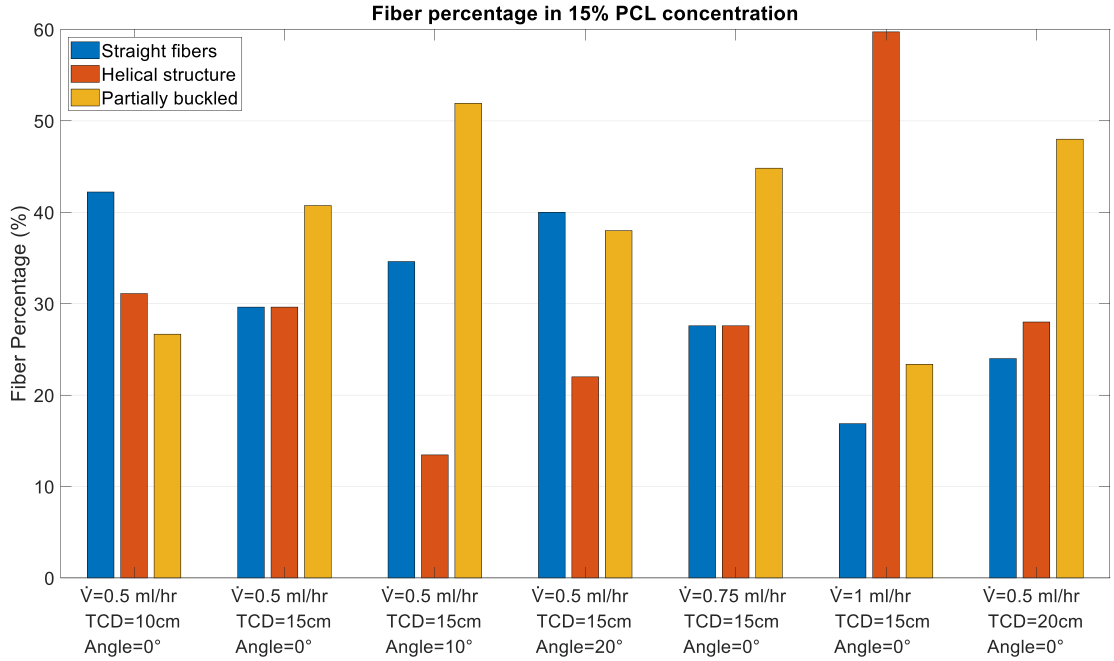

Figure 4.1 Percentage of fiber production obtained with 15% PCL concentration solution with the varying electrospinning parameters.

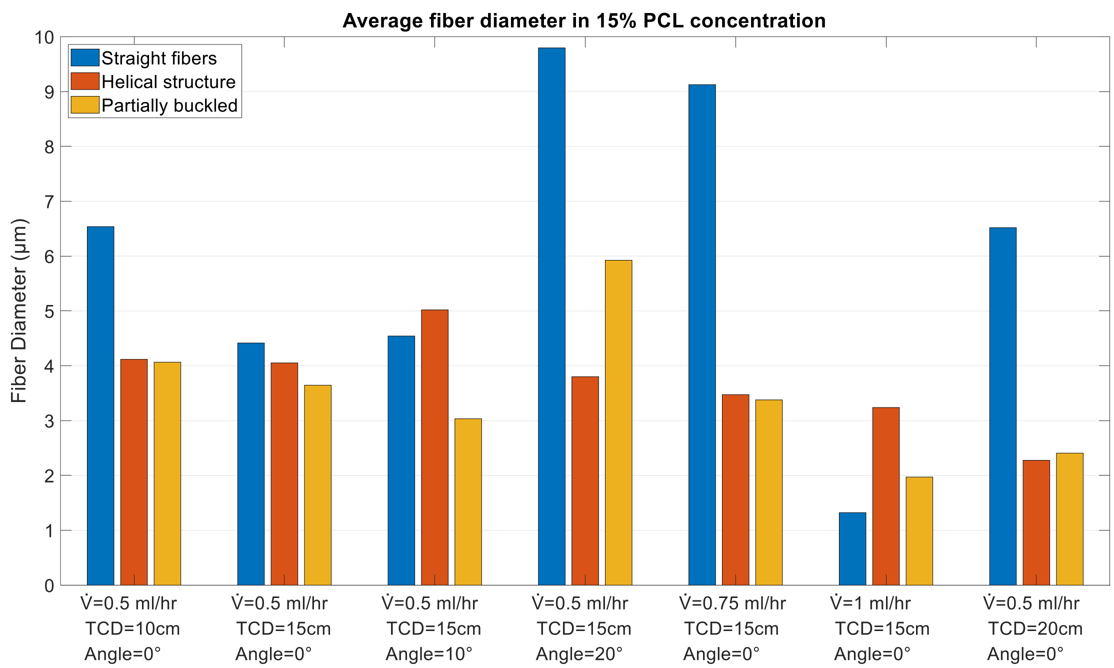

Figure 4.2 Average fiber diameter obtained using 15% PCL concentration solution with the varying electrospinning parameters.

4.1.2 17% PCL concentration solution

For the 17% PCL concentration solution for two parameters provided similar results of helical fiber production of about 44.9%, partially buckled fibers are 33.3% and straight fibers is 21.7%. The similar results were obtained at the flowrate of 0.5ml/hr, flat collector and a both TDC of 10cm and 15cm for each experiment, respectively. However, a slight variation in fiber diameter was observed between both experiments. For the experiment with TDC of 10cm, the fiber diameters where 3.82µm, 2.88µm and 6µm for helical fiber, partially buckled, and straight fibers, respectively. However, for the experiment with TCD of 15cm fiber diameter was 2.56µm, 2.47µm and 3.86µm for helical fiber, partially buckled, and straight fibers, respectively. The results are visualized in figures 4.3 and 4.4.

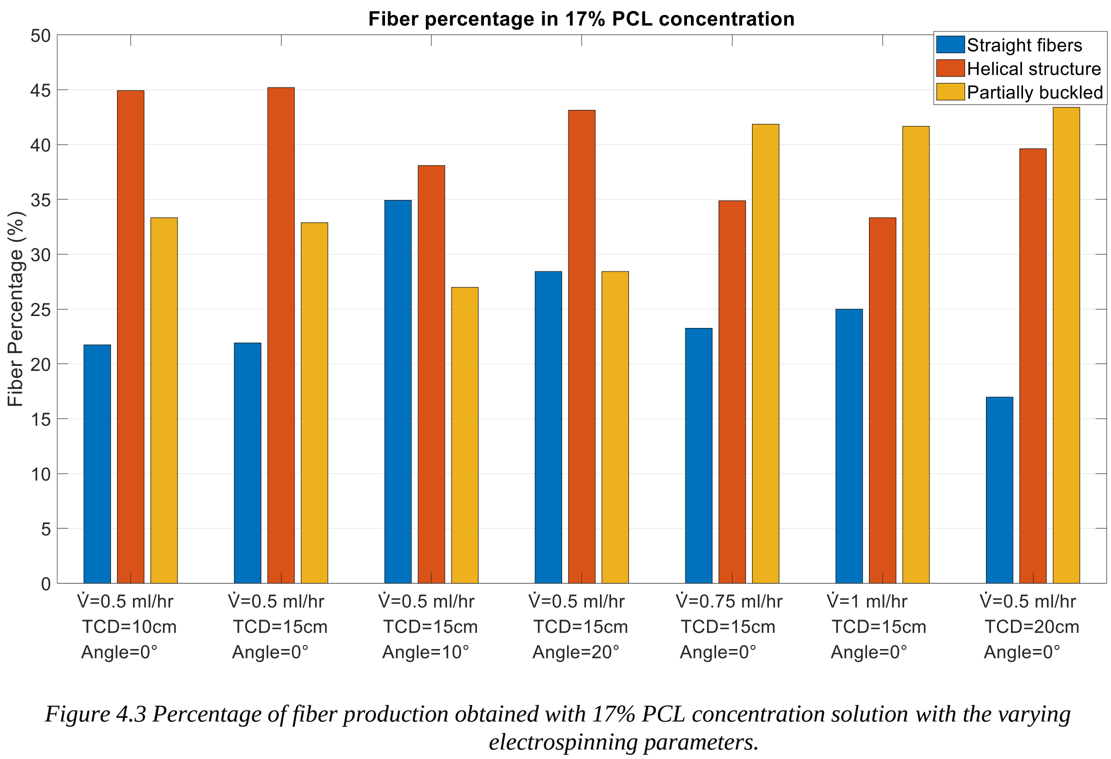

Figure 4.3 Percentage of fiber production obtained with 17% PCL concentration solution with the varying electrospinning parameters.

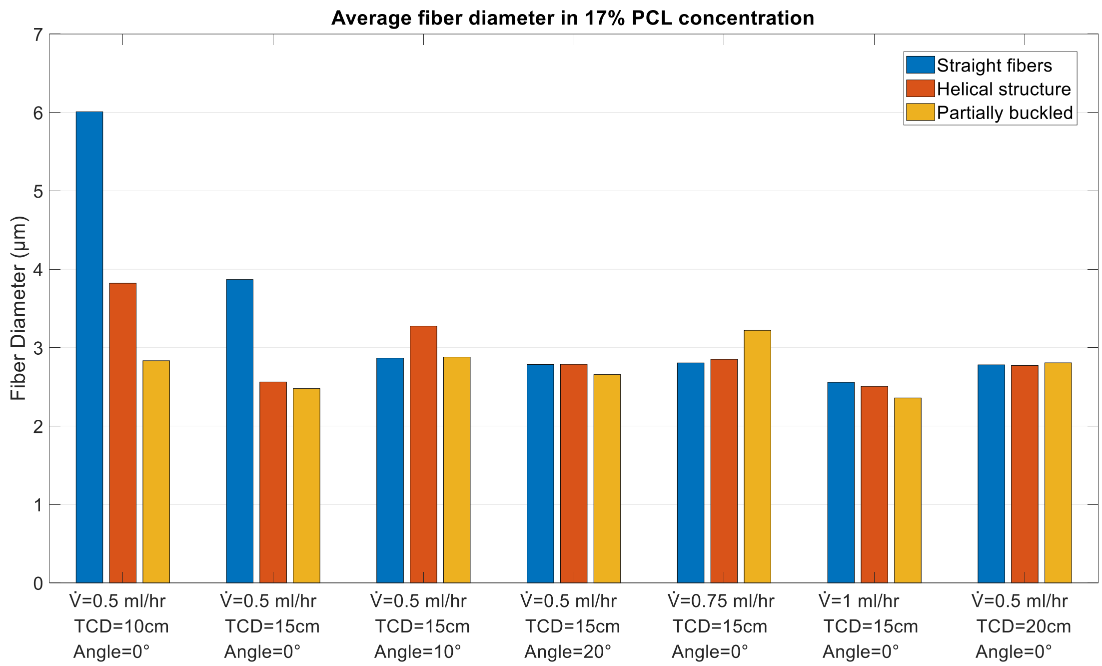

Figure 4.4 Average fiber diameter obtained using 17% PCL concentration solution with the varying electrospinning parameters.

4.1.3 19% PCL concentration solution

Meanwhile for 19% PCL concentration solution, the highest helical fiber production of about 51.5%, obtained with the following parameters of 0.5ml/hr., TCD of 20cm and a flat collector. The results for average fiber structures using 19% PCL concentration is visualized in figure 4.5. Diameters of helical, partially buckled, and straight fibers are 2.3µm, 2.10µm, and 1.79µm, respectively, which is visualized in figure 4.6. While this higher PCL concentration solution resulted in large ratio of helical fiber production, utilizing this concentration provides a challenge due to the solution drying at the needle tip over an extended duration of time.

Another observation, this concentration obtained the highest percentage of straight fiber with a ratio of 82.35%, while is has the lowest production of helical fibers with percentage of 5.88% and 11.76% for partially buckled fibers, respectively. Moreover, the number of beads and beaded fibers increased significantly as the angle of the collector increased, and this observation is shared across all solution concentrations. The beaded structures attained by using 10° angled collector is seen in figure 4.7.

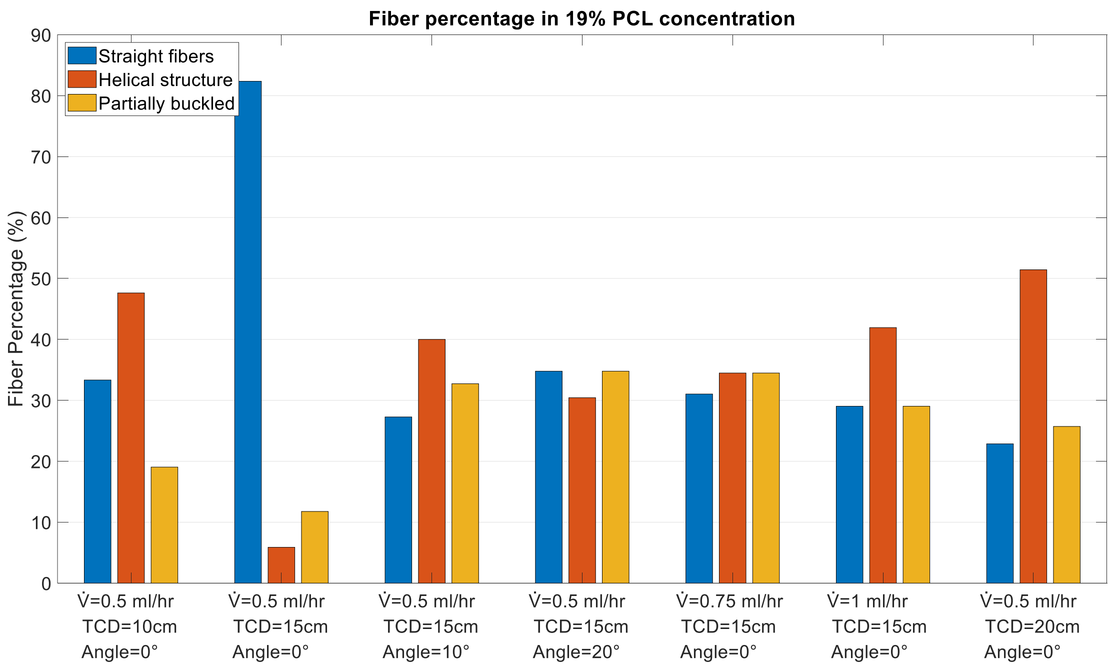

Figure 4.5 Percentage of fiber production obtained with 19% PCL concentration solution with the varying electrospinning parameters.

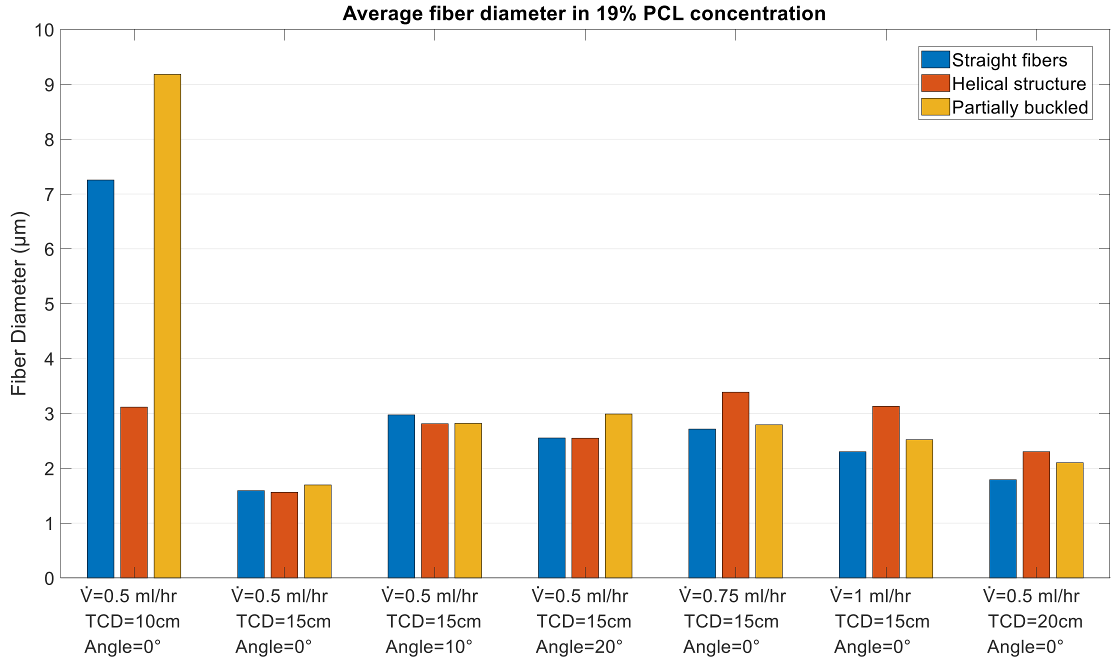

Figure 4.6 Average fiber diameter obtained using 19% PCL concentration solution with the varying electrospinning parameters.

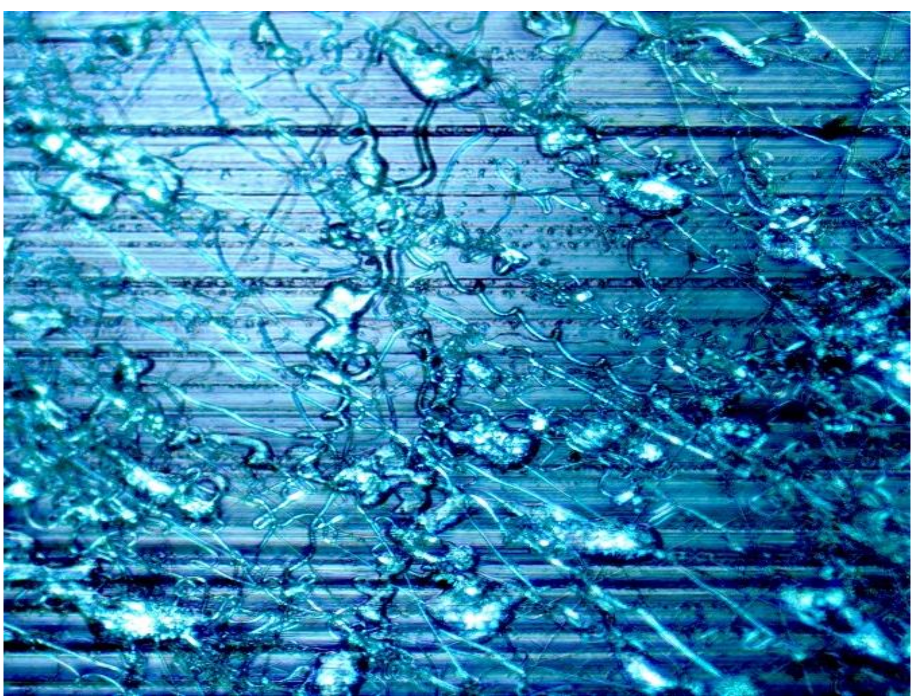

Figure 4.7 Beaded structures obtained due to collector angle of 10° in obtained using 15% PCL concentration solution.

Table 4.1 Summary of experiments performed and observation for each test.

Flowrate	TCD	Angle	Results
15% PCL concentration solution			
0.5	10	0	Helical fibers were more present in the outskirts of the scaffold than center.
0.5	15	0	Helix fibers was equal to the straight fiber production.
0.5	15	10°	Larger production of partially buckled fiber, and beaded structures due to the angle.
0.5	15	20°	High number of beaded structure due to the angled collector.
0.75	15	0	Bead structures are higher when compared to other flat collector experiments.
1	15	0	Significantly high helix fiber production, with a higher presence on the outskirts of the scaffold.
0.5	20	0	Most the fiber are partially buckled.
17% PCL concentration solution			
0.5	10	0	Highest helical fiber production in this solution concentration, and the largest straight fiber diameter.
0.5	15	0	Close percentage of helix fibers as the previous experiment, however the straight fibers diameter is smaller.
0.5	15	10°	Fiber towards the top of the scaffold have a higher straight fiber concentration.
0.5	15	20°	High number of beaded structures spread out on the scaffold, with a high helix production toward the middle and the end of the scaffold.

0.75	15	0	Number of partially buckled fiber is higher than other parameters utilizing this concentration.
1	15	0	Number of partially buckled fiber is high, along with the smallest average fiber diameter in this concentration.
0.5	20	0	Highest percentage of partially buckled fibers.
19% PCL concentration solution			
0.5	10	0	Considerably larger fiber diameter, specifically partially buckled fibers.
0.5	15	0	Noticeably smaller fiber diameter, with most of the fibers having a straight structure.
0.5	15	10°	Bead structures are present, however secondary to other solution concentrations.
0.5	15	20°	Bead structures are present in larger footprint.
0.75	15	0	Helix fiber structure is on average spread throughout the scaffold.
1	15	0	Helix fiber production increased slightly.

4.2 Temperature controlled study

It was observed that 30°C, flowrate 1ml/hr and TCD of 15cm produced the largest number of helical fibers at 38.1%, partially buckled fibers of 38.1% and 23.7% straight fibers. The average fiber diameter observed was 17.72µm, 16.88µm and 16.38µm for helical fiber, partially buckled, and straight fibers, respectively. While at 20°C the highest percentage of partially buckled fiber were obtained using flowrate of 0.75ml/hr and TCD of 15cm.

Meanwhile, the diameter average measured was 11.43µm, 16.63µm and 13.38µm for helical fiber, partially buckled, and straight fibers, respectively. In conclusion the results were subpar when compared to room temperature environment. The rationale behind the results was due to the direct temperature controlled utilized where the air flow affected the fiber formation and decreased the buckling probability.

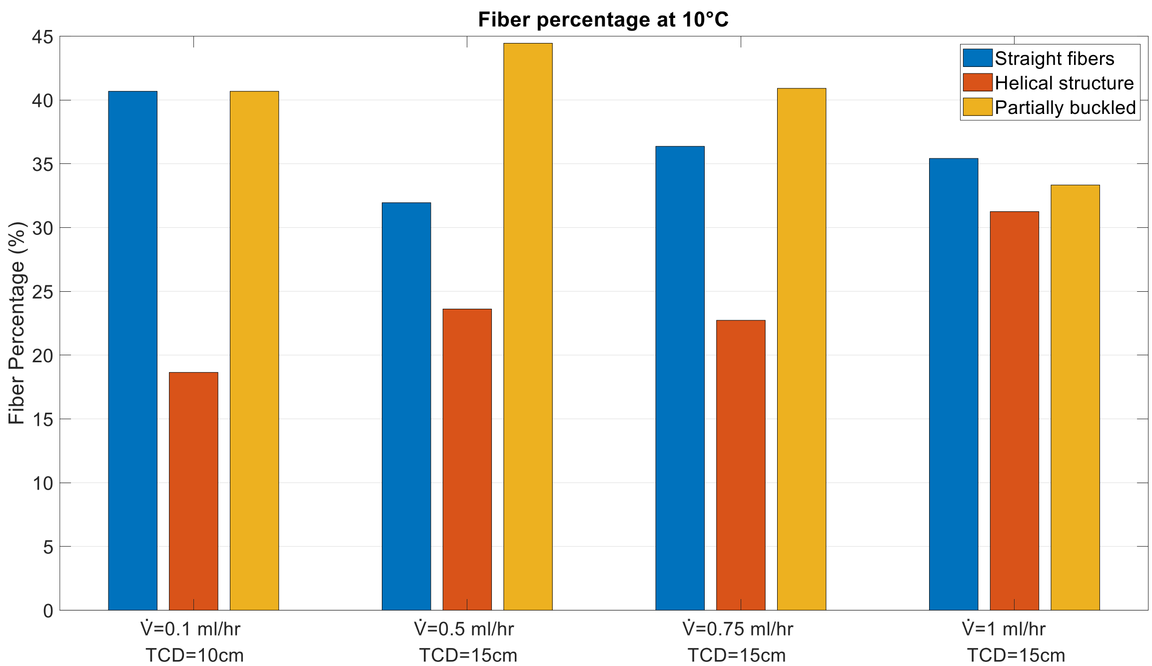

Figure 4.8 Percentages of fiber types at controlled 10°C with varying electrospinning parameters.

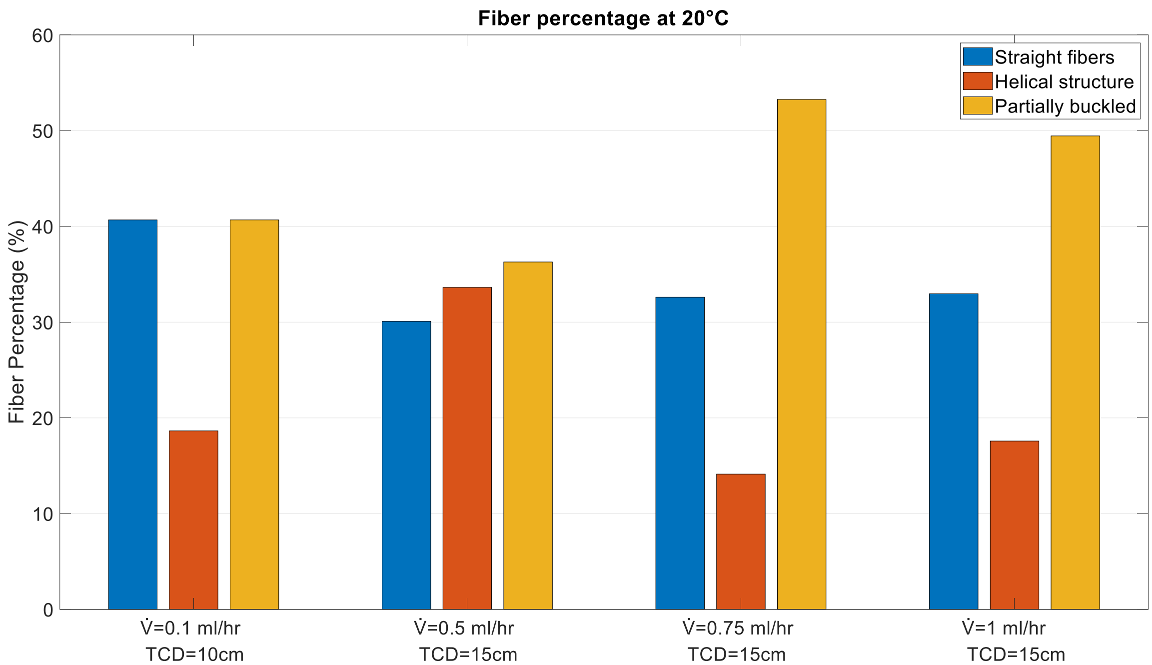

Figure 4.9 Percentages of fiber types at controlled 20°C with varying electrospinning parameters.

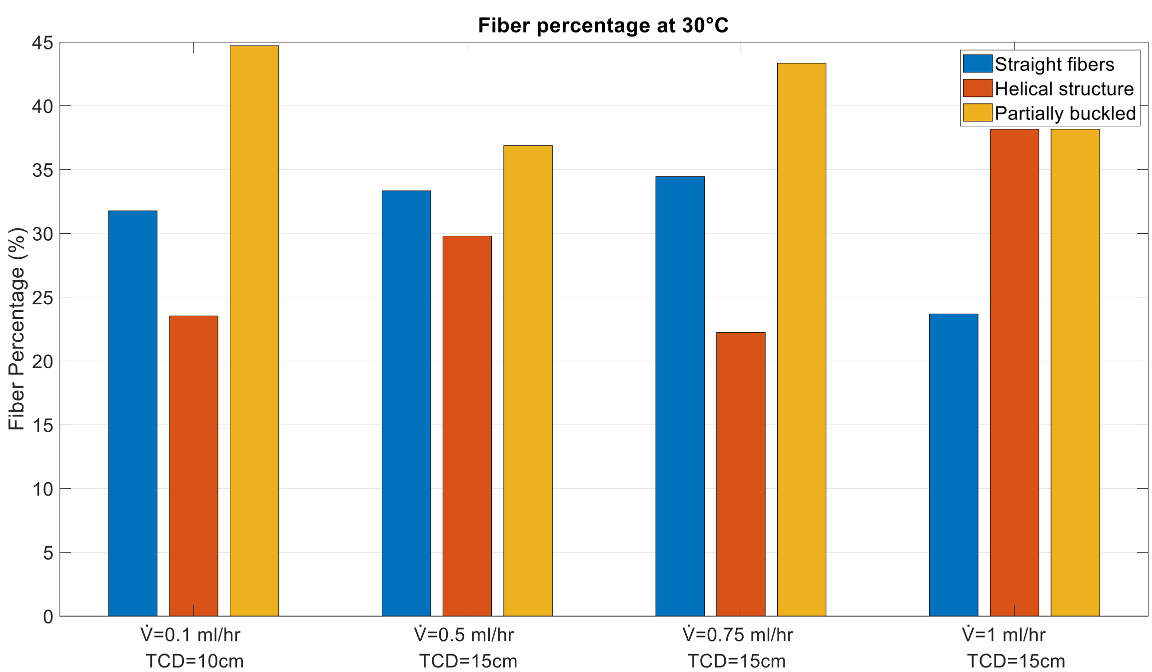

Figure 4.10 Percentages of fiber types at controlled 30°C with varying electrospinning parameters.

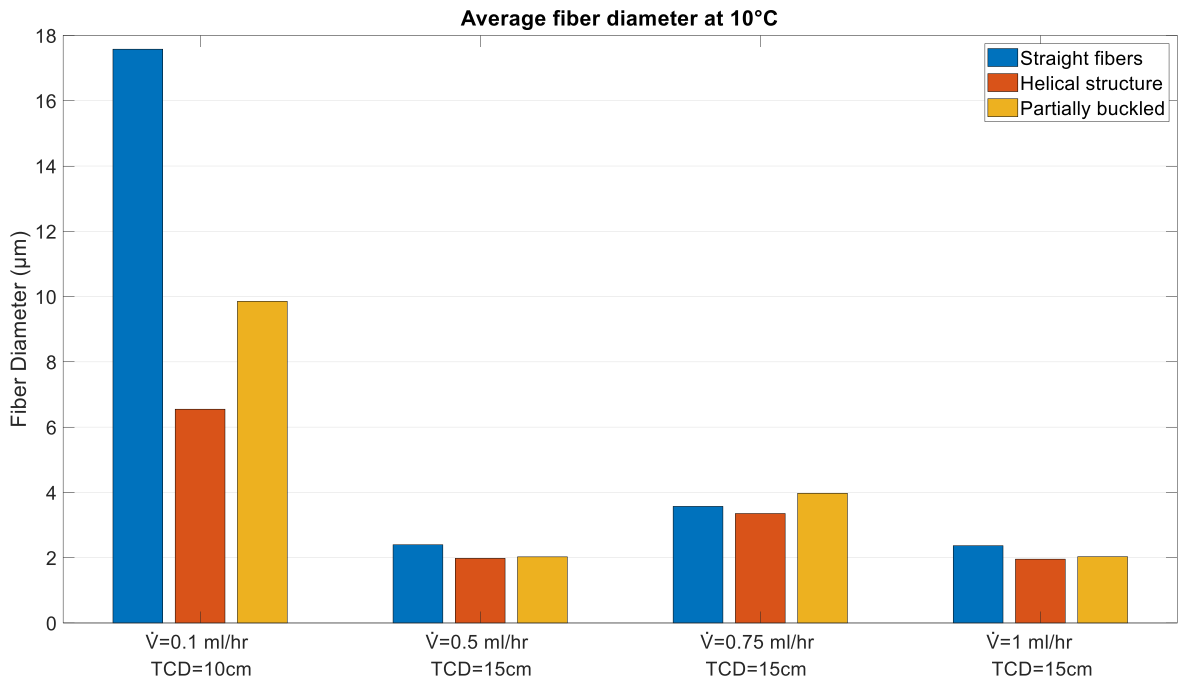

Figure 4.11 Average fiber diameter obtained at 10°C with varying flowrates and TCD.

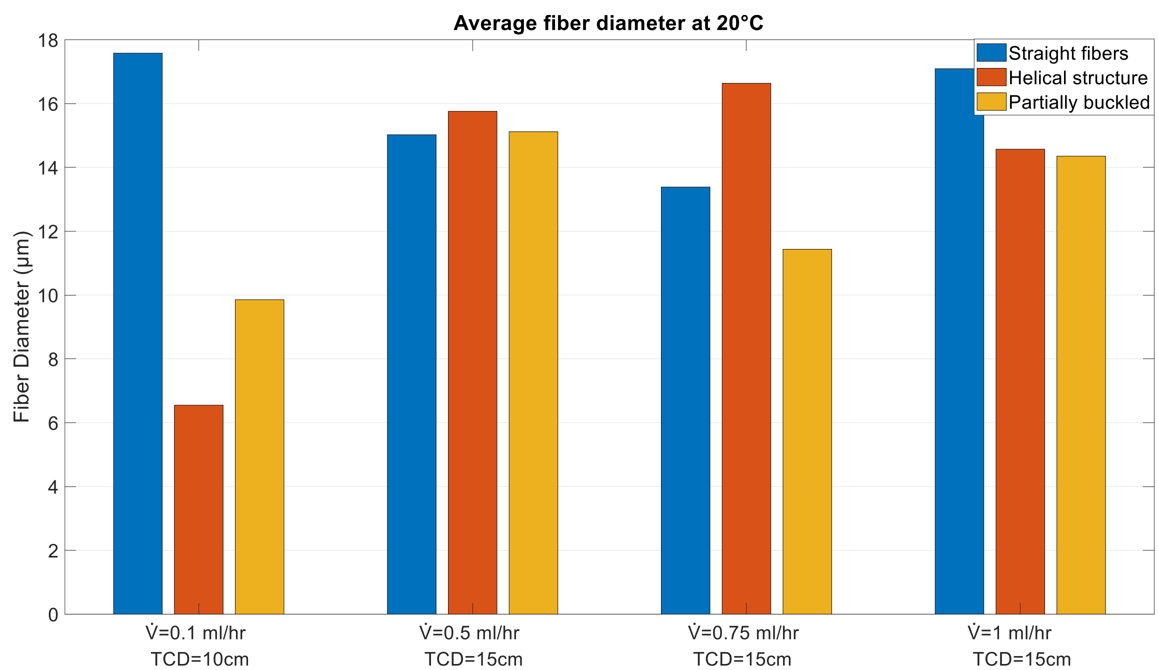

Figure 4.12 Average fiber diameter obtained at 20°C with varying flowrates and TCD.

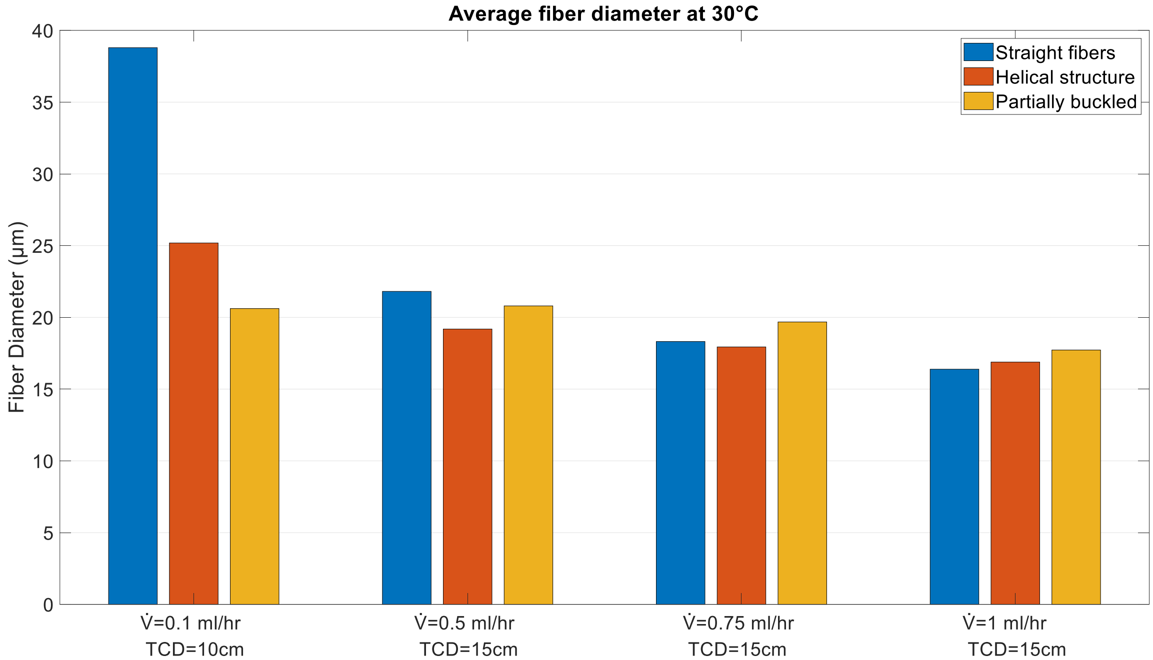

Figure 4.13 Average fiber diameter obtained at 30°C with varying flowrates and TCD.

Conclusion: *Based on our parameters sensitivity study conducted it was observed that for PCL electrospinnig solutions the following parameters are result in optimal helical fiber production at the solution concentration of 15%: TCD = 15cm, flow rate =1ml/hr and angle of 0°. Based on the analysis conducted 60% of helical fibers, 22% partially buckled fibers and 18% straight fiber were achieved. The optimal parameters were adopted in the temperature-controlled study.*

5. Mechanical characterization

Summary: *Attaining a scaffold with mechanical properties aligning with the native tissue is crucial for a successful scaffold. A study is conducted to characterize the helical electrospun scaffold manufactured using the optimal parameters from the previous study. Focus of this study are the hyperelastic and viscoelastic behavior of the material. The characterization is performed using a uniaxial tensile testing method. Every loading scheme designed highlighted a behavior of interest. Furthermore, the scaffolds are examined at two different speeds of 0.1mm/s and 0.01mm/s pre and post conditioning. Sample recovery after 24 hours of testing is explored as well. Fianlly, coupons behavior to fractured is also captured in latter tests.*

5.1 Stress strain behavior

Test samples were subjected to 10% strain and 20% strain in two different loading schemes. Conditioning the sample consists of stretching the sample to the desired strain level and unloading for 20 consecutive cycles. In both loading schemes it was observed that samples are subjected to buckling during the conditioning section of the test. Due to the buckling that occurs, the initial steps results in negligible stress till the sample is stretched adequately to achieve stress levels. Figures 5.1 and 5.2 illustrates the stress strain behavior of the material pre and post conditioning at 10% strain and 20% strain respectively. The negative stress values attained during the buckling portion of the postconditioning loading was neglected in the results. Strain was calculated starting with the unbuckled segment of the test.

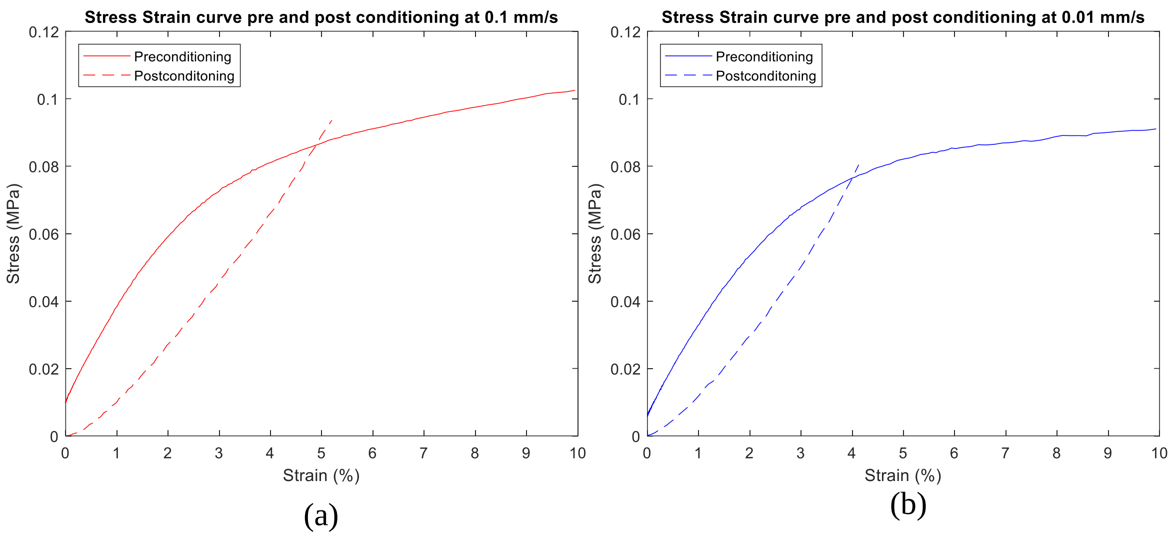

Figure 5.1 Stress strain curve up to 10% strain of the pre and post conditiong of the sample (a) at 0.1mm/s and (b) at 0.01mm/s where the preconditioned is denoted by solid line and post conidtioned denoted by dashed line.

Examining the stress strain curve pre and post conditioning, an observation can be made that the material experience significantly different behaviors. Preconditioned and postconditioned behavior, the material behaves as elastomers. However, postconditioning the behavior of the material changes drastically, this can be theorized due to the rearrangement of the fibers after the initial stretch.

Another observation made is that the scaffold experiences plastic deformation during the conditioning portion of the loading scheme. The deformation is the main reason buckling of the samples occurs. Furthermore, the degree of the plastic deformation is dependent on the maximum strain rate and loading speed. As for 0.01mm/s experienced 1.64mm of deformation post conditioning at 10% strain, while test coupons at 0.1mm/s conditioned at 10% resulted in 1.34mm in deformation. While conditioning to 20% resulted in larger deformations. At loading speed of 0.1mm/s the deformation of the sample was at 3.17mm and 3.19mm for the 0.01mm/s. Moreover, considering both strain levels tested, it can be concluded that electrospun scaffolds are strain rate sensitive. The stress levels achieved in postconditioned samples at 20% strain exceeded the preconditioned samples significantly, as seen in figure 5.2, when compared to the 10% strain tests, seen in figure 5.1.

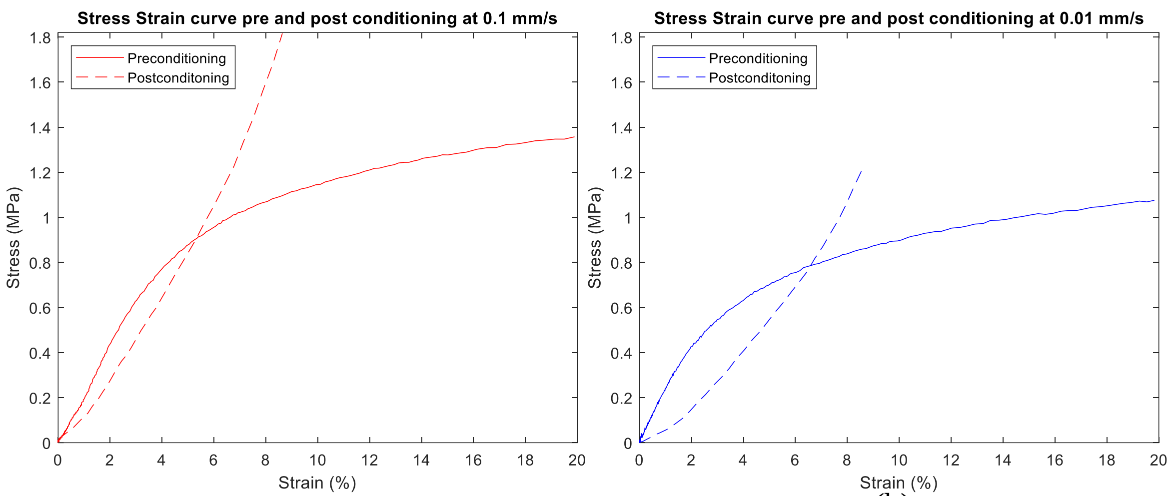

(a) (b)

Figure 5.2 Stress strain curve up to 20% strain of the pre and post conditiong of the sample (a) at 0.1mm/s and (b) at 0.01mm/s where the preconditioned is denoted by solid line and postconditioned denoted by dashed line.

5.2 Hyperelastic and viscoelastic behavior

Both electrospun and solid samples experienced significant stress softening and stress relaxation at both loading speeds tested (0.01mm/s and 0.1mm/s). Owing to the nature of the scaffolds in tissue regeneration, application requires preconditioning before implantation [57]. Examining the data, it is evident that the first cycle of loading has a noticeable loading effect compared with consecutive cycles—in the later cycles, the material experiences behavior resembling that of rubber materials. This behavior is due to stretching of the helical fibers and the subsequent breakdown of weaker bonds between the fibers within the scaffold matrix. Nonetheless, as the cycles continue, a further stress softening effect is witnessed until it reaches a stable level in later cycles. Figures 5.3 (a) and (b) show the samples being exposed to the same loading conditions as those in the previous cycle; however, the exact strain levels cannot be reached, and there is a clear negative regression line between the stress peaks.

Stress relaxation effect and stress recovery phenomena are evident in both the electrospun and solid samples at both loading speeds. In addition, both the effect and the phenomena can be clearly highlighted after the last cycle during the constant strain on the sample. Stress softening effect can be seen as the cycles develop the peak stress decreases in each cycle. Where the phenomena can be observed as a drop in the stress value in the last cycle during the static strain loading. A constant strain applied to the samples allows a slow deflation of stress over time: electrospun samples experienced a 19.3% and 13.5% drop in the stress levels, between the cycle peak and end of duration, at 0.1mm/s and 0.01mm/s, respectively. This result agrees with several findings in different fields indicating that stress relaxation increases at higher loading speeds. The stress softening effect can be eliminated in rubber materials by subjecting samples to cyclic loading; however, the effect is eliminated at later loading cycles. The results outlined represent the same conclusions, as stress softening is further minimized as the cycles progress, and a stable level can be achieved at the 18th cycle at a loading speed of 0.1mm/s. Meanwhile, samples tested at 0.01mm/s experienced softening in the last cycle tested and thus the effect may be present after 20 cycles of loading. We observed that a slower loading speed tends to increase the softening effect in the material.

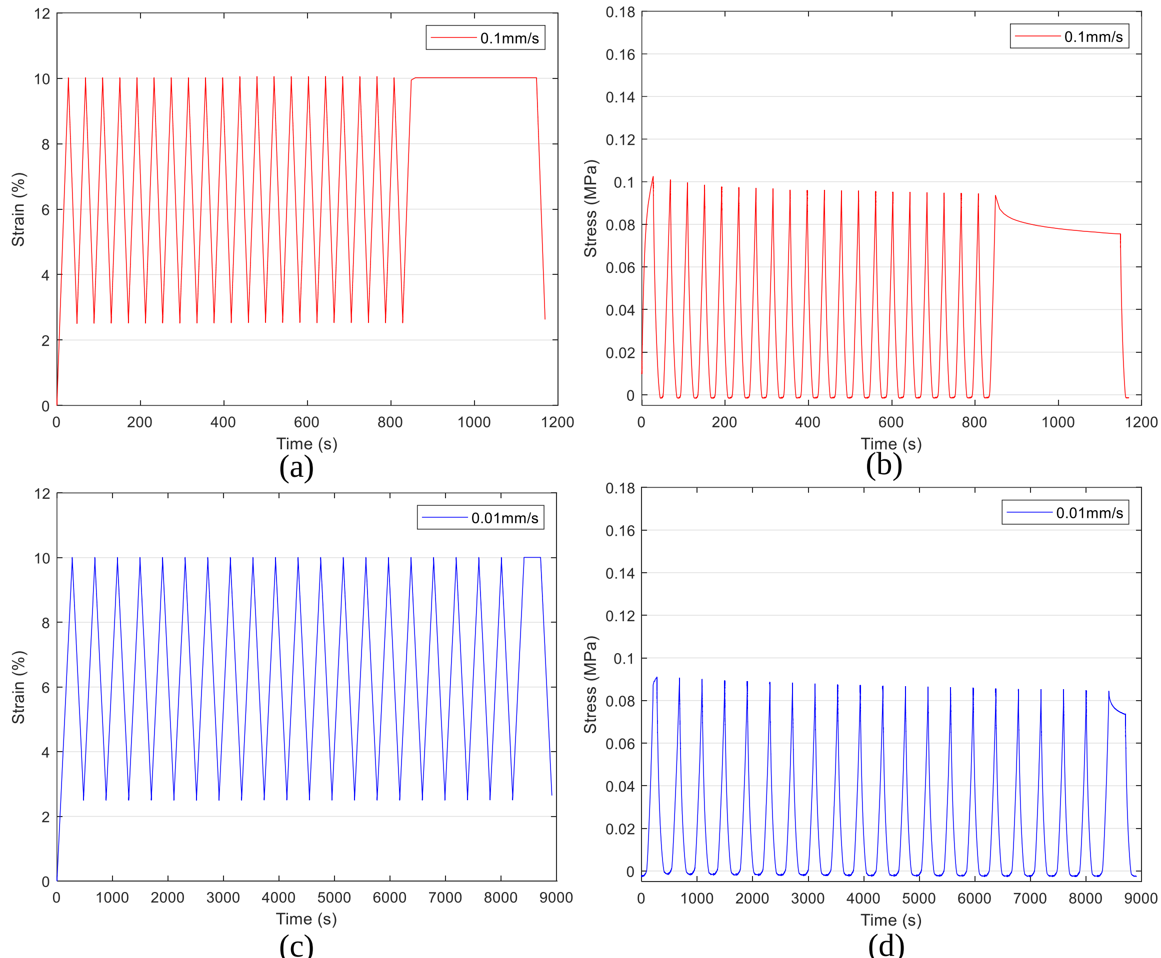

Figure 5.3 Electrospun samples subjected to 20 cycles of cyclic loading and subsequently constant strain: (a) and (c) strain over time (cause) to demonstrate loading during the experiment at loading speeds of 0.1mm/s and 0.01mm/s, respectively; b) stress over time at 0.1mm/s; (d) stress over time at 0.01mm/s.

Figure 5.4 shows that solid samples exhibited behavior similar to that of electrospun samples. By examining the samples at both speeds, we witnessed a drastically different behavior after the first cycle (figure 5.3 (a)). As mentioned previously, the stress softening phenomenon is more obvious after the initial loading, and after some cycles, this behavior lapses. The samples tended to experience some stability in properties at more mature cycles. As it can be seen in figure 5.3 (a), the stress induced in the samples tended to stabilize, with a slight decrease in the stress values around the 18th cycle at 0.1mm/s loading speed and in the last tested cycle at 0.01mm/s loading speed. The same downward regression line of peak stress in each cycle is also illustrated in the solid samples, the same as was observed for the electrospun samples. Stress relaxation is also present in the solid samples. The same trend can be seen in both figures 5.4 (b) and (c) when comparing the fibrous scaffolds. Solid coupons experienced a stress relaxation of ~20.7% decrease at 0.1 mm/s and a 15.7% drop at 0.01mm/s. A correlation between the decreasing loading speed and the increasing softening effect was observed.

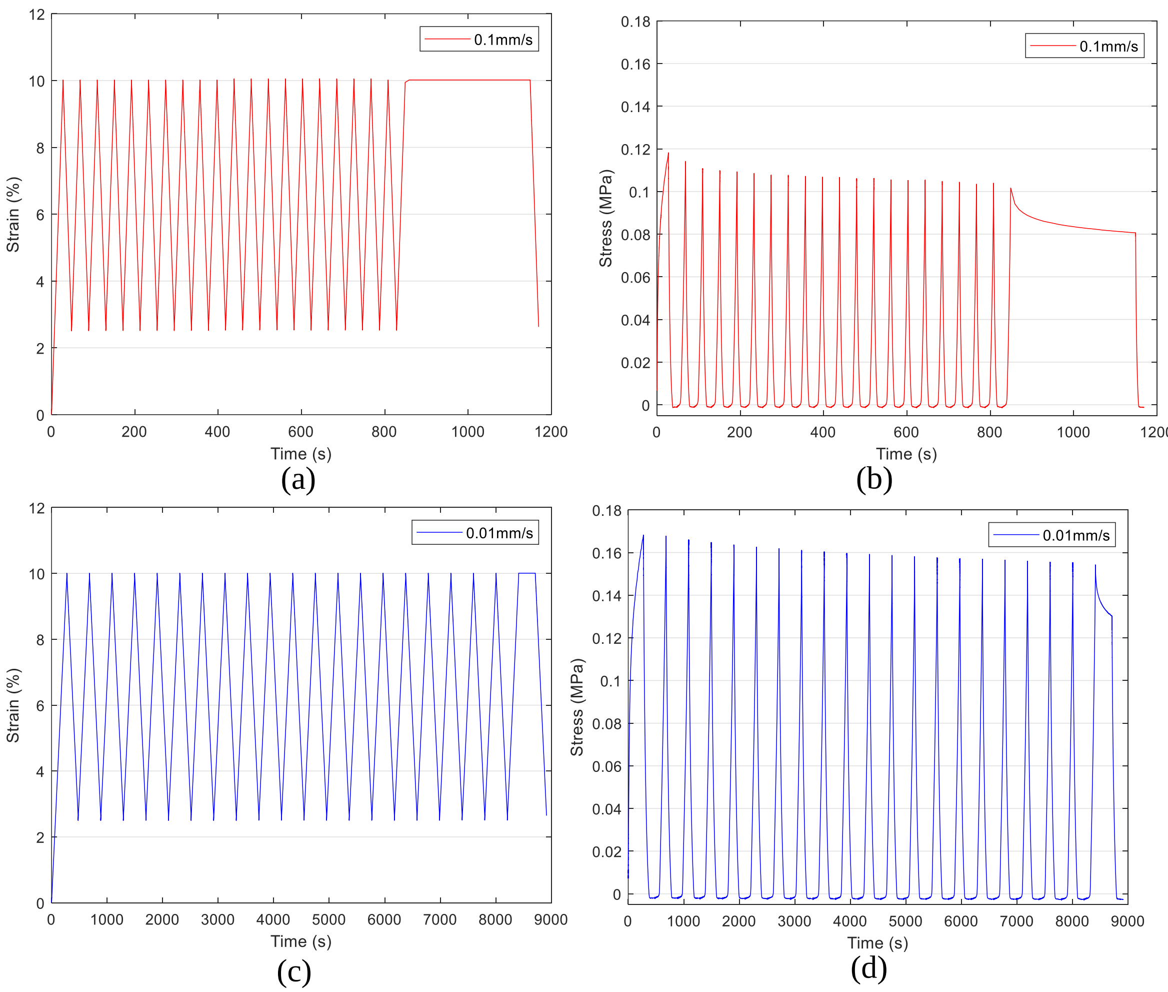

Figure 5.4 Solid samples subjected to 20 cycles of cyclic loading and subsequently constant strain over time: (a) and (c) strain over time (cause) to demonstrate loading during the experiment at loading speeds of 0.1mm/s and 0.01mm/s, respectively; (b) stress over time at 0.1mm/s; and (d) stress over time at 0.01mm/s.

5.3 Multistep loading

5.3.1 Preconditioning multistep loading

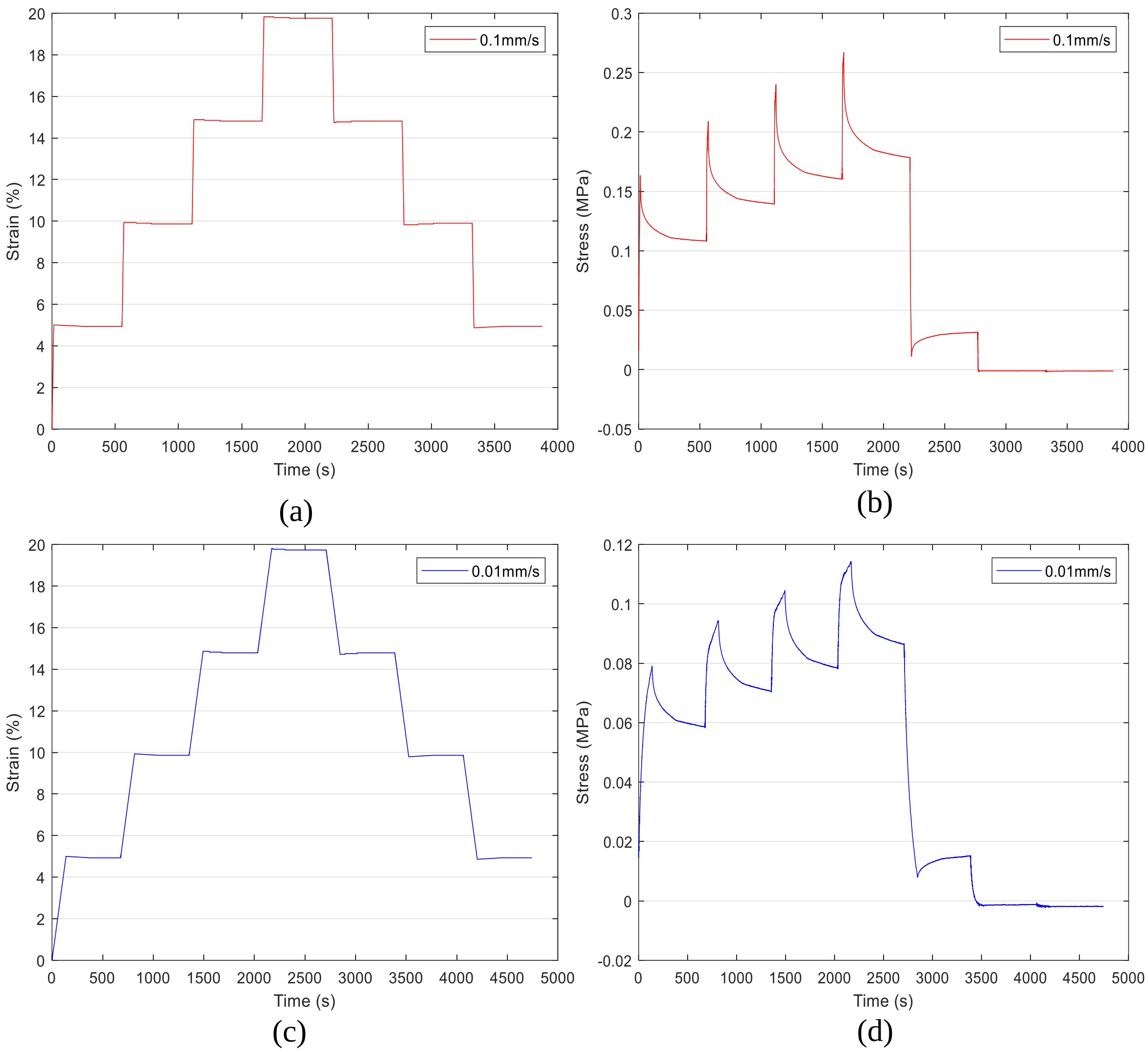

Figure 5.5 Electrospun samples subjected to multi-step loading and unloading to examine stress softening: (a) and (c) strain over time (cause) to demonstrate loading during the experiment at loading speeds of 0.1mm/s and 0.01mm/s, respectively; (b) stress over time at 0.1mm/s; (d) stress over time at 0.01mm/s.

Stress relaxation is obvious in electrospun samples at higher strains and at both loading speeds tested. figure 5.3 (a) and figure 5.3 (b), represents the loading scheme (cause of deformation) for the experiments at both speeds. At a loading speed of 0.1mm/s, the stress relaxation is apparent at every strain level during the ascending portion of the test. Moreover, the gradual drop in stress during relaxation is greater at higher strain levels. Examining the results further, we see that because of the extended duration of relaxation, stable stress levels can be determined at every level. Furthermore, comparing stress relaxation percentages, points between the peak stress value and valley, between each strain step the percentage during the first step was significantly lower than that during the other steps, with a 20.7% drop. The stress relaxation percentage from the second step onwards reached a constant level of relaxation, with ~33% drop in stress values. Meanwhile, solid samples had similar results at higher stress values. However, the stress relaxation percentage at each strain step was a more consistent value of 36.5%, compared with (the corresponding) samples with helical fibers. Subsequently, most of the descending steps, except for the first step at 15% strain, had no stress values. These results shows that excessive stretching and thus deformation of the sample causes buckling of the sample. Owing to the low speed tested (0.01mm/s), the strain increase was at a slope with respect to time; this effect is illustrated in figure 5.5 (c) for electrospun samples and figure 5.6 (c) for solid samples. Because of the lower loading speeds, stress relaxation commenced before reaching the final strain percentage of each step.

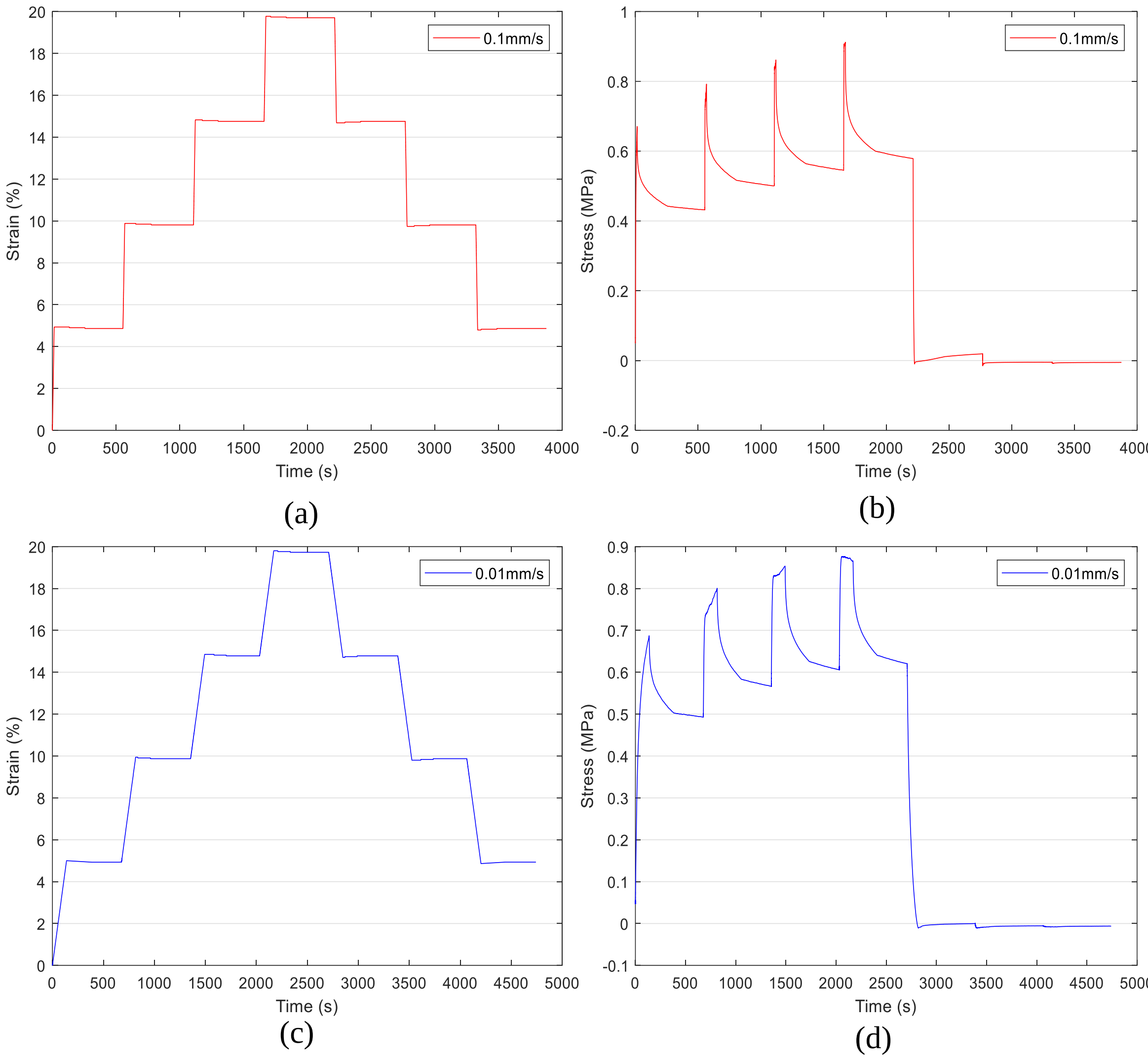

Figure 5.6 Solid samples subjected to multi-step loading and unloading to examine stress softening: (a) and (c) constant strain over time (cause) to demonstrate loading during the experiment at loading speeds of 0.1mm/s and 0.01mm/s, respectively; (b) stress over time at 0.1mm/s; (d) stress over time at 0.01mm/s.

5.3.2 Postconditioning multistep loading

A postconditioning multistep loading test (figure 5.7) was conducted to examine the stress softening effect present at 20% strain. The outlined testing protocol also highlighted stress relaxation effect by eliminating the stress softening phenomenon prior to the multistep loading. Similar trend to 10% strain cyclic loading is observed at 20% strain loading, where a downward regression line is observed when comparing the peak normalized stress value to the values of the later cycles. However, a sharper decline in stress values can be seen at 0.1mm/s loading speeds, when comparing between the normalized stress value in the first cycle and values of stabilized mature cycles. Although 0.01mm/s loading speeds, has not illustrated the same observations mentioned, the trendline is mimicking the 10% cyclic strain pattern discussed earlier. The stress softening effect has witnessed a drop of 9% and 5.33% for 0.1mm/s and 0.01mm/s respectively, between the peak stress value achieved and the minimum peak load value. During the multistep loading test at both tested speeds, the first two loading steps of 5% and 10% strain did not result in any stress value due to the plastic deformation of the coupon. Nevertheless, the 15% strain step resulted in minimal stress reaction and a stress relaxation is evident during the static strain subjected. Another observation when examining the 0.1mm/s test results was that at 20% strain loading the resulting stress was higher at the peak when compared to the last cycle of the cyclic loading. However, results of the 0.1mm/s loading approximately reached the same level as the last cycle. Moreover, the stress relaxation was at 18.9% and 13.2% for 0.1mm/s and 0.01mm/s, respectively. Consequently, a significant result must be highlighted derived from the combined loading test conducted was the stress relaxation effect on the electrospun samples. The initial loading stages of the multistep loading segment of the test served as a relaxation period for the already deformed coupons. The relaxation effect facilitated the samples achieving higher stress levels that the last cycle during the cyclic loading portion of the test at 0.1mm/s loading speed. On the other hand, the stress values of the 0.01mm/s loading speed did not exceed the levels of the step during cyclic loading.

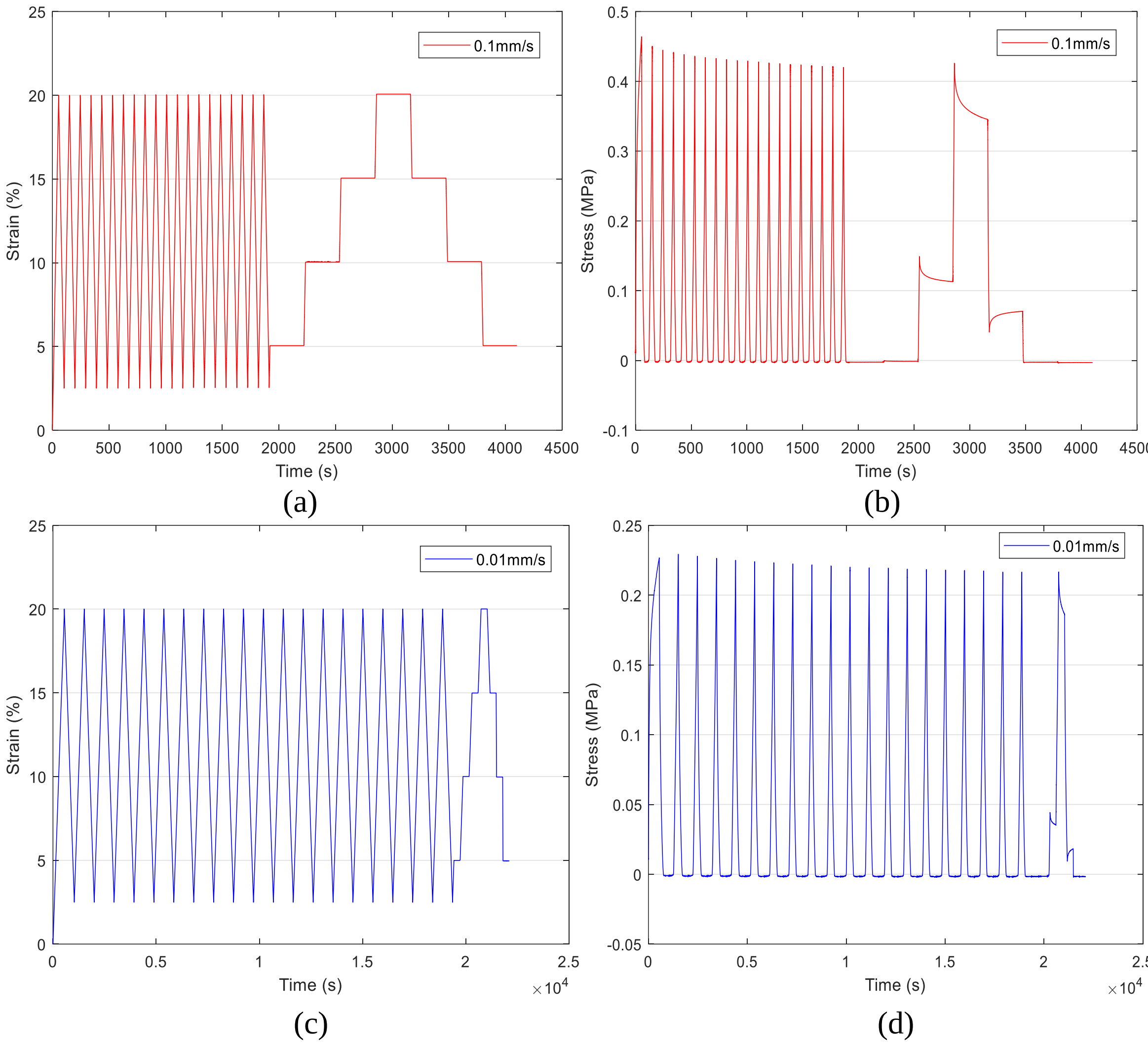

Figure 5.7 Electrospinning samples testing that combines cyclic loading and multi-step loading: (a) and c) strain over time (cause) to demonstrate loading during the experiment at loading speeds of 0.1mm/s and 0.01mm/s, respectively; (b) stress over time at 0.1mm/s; (d) strain over time at 0.01mm/s.

5.4 Deformation recovery

Sample recovery is a phenomenon that most soft material experience. Generally, elastomers recovery form the deformation sustained during loading [62]. It was observed that helical electrospun scaffolds experience some degree of recovery. Figure 5.8, a sample measured directly after conditioning to 20% strain, then loading and subsequently relaxation of 2000s. The original length of the sample before any testing conducted was 27.9mm and after subjected to the previously mentioned loading scheme the length was 31.15mm which denotes 11.6% deformation in length. The sample was left to relax in room temperature for 24-hour period and measured again, resulting in 29.57mm of length. Translating into only a 5.98% deformation from the original length and a recovery of 5.6% from the length attain following testing.

(a) (b)

Figure 5.8 Helical fibered sample measured (a) after testing at loading speed of 0.1mm/s, and (b) subsequent to 24-hour recovery in room environmentconditions.

5.5 Fracture behavior

Based on the previous tests, it was observed that the material behaves in a different manner when subjected to conditioning. The conditioning causes the stress-strain curve to deviate from the conventional hyperelastic curve. Analyzing the post conditioning samples curve, the curve tends to increase with a positive almost linear slope, and subsequently the behavior shifts to an almost linear increase in stress-strain curve. However, in all the tests conducted at high strain rates, the test was stopped due to the coupons failing from the grips.

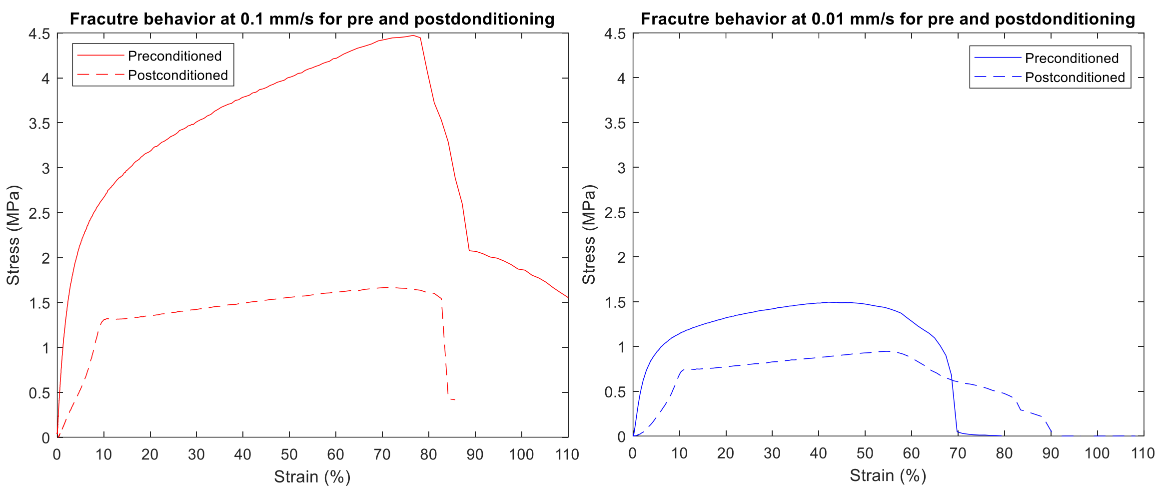

(a) (b)

Figure 5.9 Samples were tested to failure, where all samples failed from the grips. (a) represents testing at 0.1mm/s loading speed pre and post conditioning, and (b) represents testing at 0.01mm/s loading speed pre and post conditioning.

Conclusion: *Various tests were conducted to analyze the mechanical properties of the helical electrospun scaffolds. Examining the stress strain curves of two different strain rates, highlighted the strain rate effect present in the samples. Another observation deduced from the previously mentioned curves was the drastic change in behavior of samples post conditioning. Further testing was commenced to highlight the stress recovery, relaxation and stress softening phenomena. The results concluded the three previously mentioned phenomena are present and apparent in the scaffolds. Sample recovery was also examined in a sample that was subjected to conditioning, and a degree of conditioning was present over 24-hour recovery period. Lastly, coupons were tested to fracture in both preconditioned and postconditioned states. It was observed that post conditioning the samples experience a shift in the stress strain curve beyond a certain limit where the stress increases linearly.*

6. Numerical modeling of scaffolds

Summary: *This chapter summarizes the stable theoretical models utilized in modeling both the hyperelastic behavior and viscoelastic response. Subsequently the applied load and the material response is discussed and visualized. Finally, the modeling of the hyperelastic and viscoelastic experimental data are evaluated for both speeds. Preconditioned and postconditioned samples are also analyzed.*

6.1 Numerical theories and models

6.1.1 Hyperelastic models

Strain energy density function may define the isotropic elastic properties through a hyperelastic material modeling. The function is defined as material per unit volume which includes energy stored due to volumetric changes (Ψ_{vol}) and elastic energy of deviatoric deformation (Ψ_{dev}), the strain energy (Ψ) is as follows:

$$\Psi = \Psi_{dev}(I_1, I_2, I_3) + \Psi_{vol}(J) \tag{6.1}$$

Cauchy-green deformation tensors are I_1, I_2 and I_3 and determinant of the deformation tensor is J. Deformation tensor first, second and third invariants are expressed in terms of stretches in principle directions λ_1, λ_2, and λ_3.

$$I_{3}{=}\lambda_1{}^2 + \lambda_2{}^2 + \lambda_3{}^2 \tag{6.2a}$$

$$I_{2}{=}\lambda_1{}^2\lambda_2{}^2 + \lambda_2{}^2\lambda_3{}^2 + \lambda_3{}^2\lambda_1{}^2 \tag{6.2b}$$

$$I_{1}{=}\lambda_1{}^2\lambda_2{}^2\lambda_3{}^2 \tag{6.2c}$$

- *Ogden*

A hyperelastic constitutive model for elastomers that are incompressible was proposed by Ogden when experiencing large deformations [63]. The model is defined through stretches in principal directions as follows:

$$\Psi_{OG} = \sum_{i=1}^{N} \frac{2\mu_i}{\alpha_i^2}\left(\lambda_1^{-\alpha_i} + \lambda_2^{-\alpha_l} + \lambda_3^{-\alpha_l} - 3\right) + \sum_{i=1}^{N} \frac{1}{D_i}(J^{el} - 1)^{2i} \tag{6.3a}$$

N is the order of the Odgen function, μ_i, αi , and D_i are temperature dependent material properties and J^{el} is the elastic volume ratio. While the bulk modulus and shear modulus are defined as:

$$\mu_0 = 2\sum_{i=1}^{N} \mu_i \tag{6.3b}$$

$$K_0 = \frac{2}{D_1} \tag{6.3c}$$

- *Arruda-Boyce*

For larger strains behaviors in elastic materials Arruda Boyce deduced a constitutive model. The model captures an 8-chain representation of the volume structure of the material. Where, the volume element is embodied with 8 chains connected from the edges to the center [64]. The strain energy potential for the Arruda Boyce model stated by the following:

$$\mathrm{U} = \mu\sum_{\mathrm{i}=1}^{5} \frac{\mathrm{C_i}}{\lambda_{\mathrm{m}}^{2\mathrm{i}-2}}\left(\mathrm{I}_1^{-\mathrm{i}} - 3^{\mathrm{i}}\right) + \frac{1}{\mathrm{D}}\left[\frac{\mathrm{J_a^2} - 1}{2} - \mathrm{L\,n}(\mathrm{J_{al}})\right] \tag{6.4a}$$

$$\mathrm{C_1} = \frac{1}{2}, \mathrm{C_2} = \frac{1}{20}, \mathrm{C_3} = \frac{11}{1050}, \mathrm{C_4} = \frac{19}{7000}, \mathrm{C_5} = \frac{519}{673750} \tag{6.4b}$$

where μ is the initial shear modulus, l_m is defined as the locking stretch and D captures inverse of the bulk modulus at small strains.

- *Van Der Waals:*

The model is also known as the Kilian model and is identified as follows:

$$U = \mu\left\{-(\lambda_m^2 - 3)[\mathrm{Ln}\,(1-\eta) + \eta] - \frac{2}{3}a\left(\frac{\tilde{I} - 3}{2}\right)^{\frac{3}{2}}\right\} + \frac{1}{D}\left(\frac{J^2 - 1}{2} - \mathrm{Ln}\,(J)\right) \quad (6.5a)$$

$$\bar{I} = (1-\beta)I_1 + \beta\bar{I}_2 \text{ and } \eta = \sqrt{\frac{I - 3}{\lambda_m^2 - 3}} \quad (6.5b)$$

where D in this form captures the compressibility of the material and β defines the linear mixture parameters. It is recommended to set $\beta = 0$ to neglect due to the impact on deviatoric Cauchy Green tensor in $\tilde{I}$, when only a single set of test data are provided

- *Reduced polynomial*

This model is derived from the conventional polynomial model, with a single modification on omitting the second invariant of in the left-hand side of the Cauchy Green tensor [65]. Thus, the potential strain energy is defined as:

$$U = \sum_{i=1}^{N} C_{i0}\left(\bar{I}_1 - 3\right)^2 + \sum_{i=1}^{N}\frac{1}{D_i}(J_{al} - 1)^2 \quad (6.6)$$

the reduced polynomial model is governed by N where it is the order of the function. In this study, N=1 and N=2 provided stable models.

- *Yeoh (Reduced polynomial N=3)*

A special form of the reduced polynomial is derived with three term expansion. Yeoh strain energy potential depends mainly on the first invariant of deformation tensor (I_1). The function is defined as:

$$\Psi_{YH} = C_{10}(I_1 - 3) + C_{20}(I_1 - 3)^2 + C_{30}(I_1 - 3)^3 + \frac{1}{D_1}(J^{el} - 1)^2 + \frac{1}{D_1}(J^{el} - 1)^4 + \frac{1}{D_1}(J^{el} - 1)^6 \quad (6.7a)$$

where C_i and D_i are temperature-dependent parameters, and J_{el} is the elastic volume ratio. The shear modulus and the bulk modulus are given by:

$$\mu_0 = 2C_{10} \quad (6.7b)$$

$$K_0 = \frac{2}{D_{10}} \quad (6.7c)$$

6.1.2 Viscoelastic models

- *Prony series*

To accurately predict and simulate the viscoelastic behavior of the electrospun scaffold, the modeling is based on the Prony series function has been utilized. It is only applicable for one-dimensional relation test. The equation defining the model is as follows:

$$G(t) = G_\infty + \sum_{i=1}^{N} G_i \exp\left(-t/\tau_i\right) \quad (6.8a)$$

in this function, G_∞ is the long-term modulus when the material is fully relaxed and $\tau_i$represents the relaxation time. Where the minimization of the parameters G_∞, G_i and τ_i is favored to minimize the error during curve fitting.

$$G(t) = G_0 - \sum_{i=1}^{N} G_i[1 - \exp(-t/\tau_i)] \quad (6.8b)$$

this derivation of the function is more suitable to be utilized by commercial software for predicting the material coefficients. Where G_0, is attained from independent data from the relaxation data [66]. Lastly, i=1,2…,N is the number of terms in the Prony series. Though there is no restriction, N=1 has been selected due to the adequate results provided [59].

6.2 Mechanical characterization for modeling

Building a complete numerical model will help simulating complex loading schemes that regularly are more challenging to test. The first step of attaining a model is to perform adequate mechanical tests with focus on highlighting the behavior of interest. In this study, helical electrospun scaffolds were tested in at 0.1mm/s and 0.01mm/s to model the hyperelastic and viscoelastic behavior of helical electrospun scaffolds. The constant strain portion of the test was increased to 2000s to capture the complete viscoelastic response to attain a more accurate model. In figure 6.1(a) and 6.2(a) the applied load on fresh samples is visualized, at 0.1mm/s and 0.01mm/s, while the response of the load is pictured in figure 6.1(b) and 6.2(b).

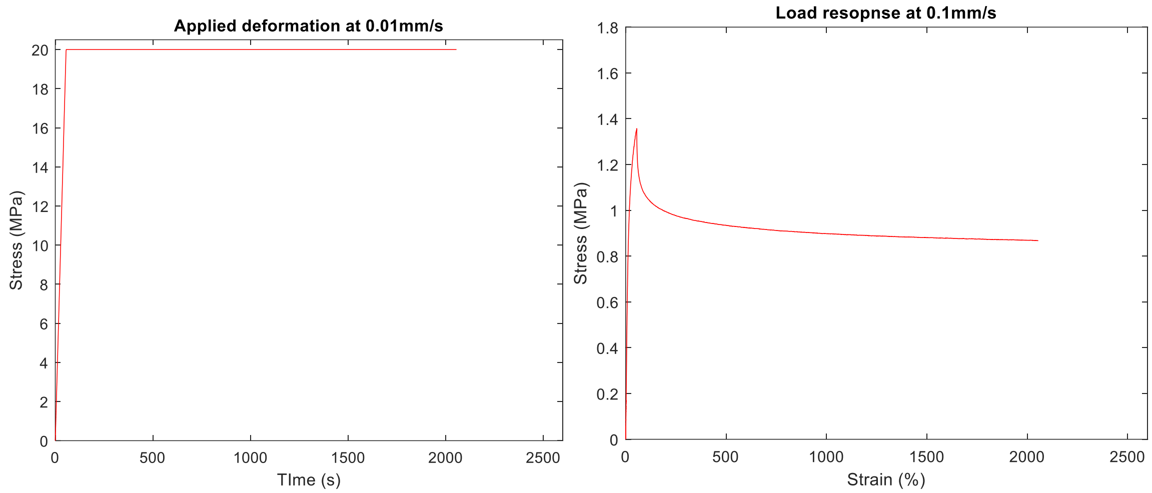

(a) (b)

Figure 6.1 Tensile testing of preconditioned sample, exploring the hyperelastic and viscoelastic behavior at 0.1mm/s; (a) deformation load on the and (b) is the applied deformation.

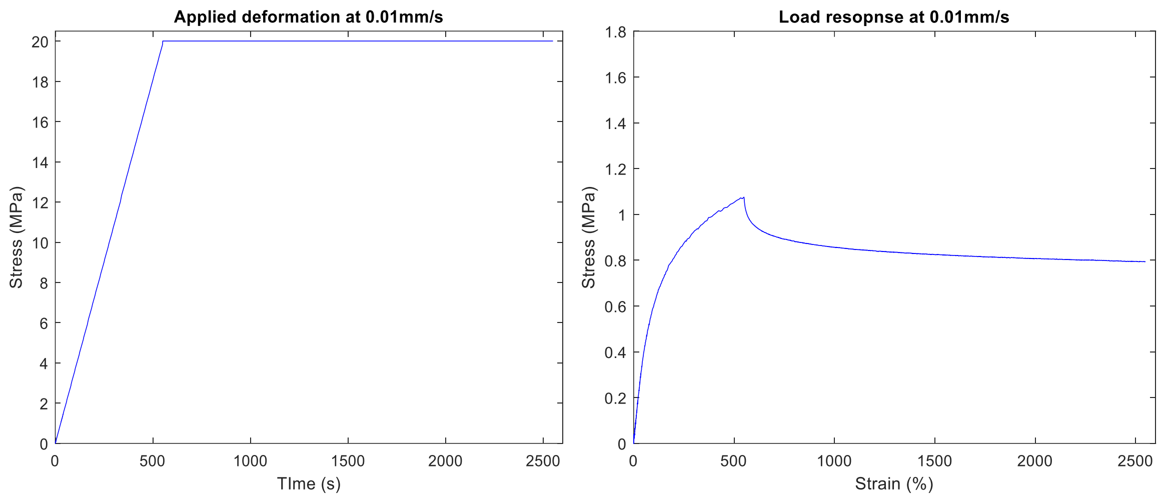

(a) (b)

Figure 6.2 Tesnile testing of preconditioned sample, exploring the hyperelastic and viscoelastic behavior at 0.01mm/s.; (a) applied deformation on the and (b) is the applied deformation.

Based on the conclusion from the previous study, it was determined that the sample post conditioning result in a different response when compared to preconditioned coupons. Samples were conditioned for 20 cycles where the strain cycled between 20% and zero, subsequently it was loaded to 20% strain and finally it was subjected to constant strain for

2000s. The load applied in the post conditioning and subsequent loading can be envisioned in figures 6.3(a) and 6.4(a) for 0.1mm/s and 0.01mm/s. While figure 6.3(b) and 6.4(b) captures the applied deformation of both speeds.

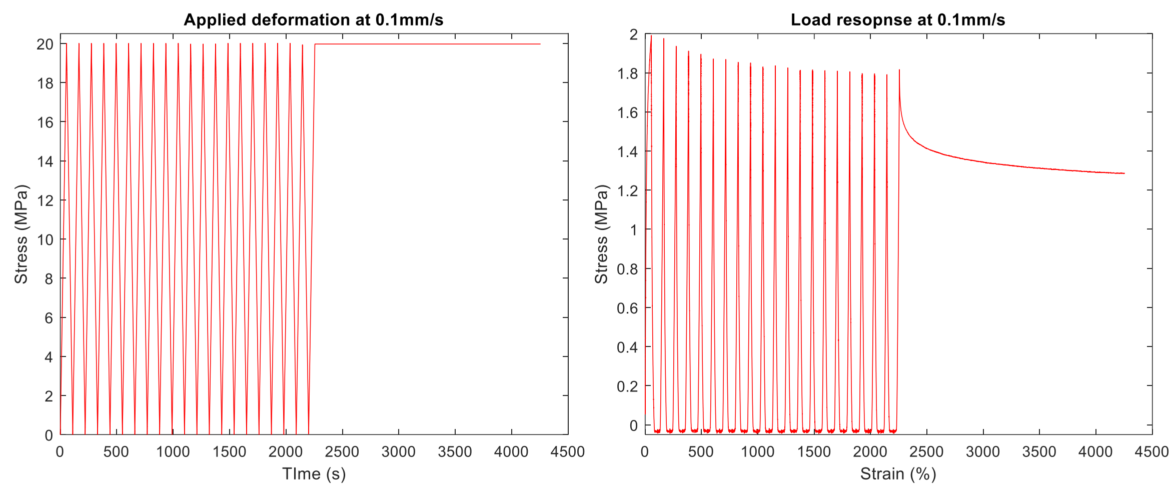

(a) (b)

Figure 6.3 Tesnile testing of postconditioned sample, exploring the hyperelastic and viscoelastic behavior at 0.1mm/s; (a) applied defomration on the and (b) is the applied deformation.

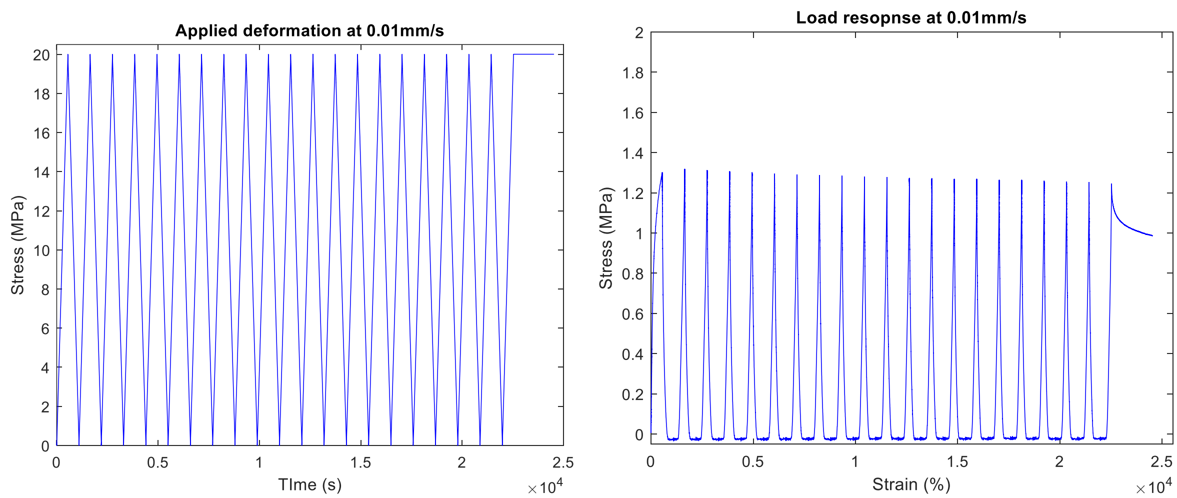

(a) (b)

Figure 6.4 Tensile testing of postconditioned sample, exploring the hyperelastic and viscoelastic behavior at 0.01mm/s; (a) applied defomration on the and (b) is the applied deformation.

6.3 Modeling of helical electrospun scaffolds

Finding the constitutive matrix for the material is a crucial step in achieving a scaffold success for the cardiac implantation. Evaluating the test data versus the existing theoretical models is the first step in meeting this major objective in the TE field. While predicting the data using uniaxial test data only is may result in accurate curve fittings, testing other test configurations, such as equiaxial or compression, it is favored to utilize more than one test data to increase the accuracy of the models. Furthermore, the assumptions concluded before the evaluation of data are crucial to the model precision when compared to material responses. Based on the literature review of characterizing electrospun scaffolds, there was no clear consensus if the material is isotropic or anisotropic [57], [61]. In this study, the material was assumed as incompressible, however, this point requires further research which is beyond the scope of this thesis.

6.3.1 Hyperelastic modeling

The objective of attaining stable existing models is to determine the constitutive matrix of the model. This is defined as the first step in building a complete model that may predict the behavior in various simulations. Stable models need to provide a good curve fit with the experimental data to be utilized in further studies. In this section, experimental data has been modeled using a commercial software (ABAQUS 2020, Dassault Systèmes), where the data is implemented as uniaxial test data. The evaluation included all the models available in the software, however only the stable models are discussed. The following models are analyzed:

- Ogden N=1
- Arruda-Boyce
- Van Der Waal
- Reduced Polynomial N=1
- Reduced Polynomial N=2
- Yeoh (Reduced Polynomial N=3)

Due to the abnormal behavior when compared to elastomers, the preconditioned samples resulted in less than desired curve fitting results. Preconditioned experimental data at both speeds increase with a positive slope until a certain strain level then the stress values tend to increase at a slower pace. At the speed of 0.1mm/s all stables models resulted in a linearly increasing curves, which does not match the experimental data. The results of stable models' evaluations can be seen in figure 6.5 for 0.1mm/s and figure 6.6 for 0.01mm/s. Values for the stable model coefficients for this case can be seen in table 6.1 for 0.1mm/s and table 6.2 for 0.01mm/s. The root mean squared error (RMSE) has been calculated, comparing the experimental test data to each model respectively.

Several unstable models for 0.1mm/s and 0.01mm/s loading speed case have resulted in good curve fittings which can be seen in figure 6.7 for the 0.1 mm/s. A rational deduced behind the instability if the models are due to the high deformation examined. Ogden N=1 is stable in uniaxial tension but deemed unstable for smaller uniaxial compression loading and high biaxial tension loading. Conducting further tests in other loading configuration, such as compression, confined compression, biaxial tension and equiaxial testing will lead to more accurate models and stabilize other models. The unstable models visualized on figure 6.7 are all unstable in high strains.

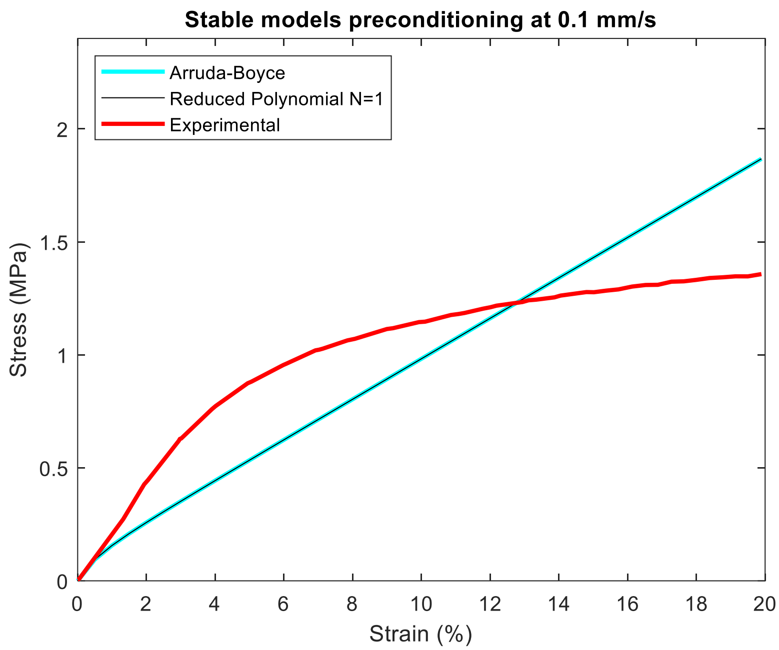

Figure 6.5 Stable models with preconditioned sample uniaxial test data provided to 20% strain. at 0.1mm/s loading speed.

Table 6.1 Stable hyperelastic models coefficient for preconditioned samples at 0.1mm/s.

Arruda-Boyce	***Reduced polynimial N=1***
μ= 3.72092	C_{10}=1.8694
$\mu_{0=}$ 3.720935	C_0=0
λ_M=621.903	
$D_{I=}0$	$D_{I=}0$
RMSE=0.2845	RMSE=0.2845

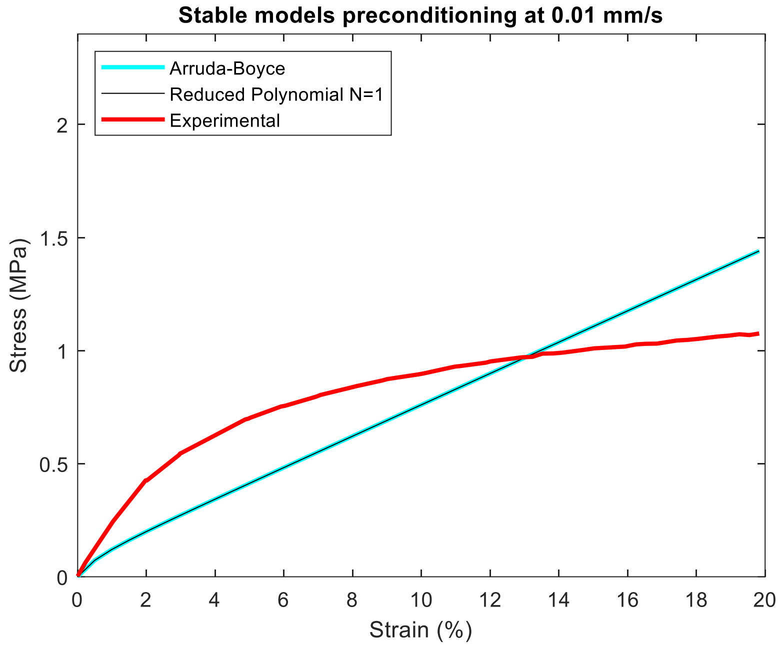

Figure 6.6 Stable models with preconditioned sample uniaxial test data provided to 20% strain. at 0.01mm/s loading speed.

Table 6.2 Stable hyperelastic models coefficient for preconditioned samples at 0.01mm/s

Arruda-Boyce	***Reduced polynimial N=1***
μ= 2.8223	C_{10}=1.41111
μ_0= 2.82232	C_0=0
λ_M=598.736	
$D_{I=}0$	$D_{I=}0$
RMSE=0.2234	RMSE=0.2234

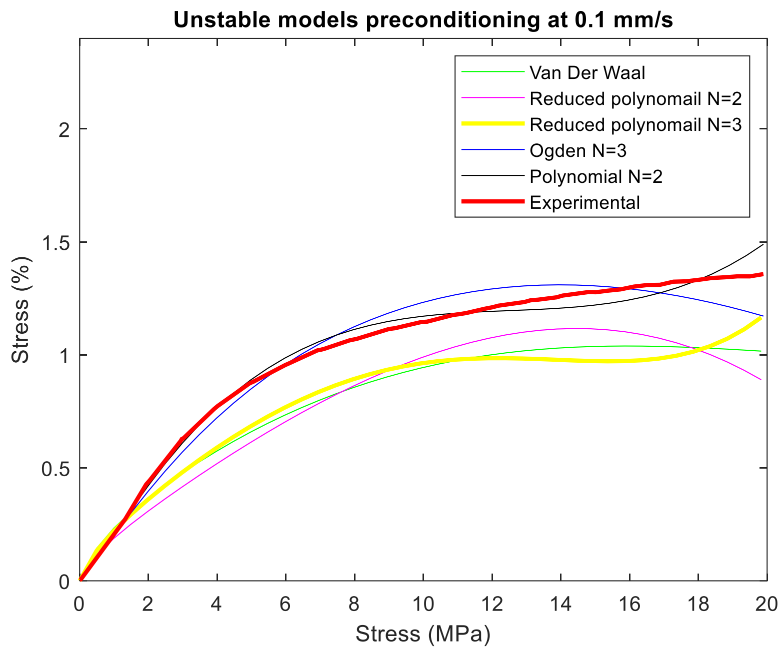

Figure 6.7 Stable models with postconditioned sample uniaxial test data provided to 20% strain. at 0.1mm/s loading speed.

The change in behavior due to conditioning resulted in better curve fitting when compared to preconditioned cases. Postconditioned samples is more relevant to the application of cardiac patches. As the scaffold will be cultivated with cardiac cell before implantation, thus will experience contractions.

The applied load resulted in steep increase in the stress strain when accounted for buckling. In both loading speeds tested, Ogden N= 1 resulted in the best fit when compared to other stable models. However, Yeoh and Van Der Waal models are deemed unstable in postconditioned samples at strains higher than 8.9% in tension. The results are visualized in both speeds in figures 6.8 and figures 6.9 for 0.1mm/s and 0.01mm/s respectively. The coefficient of the stable hyperelastic models for postconditioned behavior are listed in tables 6.3 and 6.4 for 0.1mm/s and 0.01mm/s, respectively.

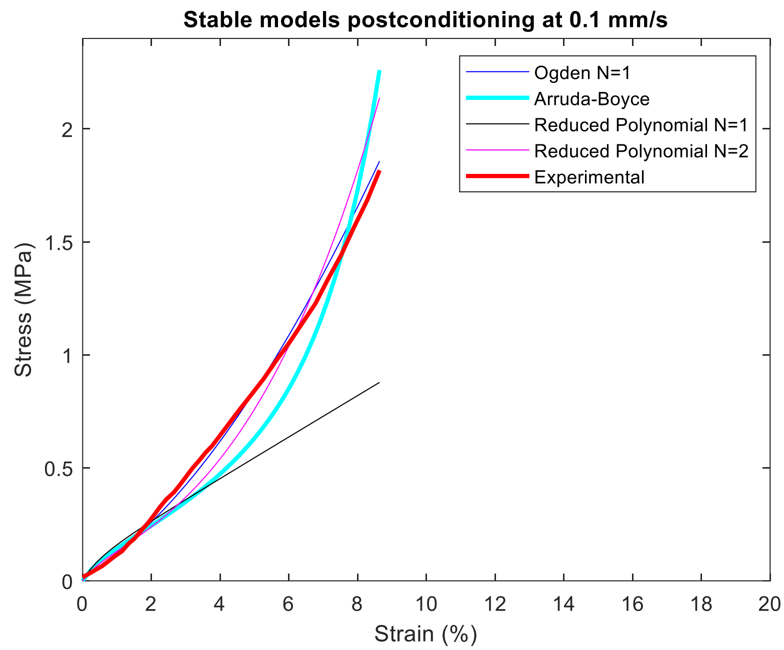

Figure 6.8 Stable models with postconditioned sample uniaxial test data provided to 20% strain. at 0.1mm/s loading speed.

Table 6.3 Stable hyperelastic models coefficient for postconditioned samples at 0.1mm/s.

Ogden N=1	***Arruda-Boyce***	***Reduced polynimial N=1***	***Reduced polynimial N=2***
I =1	$\mu= 4.9667237$	$C_{10}=2.514399$	$C_{10}=2.18888$
$\mu_I= 4.15922$	$\mu_0= 5.2873$	$C_0=0$	$C_{10}=-42.4887$
$\alpha_I=20.38422$	$\lambda_M=6.9998$		$C_{01}=C_{11}=0$
$D_I=0$	$D_I=0$	$D_I=0$	$D_I=0$
RMSE=0.03958	*RMSE=0.21209*	*RMSE=0.51601*	*RMSE=0.15299*

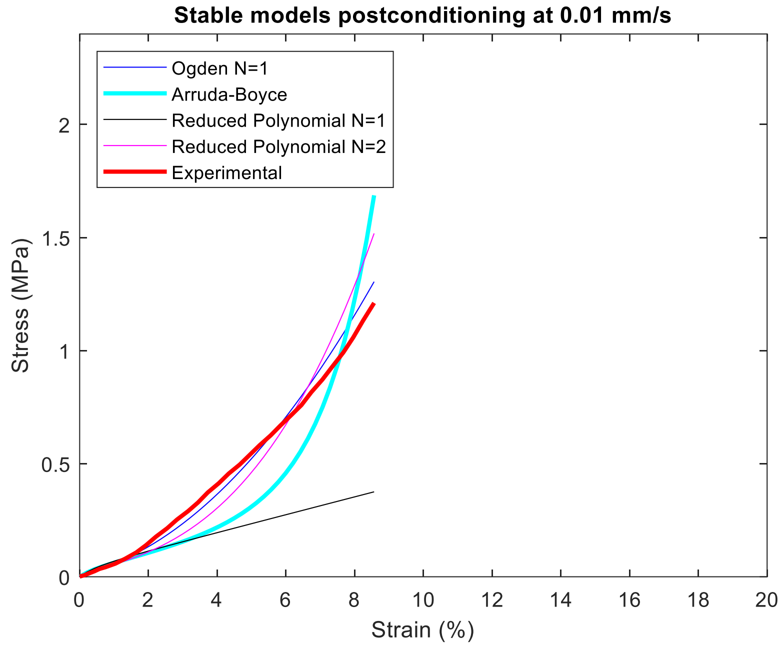

Figure 6.9 Stable models with postconditioned sample uniaxial test data provided to 20% strain. at 0.01mm/s loading speed.

Table 6.4 Stable hyperelastic models coefficient for postconditioned samples at 0.01mm/s.

Ogden N=1	***Arruda-Boyce***	***Reduced polynimial N=1***	***Reduced polynimial N=2***
$I=1$	$\mu= 2.60978$	$C_{10}=1.3213$	$C_{10}=1.03698$
$\mu_I= 2.1621$	$\mu_0=2.6423$	$C_0=0$	$C_{10}=44.76711$
$\alpha_I=25$	$\lambda_M=6.99982$		$C_{01}=C_{11}=0$
$D_{I=}0$	$D_{I=}0$	$D_{I=}0$	$D_{I=}0$
$RMSE=0.46873$	$RMSE=0.6404$	$RMSE=0.502459$	$RMSE=0.54829$

6.3.2 Viscoelastic modeling

Viscoelastic response has been accurately predicted using Prony series function. Samples at both speed 0.1mm/s and 0.01mm/s have been predicted in both preconditioned and conditioned samples. In the evaluation of the data the Prony series requires the experimental data serves as input in shear test data under time dependent data. The function utilizes stress in normalized fashion. Furthermore, the four cases analyzed resulted in accurate curve fitting. An observation can be made when comparing results between two different speed of similar conditioning scheme, the viscoelastic response recovery early in lower speeds. This conclusion can be made for preconditioned and conditioned samples. The corresponding viscoelastic coefficient models are listed below in the following tables 6.5,6.6,6.7 and 6.8 for each case evaluated, respectively.

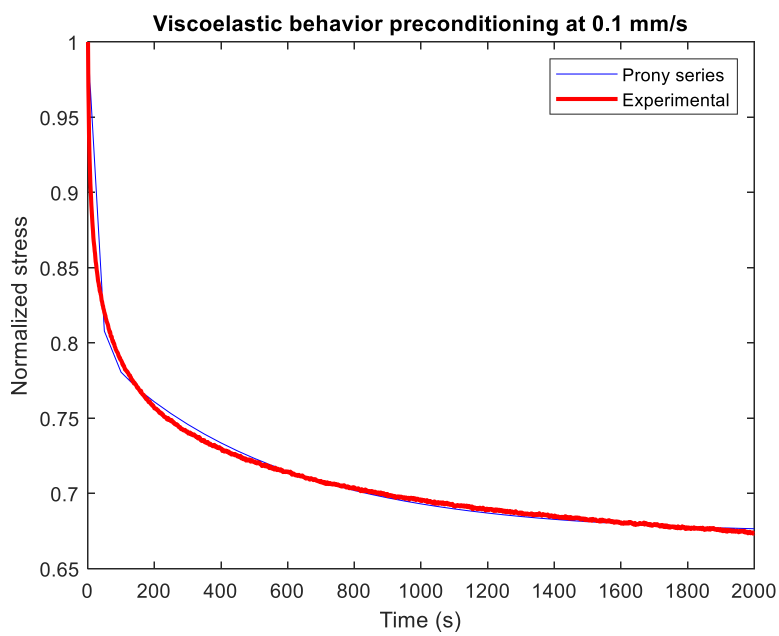

Figure 6.10 Viscoelastic behavior in preconditioned experimental data and Prony series prediciton at 0.1mm/s.

Table 6.5 Viscoelastic models coffeicients for preconditioned at 0.1mm/s.

	I=1	*I=2*
G(I)	*0.19936*	*0.12708*
K(I)	*0*	*0*
τ (I)	*21.078*	*532.47*
RMSE=0.002254755		

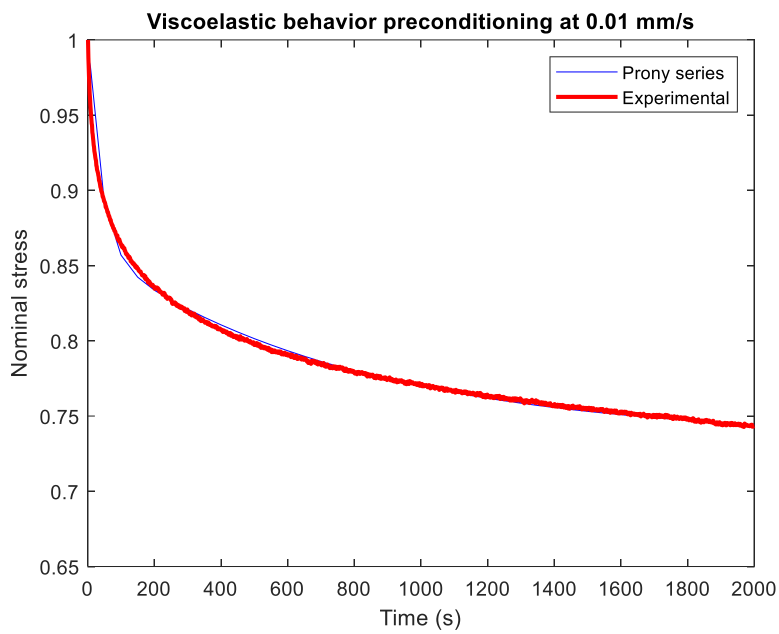

Figure 6.11 Viscoelastic behavior in preconditioned experimental data and Prony series prediciton at 0.01mm/s.

Table 6.6 Viscoelastic models coffeicients for preconditioned at 0.01mm/s.

	I=1	*I=2*
G(I)	*0.17575*	*0.1289*
K(I)	*0*	*0*
τ (I)	*32.409*	*606.95*
RMSE=0.0048561		

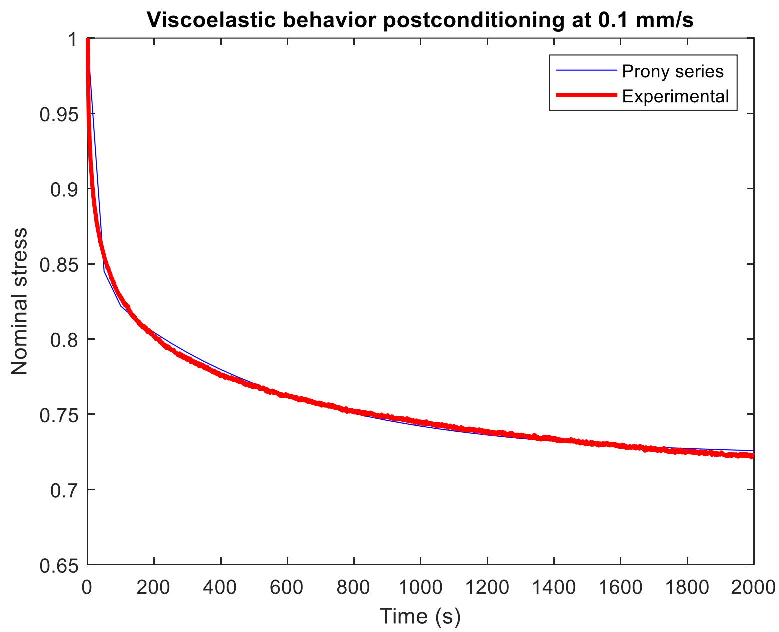

Figure 6.12 Viscoelastic behavior in postconditioning experimental data and Prony series prediciton at 0.1mm/s.

Table 6.7 Viscoelastic models coffeicients for postconditioned at 0.1mm/s.

	I=1	*I=2*
G(I)	*0.16031*	*0.11708*
K(I)	*0*	*0*
τ (I)	*21.233*	*557.43*
RMSE=0.0024181		

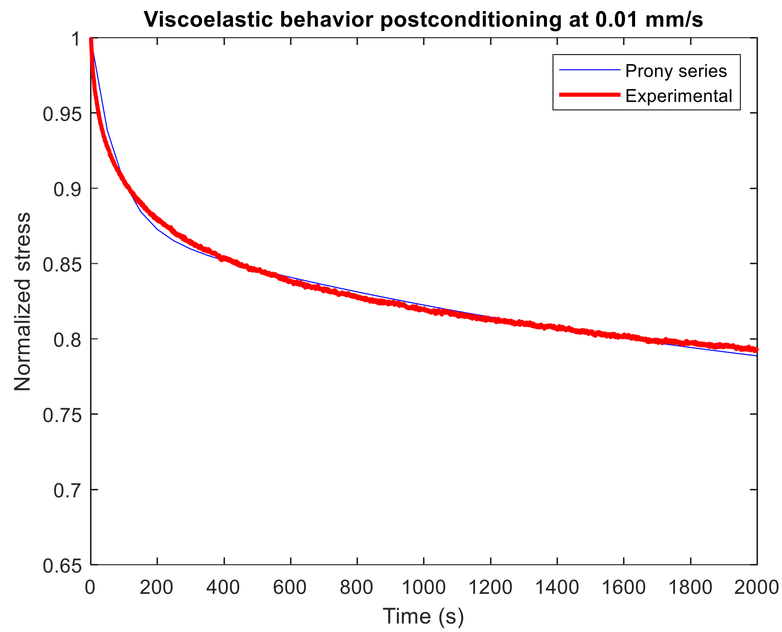

Figure 6.13 Viscoelastic behavior in postconditioning experimental data and Prony series prediciton at 0.01mm/s.

Table 6.8 Viscoelastic models coffeicients for postconditioned at 0.01mm/s.

	I=1	*I=2*
G(I)	*9.0781e^{-2}*	*0.11595*
K(I)	*0*	*0*
τ (I)	*41.26*	*765.29*
RMSE=0.0047859		

Examining the viscoelastic response pre and post conditioning, it was noted that the material experiences a larger drop in stress values before altering to a more linear response. This observation can be made for both speeds with respect to difference in stress value decrease in each speed. The comparison can be visualized in the following figures.

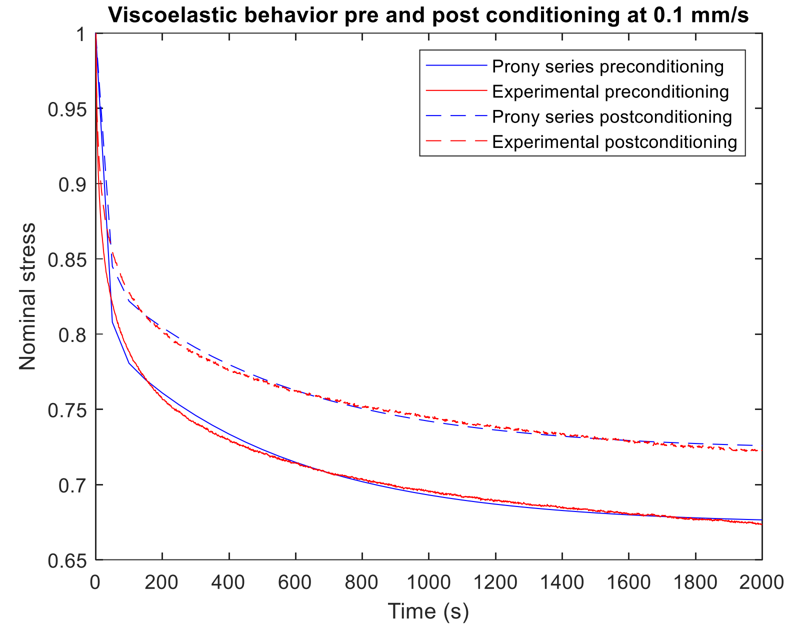

Figure 6.14 Comparison of the viscoelastic response in preconditioned and postconditioned coupons at 0.1mm/s.

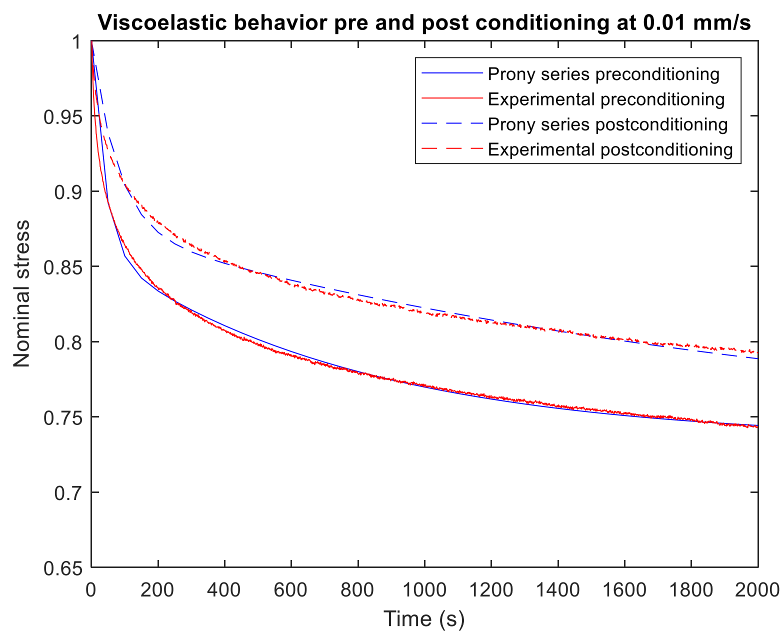

Figure 6.15 Comparison of the viscoelastic response in preconditioned and postconditioned coupons at 0.01mm/s.

Conclusion: *This chapter discussed the theoretical models utilized in curve fitting the experimental data in all cases. As for the assumptions deducted for modeling it, the material was assumed as isotropic and incompressible. Modeling the preconditioned samples for both speeds resulted in subpar curve fitting for the stable models, especially for the 0.1 mm/s loading speed. However, some unstable models provided a reasonable result, but deemed unstable due to the high deformation examined. Meanwhile, for the experimental data attained from postconditioned coupons they resulted in good fits with the Ogden N=1, functions. Lastly, the viscoelastic response was modeled using Prony series equation. The function provided immaculate results in both loading speeds at the two different conditions. Viscoelastic behavior is similar pre and post conditioning with respect to the difference in normalized stress values.*

7. Conclusion

In this chapter, we state the problem, identify the objectives of the research, and outline the contributions resulting from the work. Furthermore, a brief description of potential future work is presented.

7.1 Statement of the problem

To increase the cardiac regeneration rate post CVD or a heart attack, a passive method be required to be utilized. Based on the literature electrospun scaffold provide tremendous results in other TE application. To achieve a successful vascularization of a scaffold to be implanted it must behave similar to the native cardiac tissue, which may be achieved through this technique. However, one often overlooked property in engineered cardiac patches is the mechanical properties. Scaffold with similar fiber matrix and strain rates may achieve adequate force for pumping blood through out the body. It was stated in the literature that helical electrospun fibered scaffolds increased the operational strain limits when compared to conventional scaffolds.

The native cardiac tissue experiences various behaviours and phenomena. Based on the literature review conducted, the tissue experience stress softening, stress relaxation, and stress recovery. Another observation was that the material behavior is strain rate dependant. Examining the loading of the heart, during diastole and systole, it is observed that it is a complex loading scheme. During Diastole the material experience compression, while during systole the loading is tension. Which raises a challenge to subject any material through this loading conditions and strain rates. Attaining an accurate numerical model predicting the material behavior would aid in simulating said conditions.

In this thesis, a parameters sensitivity study was conducted to determine the optimal parameters to manufacture helical fibered electrospun scaffolds. Subsequently, the scaffold was mechanically characterized to examine various material behaviors. Lastly, experimental data was evaluated versus existing hyperelastic and viscoelastic numerical models.

7.2 Objective

i. Optimize electrospun helical fiber production.

A parameter sensitivity study is conducted to examine the effect of the varying process parameters. The objective of the study is to optimize the helical fiber production. Fibers are characterized using an optical microscope and an image analysis software to determine the fiber morphologies and diameters.

ii. Characterize the behavior of helical fibred scaffolds.

Scaffolds are prepared based on the optimal parameters obtained from the sensitivity study. Samples were processed for testing using a Rheometer with tensile fixtures. A comparison between electrospun samples and solid polymeric samples are conducted to determine the properties more akin to the native cardiac tissue. Three different loading schemes are used to determine the stress relaxation, recovery and softening. Sample recovery after conditioning was also explored after 24-hour recovery period. Lastly, coupons are tested to failure to examine the material response,

iii. Develop a numerical model to predict the scaffold response under different loading conditions.

The hyperelastic behavior of the material attained from mechanical characterization was evaluated against existing theoretical hyperelastic models. Stable models for each case tested is analyzed with respect to the experimental data to determine the accurate models. Furthermore, experimental viscoelastic response is utilized to establish a theoretical model using Pony series functions.

7.3 General conclusions

7.3.1 Manufacturing of scaffolds

In this study, the parameter of the electrospinning process was varied to examine the optimal helix fiber production. Helix fibers are formed due to buckling of the fibers under their own weight, subsequently the fibers were classified into Helix structured, partially buckled and straight fibers. Partially structured fibers contribute to the desired scaffold mechanical properties with a certain structural limitation. Based on this characterization each scaffold was scanned using an optical microscope to determine the optimum parameters for helical fiber production, and consequently analyzed using a software.

It was observed that 15% PCL concentration solution produced the highest percentage of helical structured fibers. While a solution with 17% PCL concentration provided median result when compared to the solutions utilized in the experiment. Moreover, increasing the solution concentration to 19% PCL concentration, resulted more helical fibers present in the scaffold. However, the scaffold also presented an increase in the number of beaded structures. Utilizing an angled collector with higher solution concentration, did not provide any desired results. Scaffold obtained higher number of beaded structures when compared to scaffold produced with flat collectors.

Environmental control of the electrospinning process may change the outcome drastically and result in a different scaffold structure. As mentioned in the literature review portion above, the effect of temperature on the fiber and scaffold morphology results in changed properties of the scaffold. However, to control the temperature without affecting the formation of fibers a passive cooling method is required. An active cooling method will affect the buckling of the fibers due to the increased air rotation in the electrospinning chamber. In this experiment due to the active cooling method utilized the buckling of fibers decreased and thus less helical fibers were present in the electrospun scaffold. Based on this conclusion, this study should be conducted with a passive cooling chamber that is well insulated and manufactured from nonconductive material to avoid any interference with the electromagnetic field.

7.3.2 Mechanical characterization

A scaffold consisting primarily of helical fibers that was manufactured based on a previous sensitivity study was tested to determine optimal helical fiber production. A downward regression line was observed during cyclical loading, signifying the presence of a stress softening effect. Stress relaxation was evident in all the three tests conducted, visualized by a sharp decrease in the stress values during constant strain loading. The combined loading test has highlighted the stress recovery capacity of the material. During the multi-step loading test, stress levels exceeded the values achieved during the final cycles of the cyclical loading phase. Stress softening and stress relaxation experienced by the samples were following trends seen in various soft materials. Where the peak stress resulting in the sample decreases with later cycles up to a threshold where the stress value stabilizes. Meanwhile, subjecting the sample to constant strain led the stress to gradually decrease in the sample. Obtaining the mechanical characteristics of a spring-like fibered cardiac scaffold will facilitate the development of a scaffold with properties tailored to those matching the properties of native cardiac tissue.

Electrospun samples exhibited stress values that were lower than those of solid samples, and thus electrospun samples were more capable of matching the mechanical properties of the native cardiac tissue. Additional benefits of using a fibred scaffold as opposed to solid samples is the structure of the scaffolds, with a more fibrous scaffold translating to better cell and molecular infiltration. Nevertheless, both samples demonstrated stress softening and stress relaxation recovery behavior.

Tested scaffolds experienced a degree of plastic deformation during loading and relaxations. The recovery of the samples was examined over 24 hours. A tested coupon was examined after the test and after 24-hour recovery in room environment conditions. It was observed that a recovery was evident. After testing the sample deformed about 11.6% of its original length and after recovery period the sample was only deformed for 5.6% of the original length.

Lastly, based on the previous observations the where the scaffold properties change during conditioning. Pre and postconditioned samples were tested to fracture in both loading speeds or 0.1 mm/s and 0.01 mm/s. While the preconditioned samples provided a typical stress strain curve for a material with a strain dependent modulus. The postconditioned samples resulted in an abnormal stress strain curve, where the material properties were altered at a specific strain point. As the samples reaches the strain threshold, the stress increase was almost a linear increase to failure from grips. This theorized due to the extreme stretching of the helical fibers and a change in the crystal structure of the samples.

7.3.3 Constitutive modeling of scaffolds

Attaining a constitutive matrix for the helical fibered scaffolds was the first step to simulating and predicting the material at more complex loading schemes. This was be performed using experimental data examining the hyperelastic and viscoelastic material response. Data was used as an input in a commercial and evaluated in terms of multiple existing theoretical models. The stable models in all cases where Arruda-Boyce and reduced polynomial N=1. Several assumptions were partaken based on the literature, where the material is assumed isotropic and incompressible.

In preconditioned sample at 0.1 mm/s loading speed, all models provided subpar curve fitting. However, the unstable models of Ogden N=1, Odgen N=3 and polynomial N=3 provided adequate results but cannot be utilized in predicting novel loading conditions. Meanwhile the postconditioned coupons had improved curve fitting results for several models. While some other model did provide good curve fitting results using the root mean squared error method Ogden N=1 will provide most accurate simulation results. Based on the results, the coefficients from Odgen N=1 may be used to build the first model to predict the complex loading conditions in postconditioned application.

The viscoelastic behavior was evaluated using the Prony series functions. The functions resulted in immaculate curve firring for all cases analyzed. Comparing the pre and postconditioned samples response, it was noted that the response was similar before and after conditioning with respect to the difference in the normalized stress values. Concluding that the material exhibits linear viscoelastic behavior

7.4 Thesis contributions

In this thesis, helical electrospun scaffolds were manufactured with a modification to the solution and process parameters. A sensitivity study was conducted to highlight the optimal parameters for electrospun helical fibers. Based on the parameters attain, cardiac patches were attained and mechanically characterized and modeled. A summary of the observations and contributions is as follows:

- *Scaffold manufacturing:*
  1. Optimal parameters for helical fiber production using electrospun was attained.
  2. The parameters resulted in fiber diameters akin to the native cardiac tissue fiber diameters.
- *Mechanical characterization:*
  1. Stress softening phenomena, stress relaxation and stress recovery was evident in both loading speeds tested, similar to other soft material and native cardiac tissue behavior.
  2. Some degree of plastic deformation occurs to the sample, which result in buckling of the sample during conditioning.

iii. Tested samples experience recovery post 24-hours of testing, which room environmental conditions.

iv. The material post conditioning experience a change in the Young's modulus and thus limits the operating range.

- *Numerical modeling of the scaffold:*

i. None of the stable models provided an accurate fit for the 0.1 mm/s preconditioned samples.

ii. For both speeds examined in postconditioned samples, the experimental data aligns with Odgen N=1 function.

iii. Prony series provided very good fit for all experimental data evaluated.

iv. The material experience linear viscoelastic behavior based on the strains examined.

7.5 Future remarks

The following areas require additional future research:

i. Conduct temperature-controlled study with specialized environment control chambers designed with passive cooling scheme.

ii. Improve the strain operation range of the material by post process treatments.

iii. Further examination of material behavior in other loading configurations.

iv. Explore the material behavior at temperature suitable extended cell incubation periods.

v. Examine the material compressibility.

vi. Investigate material if behaves in isotropic or anisotropic manner.

vii. Evaluate experimental data while considering other loading configuration to build more accurate numerical models.

Electrospun scaffolds have been used in the TE field for an extend duration of time. Though significant research has been conducted on the scaffolds, the literature is lacking mechanical characterization research. Future research may focus on further examining the material properties in biaxial loading conditions. Other loading conditions should also be examined with more precise and purpose-built equipment to capture the mechanical properties. Moreover, characterizing samples in compression is challenging due to the fibred structure of a scaffold, as testing the scaffold in compression would neglect the benefits of the physical structure obtained using electrospinning. Suitable compression testing will aid in determining the incompressibility of the scaffold which will aid in attaining an accurate constitutive model.

Bibliography

[1] R. E. S. Bowen, T. J. Graetz, D. A. Emmert, and M. S. Avidan, "Statistics of heart failure and mechanical circulatory support in 2020," *Ann. Transl. Med.*, vol. 8, no. 13, Jul. 2020, doi: 10.21037/atm-20-1127.

[2] P. H. A. of Canada, "Heart disease in Canada: Highlights from the Canadian Chronic Disease Surveillance System, 2017," *aem*, Aug. 22, 2017. https://www.canada.ca/en/public-health/services/publications/diseases-conditions/heart-disease-canada-fact-sheet.html (accessed Sep. 22, 2020).

[3] "Heart Failure | NHLBI, NIH." https://www.nhlbi.nih.gov/health-topics/heart-failure (accessed Sep. 22, 2020).

[4] J. H. Morris and L. Chen, "Exercise Training and Heart Failure: A Review of the Literature," *Card. Fail. Rev.*, vol. 5, no. 1, pp. 57–61, Feb. 2019, doi: 10.15420/cfr.2018.31.1.

[5] A. P. Ambrosy *et al.*, "The Global Health and Economic Burden of Hospitalizations for Heart Failure: Lessons Learned From Hospitalized Heart Failure Registries," *J. Am. Coll. Cardiol.*, vol. 63, no. 12, pp. 1123–1133, Apr. 2014, doi: 10.1016/j.jacc.2013.11.053.

[6] C. M. O'Connor *et al.*, "Efficacy and Safety of Exercise Training in Patients With Chronic Heart Failure: HF-ACTION Randomized Controlled Trial," *JAMA J. Am. Med. Assoc.*, vol. 301, no. 14, pp. 1439–1450, Apr. 2009, doi: 10.1001/jama.2009.454.

[7] M. R. Cowie *et al.*, “The epidemiology of heart failure,” *Eur. Heart J.*, vol. 18, no. 2, pp. 208–225, Feb. 1997, doi: 10.1093/oxfordjournals.eurheartj.a015223.

[8] H. Denolin, H. Kuhn, H. Krayenbuehl, F. Loogen, And A. Reale, “The defintion of heart failure,” *Eur. Heart J.*, vol. 4, no. 7, pp. 445–448, Jul. 1983, doi: 10.1093/oxfordjournals.eurheartj.a061500.

[9] Z. Lister, K. J. Rayner, and E. J. Suuronen, “How Biomaterials Can Influence Various Cell Types in the Repair and Regeneration of the Heart after Myocardial Infarction,” *Front. Bioeng. Biotechnol.*, vol. 4, 2016, doi: 10.3389/fbioe.2016.00062.

[10] D. Allbrook, “Skeletal muscle regeneration,” *Muscle Nerve*, vol. 4, no. 3, pp. 234–245, 1981, doi: https://doi.org/10.1002/mus.880040311.

[11] M. Mercola, P. Ruiz-Lozano, and M. D. Schneider, “Cardiac muscle regeneration: lessons from development,” *Genes Dev.*, vol. 25, no. 4, pp. 299–309, Feb. 2011, doi: 10.1101/gad.2018411.

[12] T. Billiet, M. Vandenhaute, J. Schelfhout, S. Van Vlierberghe, and P. Dubruel, “A review of trends and limitations in hydrogel-rapid prototyping for tissue engineering,” *Biomaterials*, vol. 33, no. 26, pp. 6020–6041, Sep. 2012, doi: 10.1016/j.biomaterials.2012.04.050.

[13] R. A. Wolfe, E. C. Roys, and R. M. Merion, “Trends in Organ Donation and Transplantation in the United States, 1999–2008,” *Am. J. Transplant.*, vol. 10, no. 4p2, pp. 961–972, 2010, doi: https://doi.org/10.1111/j.1600-6143.2010.03021.x.

[14] K. D. Boudoulas and A. K. Hatzopoulos, "Cardiac repair and regeneration: the Rubik's cube of cell therapy for heart disease," *Dis. Model. Mech.*, vol. 2, no. 7–8, pp. 344–358, Jul. 2009, doi: 10.1242/dmm.000240.

[15] J. Duan, "Wnt1/βcatenin injury response activates the epicardium and cardiac fibroblasts to promote cardiac repair," *EMBO J.*, vol. 31, no. 2, pp. 429–442, Jan. 2012, doi: 10.1038/emboj.2011.418.

[16] Y. Liu, J. Lim, and S.-H. Teoh, "Review: Development of clinically relevant scaffolds for vascularised bone tissue engineering," *Biotechnol. Adv.*, vol. 31, no. 5, pp. 688–705, Sep. 2013, doi: 10.1016/j.biotechadv.2012.10.003.

[17] B. P. Chan and K. W. Leong, "Scaffolding in tissue engineering: general approaches and tissue-specific considerations," *Eur. Spine J.*, vol. 17, no. 4, pp. 467–479, Dec. 2008, doi: 10.1007/s00586-008-0745-3.

[18] B. K. Gu, D. J. Choi, S. J. Park, Y.-J. Kim, and C.-H. Kim, "3D Bioprinting Technologies for Tissue Engineering Applications," in *Cutting-Edge Enabling Technologies for Regenerative Medicine*, H. J. Chun, C. H. Park, I. K. Kwon, and G. Khang, Eds. Singapore: Springer, 2018, pp. 15–28. doi: 10.1007/978-981-13-0950-2_2.

[19] E. Tzahor and K. D. Poss, "Cardiac regeneration strategies: Staying young at heart," *Science*, vol. 356, no. 6342, pp. 1035–1039, Jun. 2017, doi: 10.1126/science.aam5894.

[20] N. F. Huang, "Big bottlenecks in cardiovascular tissue engineering," *Commun. Biol.*, vol. 1, no. 1, Art. no. 1, Nov. 2018, doi: 10.1038/s42003-018-0202-8.

[21] S. Sankar, C. S. Sharma, and S. N. Rath, “Enhanced osteodifferentiation of MSC spheroids on patterned electrospun fiber mats - An advanced 3D double strategy for bone tissue regeneration,” *Mater. Sci. Eng. C*, vol. 94, pp. 703–712, Jan. 2019, doi: 10.1016/j.msec.2018.10.025.

[22] S. Fleischer, A. Shapira, R. Feiner, and T. Dvir, “Modular assembly of thick multifunctional cardiac patches,” *Proc. Natl. Acad. Sci.*, Feb. 2017, doi: 10.1073/pnas.1615728114.

[23] Y. Li *et al.*, “Engineering cell alignment in vitro,” *Biotechnol. Adv.*, vol. 32, no. 2, pp. 347–365, Mar. 2014, doi: 10.1016/j.biotechadv.2013.11.007.

[24] I. Jun, H.-S. Han, J. R. Edwards, and H. Jeon, “Electrospun Fibrous Scaffolds for Tissue Engineering: Viewpoints on Architecture and Fabrication,” *Int. J. Mol. Sci.*, vol. 19, no. 3, Mar. 2018, doi: 10.3390/ijms19030745.

[25] R. Feiner, A. Shapira, and T. Dvir, “32 - Scaffolds for tissue engineering of functional cardiac muscle,” in *Handbook of Tissue Engineering Scaffolds: Volume One*, M. Mozafari, F. Sefat, and A. Atala, Eds. Woodhead Publishing, 2019, pp. 685–703. doi: 10.1016/B978-0-08-102563-5.00032-0.

[26] N. Bhardwaj and S. C. Kundu, “Electrospinning: A fascinating fiber fabrication technique,” *Biotechnol. Adv.*, vol. 28, no. 3, pp. 325–347, May 2010, doi: 10.1016/j.biotechadv.2010.01.004.

[27] S. Fleischer, J. Miller, H. Hurowitz, A. Shapira, and T. Dvir, “Effect of fiber diameter on the assembly of functional 3D cardiac patches,” *Nanotechnology*, vol. 26, no. 29, p. 291002, Jul. 2015, doi: 10.1088/0957-4484/26/29/291002.

[28] S. Fleischer, “Spring-like fibers for cardiac tissue engineering,” *Biomaterials*, vol. 34, no. 34, pp. 8599–8606, Nov. 2013, doi: 10.1016/j.biomaterials.2013.07.054.

[29] M. Kharaziha *et al.*, “PGS:Gelatin nanofibrous scaffolds with tunable mechanical and structural properties for engineering cardiac tissues,” *Biomaterials*, vol. 34, no. 27, pp. 6355–6366, Sep. 2013, doi: 10.1016/j.biomaterials.2013.04.045.

[30] I. Alghoraibi and S. Alomari, “Different Methods for Nanofiber Design and Fabrication,” in *Handbook of Nanofibers*, A. Barhoum, M. Bechelany, and A. Makhlouf, Eds. Cham: Springer International Publishing, 2018, pp. 1–46. doi: 10.1007/978-3-319-42789-8_11-2.

[31] S. Fleischer, R. Feiner, and T. Dvir, “Cardiac tissue engineering: from matrix design to the engineering of bionic hearts,” *Regen. Med.*, vol. 12, no. 3, pp. 275–284, Apr. 2017, doi: 10.2217/rme-2016-0150.

[32] P. E. S. Silva, F. V. de Abreu, and M. H. Godinho, “Shaping helical electrospun filaments: a review,” *Soft Matter*, vol. 13, no. 38, pp. 6678–6688, Oct. 2017, doi: 10.1039/C7SM01280B.

[33] T. Han, D. H. Reneker, and A. L. Yarin, “Buckling of jets in electrospinning,” *Polymer*, vol. 48, no. 20, pp. 6064–6076, Sep. 2007, doi: 10.1016/j.polymer.2007.08.002.

[34] T. Peijs, "6.7 Electrospun Polymer Nanofibers and Their Composites," in *Comprehensive Composite Materials II*, P. W. R. Beaumont and C. H. Zweben, Eds. Oxford: Elsevier, 2018, pp. 162–200. doi: 10.1016/B978-0-12-803581-8.10025-6.

[35] C. H. Park, H. R. Pant, and C. S. Kim, "Novel robot-assisted angled multi-nozzle electrospinning set-up: computer simulation with experimental observation of electric field and fiber morphology:," *Text. Res. J.*, Jan. 2014, doi: 10.1177/0040517513517961.

[36] S. Suresh, A. Becker, and B. Glasmacher, "Impact of Apparatus Orientation and Gravity in Electrospinning-A Review of Empirical Evidence," *Polymers*, vol. 12, no. 11, Oct. 2020, doi: 10.3390/polym12112448.

[37] A. Faraone, "Dispensing pico droplets by pyroelectrohydrodynamic jetting: simulations and experimental results," 2019. doi: 10.5281/zenodo.3530462

[38] D. Li and Y. Xia, "Electrospinning of Nanofibers: Reinventing the Wheel?," *Adv. Mater.*, vol. 16, no. 14, pp. 1151–1170, 2004, doi: 10.1002/adma.200400719.

[39] D. H. Reneker and I. Chun, "Nanometre diameter fibres of polymer, produced by electrospinning," *Nanotechnology*, vol. 7, no. 3, pp. 216–223, Sep. 1996, doi: 10.1088/0957-4484/7/3/009.

[40] K. Garg and G. L. Bowlin, "Electrospinning jets and nanofibrous structures," *Biomicrofluidics*, vol. 5, no. 1, Mar. 2011, doi: 10.1063/1.3567097.

[41] S. Koombhongse, W. Liu, and D. H. Reneker, "Flat polymer ribbons and other shapes by electrospinning," *J. Polym. Sci. Part B Polym. Phys.*, vol. 39, no. 21, pp. 2598–2606, 2001, doi: 10.1002/polb.10015.

[42] J. M. Deitzel, J. Kleinmeyer, D. Harris, and N. C. Beck Tan, “The effect of processing variables on the morphology of electrospun nanofibers and textiles,” *Polymer*, vol. 42, no. 1, pp. 261–272, Jan. 2001, doi: 10.1016/S0032-3861(00)00250-0.

[43] H. Fong, I. Chun, and D. H. Reneker, “Beaded nanofibers formed during electrospinning,” *Polymer*, vol. 40, no. 16, pp. 4585–4592, Jul. 1999, doi: 10.1016/S0032-3861(99)00068-3.

[44] Z. Li and C. Wang, “Effects of Working Parameters on Electrospinning,” in *One-Dimensional nanostructures: Electrospinning Technique and Unique Nanofibers*, Z. Li and C. Wang, Eds. Berlin, Heidelberg: Springer, 2013, pp. 15–28. doi: 10.1007/978-3-642-36427-3_2.

[45] “Electrospinning Process,” in *An Introduction to Electrospinning and Nanofibers*, 0 vols., WORLD SCIENTIFIC, 2005, pp. 90–154. doi: 10.1142/9789812567611_0003.

[46] J. M. López-Herrera and A. M. Gañán-Calvo, “A note on charged capillary jet breakup of conducting liquids: experimental validation of a viscous one-dimensional model,” *J. Fluid Mech.*, vol. 501, pp. 303–326, Feb. 2004, doi: 10.1017/S0022112003007560.

[47] G. I. Taylor and M. D. Van Dyke, “Electrically driven jets,” *Proc. R. Soc. Lond. Math. Phys. Sci.*, vol. 313, no. 1515, pp. 453–475, Dec. 1969, doi: 10.1098/rspa.1969.0205.

[48] A. G. Şener, A. S. Altay, and F. Altay, “Effect of voltage on morphology of electrospun nanofibers,” in *2011 7th International Conference on Electrical and Electronics Engineering (ELECO)*, Dec. 2011, p. I–324.

[49] Z. Rezvani, J. R. Venugopal, A. M. Urbanska, D. K. Mills, S. Ramakrishna, and M. Mozafari, “A bird’s eye view on the use of electrospun nanofibrous scaffolds for bone tissue engineering: Current state-of-the-art, emerging directions and future trends,” *Nanomedicine Nanotechnol. Biol. Med.*, vol. 12, no. 7, pp. 2181–2200, Oct. 2016, doi: 10.1016/j.nano.2016.05.014.

[50] H. S. SalehHudin, E. N. Mohamad, W. N. L. Mahadi, and A. Muhammad Afifi, “Multiple-jet electrospinning methods for nanofiber processing: A review,” *Mater. Manuf. Process.*, vol. 33, no. 5, pp. 479–498, Apr. 2018, doi: 10.1080/10426914.2017.1388523.

[51] C. Mit-uppatham, M. Nithitanakul, and P. Supaphol, “Ultrafine Electrospun Polyamide-6 Fibers: Effect of Solution Conditions on Morphology and Average Fiber Diameter,” *Macromol. Chem. Phys.*, vol. 205, no. 17, pp. 2327–2338, 2004, doi: 10.1002/macp.200400225.

[52] C. Pislaru, T. P. Abraham, and M. Belohlavek, “Strain and strain rate echocardiography,” *Curr. Opin. Cardiol.*, vol. 17, no. 5, pp. 443–454, Sep. 2002, doi: 10.1097/00001573-200209000-00002.

[53] A. Heimdal, A. Støylen, H. Torp, and T. Skjaerpe, “Real-time strain rate imaging of the left ventricle by ultrasound,” *J. Am. Soc. Echocardiogr. Off. Publ. Am. Soc. Echocardiogr.*, vol. 11, no. 11, pp. 1013–1019, Nov. 1998, doi: 10.1016/s0894-7317(98)70151-8.

[54] J. D’hooge *et al.*, “Two-dimensional ultrasonic strain rate measurement of the human heart in vivo,” *IEEE Trans. Ultrason. Ferroelectr. Freq. Control*, vol. 49, no. 2, pp. 281–286, Feb. 2002, doi: 10.1109/58.985712.

[55] J. Bonzon *et al.*, “Rigor mortis at the myocardium investigated by post-mortem magnetic resonance imaging,” *Forensic Sci. Int.*, vol. 257, pp. 93–97, Dec. 2015, doi: 10.1016/j.forsciint.2015.07.039.

[56] G. Sommer *et al.*, “Biomechanical properties and microstructure of human ventricular myocardium,” *Acta Biomater.*, vol. 24, pp. 172–192, Sep. 2015, doi: 10.1016/j.actbio.2015.06.031.

[57] R. R. Duling, R. B. Dupaix, N. Katsube, and J. Lannutti, “Mechanical Characterization of Electrospun Polycaprolactone (PCL): A Potential Scaffold for Tissue Engineering,” *J. Biomech. Eng.*, vol. 130, no. 1, Feb. 2008, doi: 10.1115/1.2838033.

[58] J. E. Bischoff, E. M. Arruda, and K. Grosh, “Finite element modeling of human skin using an isotropic, nonlinear elastic constitutive model,” *J. Biomech.*, vol. 33, no. 6, pp. 645–652, Jun. 2000, doi: 10.1016/s0021-9290(00)00018-x.

[59] E. Gkouti, B. Yenigun, and A. Czekanski, “Transient Effects of Applying and Removing Strain on the Mechanical Behavior of Rubber,” *Materials*, vol. 13, no. 19, Art. no. 19, Jan. 2020, doi: 10.3390/ma13194333.

[60] T. Lu, J. Wang, R. Yang, and T. J. Wang, “A Constitutive Model for Soft Materials Incorporating Viscoelasticity and Mullins Effect,” *J. Appl. Mech.*, vol. 84, no. 2, Nov. 2016, doi: 10.1115/1.4035180.

[61] H. Mondésert, “Anisotropic PCL electrospun scaffolds for soft tissue engineering : Elaboration, morphological and mechanical properties,” 2020.

[62] J. C.-W. Lee, K. M. Weigandt, E. G. Kelley, and S. A. Rogers, “Structure-Property Relationships via Recovery Rheology in Viscoelastic Materials,” *Phys. Rev. Lett.*, vol. 122, no. 24, p. 248003, Jun. 2019, doi: 10.1103/PhysRevLett.122.248003.

[63] R. W. Ogden and R. Hill, “Large deformation isotropic elasticity – on the correlation of theory and experiment for incompressible rubberlike solids,” *Proc. R. Soc. Lond. Math. Phys. Sci.*, vol. 326, no. 1567, pp. 565–584, Feb. 1972, doi: 10.1098/rspa.1972.0026.

[64] M. C. Boyce and E. M. Arruda, “Constitutive Models of Rubber Elasticity: A Review,” *Rubber Chem. Technol.*, vol. 73, no. 3, pp. 504–523, Jul. 2000, doi: 10.5254/1.3547602.

[65] A. Ali, M. Hosseini, and B. Sahari, “A review of constitutive models for rubber-like materials,” 2010, doi: 10.3844/AJEASSP.2010.232.239.

[66] M. Smith, “ABAQUS/Standard User’s Manual, Version 6.14.” Dassault Systèmes Simulia Corp, 2014.